NGU Report 2009.041
Shallow geology and seabed processes,
Western Barents Sea

NGU
Norges geologiske undersøkelse
Geological Survey of Norway

Geological Survey of Norway
NO-7491 Trondheim, Norway
Tel.: 47 73 90 40 00
Telefax 47 73 92 16 20

REPORT

Report no.: NGU Report 2009.041	ISSN 0800-3416	Grading: Open

Title:
Shallow geology and seabed processes, Western Barents Sea

Authors:
Shyam Chand, Terje Thorsnes, Leif Rise, Reidulv Bøe

Client:
Lundin Norge AS

County:
Norway

Commune:

Map-sheet name (M=1:250.000)

Map-sheet no. and -name (M=1:50.000)

Deposit name and grid-reference:

Number of pages: 71 Price (NOK): 260
Map enclosures: 0

Fieldwork carried out:	Date of report:	Project no.:	Person responsible:
	24th August 2009	328200	Øystein Nordgulen

Summary:

The project is aimed to achieve a better understanding of shallow geological/seabed conditions and processes to support technical and environmental aspects of exploration and production along the western margin of the Hammerfest Basin and Loppa High, and in the Tromsø Basin/Ingøydjupet area.

The project has had the following subgoals:

- Detection of pockmarks and seep-related features, including water column gas flares and neo-tectonic structures
- Investigate the occurrence of gas hydrates (GH), bottom-simulating reflectors (BSR) and other related seismic anomalies
- Establish seismostratigraphy

The project has the following results:

- Bathymetry and backscatter has given an overview of Holocene surface features such as pockmarks, iceberg ploughmarks etc and their relation to subsurface geological processes. Even though numerous pockmarks were identified in two basins along the study area, no water column gas flares were detected to indicate active gas leakage.
- Gas and BSR-like anomalies were identified and related to gas hydrate stability conditions of the study area. GHSZ modelling indicates gas hydrate stability for structure II hydrates with a few percent of ethane, propane or CO_2.
- High-resolution seismic data gave a detailed picture of depositional processes during post glacial times. Two subunits, 4W1 and 4W2, are identified within the youngest Quaternary unit 4W. They probably represent the two last glacial advances LGM I and II towards the present shelf edge.

Keywords: Marine Geology	Gas hydrate	Flare
Pockmark	Seismic	Seismostratigraphy
BSR	Shallow gas	Multibeam bathymetry

CONTENTS

FIGURES

Figure 1. Structural map of the study area showing major geological formation boundaries at the base Plio-Pleistocene level and regional bathymetry (grey contours). Also shown are areas surveyed using EM710 multibeam echosounder (dashed blue polygon), 3D seismic (blue polygon), BSR occurrences (blue filled polygon), gas anomalies (purple) (Andreassen and Hansen, 1995), locations of faults (dashed black lines) and oil fields (red filled polygon).
Figure 2. Regional bathymetry of the study area showing the locations of the multi beam bathymetry (MBB) (blue polygons), 3D seismic (red polygon), 2D industry seismic lines (red lines), FFI 2D seismic lines (thick black lines) and TOPAS lines (thin black lines). Also shown are the locations of gas anomalies (purple), BSRs (blue) (Andreassen and Hansen, 1995), hydrocarbon discoveries (yellow) and faults (dashed lines).
Figure 3. Overview of water depths for the MBB area. The red stippled lines indicate the boundary between areas with pockmarks (the basins areas A and B) and areas with no or few pockmarks.
Figure 4 Nearly 15 m deep iceberg ploughmark. Note slump deposits along the eastern margin (arrow).
Figure 5 Backscatter data from the southern MBB area. Note low reflectance in the basin areas – A and B.
Figure 6. Part of basin B, showing how soft sediments (lower right corner) cover iceberg ploughmarks.
Figure 7A. Detailed bathymetry from basin A showing coexistence of pockmarks with iceberg ploughmarks. Black lines indicate ship tracks.
Figure 7B. Detailed backscatter of the area shown in Fig. 7A from basin A showing backscatter signatures of pockmarks and iceberg ploughmarks. Notice high backscatter (red) associated with pockmarks and at the rims of ploughmarks.
Figure 8A. Detailed bathymetry from basin B showing co-existence of pockmarks in recent sediments and partly buried iceberg ploughmarks.
Figure 8B. Detailed backscatter of the area shown in Fig. 8A from basin B showing backscatter signatures of pockmarks and iceberg ploughmarks. Notice high backscatter associated with pockmarks and at the edges of ploughmarks.
Figure 9A. Detailed bathymetry from pockmark area showing a large pockmark-like feature in coexistence with smaller pockmarks and iceberg ploughmarks.
Figure 9B. Detailed backscatter of the area shown in Fig. 9A from basin A showing backscatter signatures of pockmarks and iceberg ploughmarks. Notice high backscatter associated with pockmarks and at the rims of ploughmarks. The large pockmark-like features have high backscatter rims indicating a probable iceberg plunging/ploughing origin.
Figure 10. Large irregular pockmark (same as shown in Fig. 9A), 20 m deep. Bathymetry grid size around the large pockmark is 1 m, while it is 5 m in the background. Both pockmarks are asymmetric, indicating an origin as a mega-scale prod mark. Iceberg drift direction is indicated by arrows.
Figure 11. A) Overview map showing the distribution of investigated lines (black lines), and BSR occurrences and gas anomalies (blue transparent polygons, from Andreassen & Hansen, 1995). B) Example_Fish_school: Screen dump from the Kongsberg SIMRAD SIS software. F – fish schools; N – noise; SBR – seabed reflector. Width of view – c. 750 m.
Figure 12. A and B: Examples of possible biogenic structures (M – mounds; X – cross-cutting structures) and glacigenic structures (IPR – iceberg ploughmark ridges). C: Coral reef mounds (K) as they occur on the Røst Reef (water depth -400 m on the shelf, and down to -600 m in the upper left (blue) part).
Figure 13. Example of a continuous bottom simulating reflector (BSR) from Blake Ridge. Amplitude blanking shown in the figure is still not considered as genuine, since many places

blanking is more representative of the sediment uniformity in a gas devoid environment (Hornbach et al, 2003).
Figure 14. Disrupted BSR or gas hydrate anomalies within methane hydrate stability region from Blake Ridge (Holbrook et al., 2002).
Figure 15. Gas hydrate region from the Mallik well showing gas-like reflections within and below methane hydrate stability depths. Also shown is the sonic log showing the high gas hydrate concentration zones (Bellefleur et al., 2006).
Figure 16. High frequency single airgun data showing very feeble BSR signature in a gas hydrate zone from lake Baikal. Notice that there is no BSR beneath the gas hydrate recovery site (Vanneste et al., 2001).
Figure 17. OBC data from the BSR zone within the Storegga Slide area, offshore Norway showing the seismic signatures across a BSR in a low gas hydrate concentration zone (Buenz and Mienert, 2004). The BSR is shown up as a change in amplitude across a permeable layer in the PP section (vertical component) while such anomalies are absent above and below layers. Due to low concentration of gas hydrates no significant anomaly is produced in the PS section (inline component).
Figure 18. VSP derived P wave a) velocity and b) attenuation from Mallik 2L 38 well Mackenzie delta Canada showing the distinctive acoustic properties of hydrate bearing sediments (Pratt et al., 2003)
Figure 19. Log derived P and S wave a) attenuations and b) velocities in hydrate bearing sediments at Mallik 2L-38 well Mackenzie delta, Canada (Guerin and Goldberg, 2002). The hydrate bearing sediment velocities and attenuations increase with hydrate saturation.
Figure 20. Example from the Barents Sea showing patchy reflections which are interpreted as due to gas hydrates (Laberg et al., 1998).
Figure 21. Patchy high amplitude reflections close to the seafloor in and around region of pockmarks indicating active fluid flow blocked by the possible presence of gas hydrates (Chand et al., 2009).
Figure 22. Hydrate stability curves for various gas compositions and salinities (thick: seawater; thin: fresh water). The region to the right of the geothermal gradient curve is GHSZ and the thickness of it is the difference between seafloor and where the geothermal gradient cuts the stability curve for the particulate gas composition. The bottom water temperature is taken from the World Ocean Database (WOD05) and varies between 1.5 and 5.5 ^{o}C within the area shown. A linear geothermal gradient is assumed from this sea bottom temperature. NaCl and N_2 are inhibitors for hydrate formation and makes hydrate unstable, while presence of CO_2 and H_2S facilitate hydrate formation at deeper depths than normal, predicted above.
Figure 23. Two way time (ms, TWT) contour map of the GHSZ below seafloor shown on the structural map of the study area. The locations o MBB& 3D seismic datasets (blue polygons), and FFI 2D seismic profiles (black lines).
Figure 24. Two way time (ms, TWT) contour map of the GHSZ below sea surface shown on the structural map of the study area. Also shown is the TWT to base Tertiary (colour range 500 to 2500 ms), the locations of MBB & 3D seismic (LH08M01) datasets (blue polygons), and FFI 2D seismic profiles (black lines), two FFI TOPAS Seismic lines (pink), 2D industry seismic line NPDTR82_2045_8230 (green) and two cross lines from LHS08M01 (light blue).
Figure 25. FFIAG_1 2D seismic line (see Fig. 24 for location) in W-E direction indicating gas anomalies below the URU (orange).
Figure 26. FFIAG_6 2D seismic line (see Fig. 24 for location) in W-E direction indicating gas anomalies below the URU (orange).
Figure 27. FFI AG_7 2D seismic line (see Fig. 24 for location) in N-S direction indicating gas anomalies below the URU (orange).

discoveries(red), gas indications (purple), BSR (blue) and regional bathymetry of the study area (contours).
Figure 43. Base Tertiary TWT (sec) map overlaid on structural and bedrock map of the Barents Sea. Also shown are locations of the MBB and 3D seismic datasets (blue), oil discoveries(red), gas indications (purple), BSR (blue) and regional bathymetry of the study area (contours).
Figure 44. Base Quaternary/URU TWT (sec) map overlaid on structural and bedrock map of the Barents Sea. Also shown are locations of the MBB and 3D seismic datasets (blue), oil discoveries(red), gas indications (purple), BSR (blue) and regional bathymetry of the study area (contours).
Figure 45. FFIAG_1 2D seismic line (see Fig. 24 for location) in W-E direction indicating gas anomalies below the URU (orange).
Figure 46. FFIAG_6 2D seismic line (see Fig. 24 for location) in W-E direction indicating gas anomalies below the URU (orange).
Figure 47. FFIAG_7 2D seismic line (see Fig. 24 for location) in N-S direction indicating gas anomalies below the URU (orange).
Figure 48. FFIAG_7 2D seismic line (see Fig. 24 for location) in N-S direction indicating gas anomalies below the URU (orange).
Figure 49. FFI TOPAS line 101085 in W-E direction indicating intra 4w reflections 4W1 and 4W2 within the unit 4W. The southern pockmark area is underlain by a thin layer of soft sediments overlying glacial till from the last glaciation (4W1) is also indicated. Another intra 4W unit can be identified (4W2) which indicate deposition from a previous intra glacial cycle.
Figure 50. FFI TOPAS line 101065 in W-E direction indicating intra 4W reflection 4W1 within the unit 4W. The northern pockmark area is underlain by a thin layer of soft sediments overlying glacial till from the last glaciation (4W1) is also indicated.

TABLES

Table 1. Correlation of various units observed in the Barents Sea. Compiled by Laberg and Vorren (1996).

Table 2. Correlation of various units from western the Barents Sea based on compilation of information from various studies (Lebesbye 2000; Butt et al. 2000; Solheim et al. 1998; Sættem et al. 1992) and to those from this study.

1. INTRODUCTION

The Barents Sea is an epicontinental sea bounded by sheared and rifted Tertiary margin to the west (Eldholm et al., 1984). Mesozoic and early Cenozoic sedimentation took place in intracratonic basins. After the early Tertiary opening of the Norwegian Sea, the Tertiary sediment transport bypassed these basins, and depocentres were established on the continental margin (Spencer et al., 1984). The Bear Island trough was formed through extensive glacial erosion (Nøttvedt et al., 1988; Eidvin and Riis, 1989; Vorren et al., 1991; Riis and Fjeldskaar, 1992) and the bulk of the eroded sediments form the principal depocenter at the continental slope, the Bear Island Trough Mouth Fan (ATMF; Vorren et al., 1991; Faleide et al., 1996). The morphology of the Barents Sea has been interpreted as a submerged inherited fluvial landscape, formed in preglacial times and later modified by glacial erosion (Nansen, 1904; Lastochkin, 1977; Vorren et al., 1986, 1991). Recent drilling and coring show that the main part of the erosion took place in the late Plio-Pleistocene (<2.7 Ma) and that the corresponding sediments have mainly a glacial affinity (Eidvin and Riis, 1989; Eidvin et al., 1993, 1998; Mørk and Duncan, 1993; Sættem et al., 1994; Hald et al., 1990: Knies et al., 2009).

Estimates show that about 1000 m of sediments may have been removed by the erosion (Nøttvedt et al., 1988; Vorren et al., 1991; Riis and Fjeldskaar, 1992; Løseth et al., 1992; Nyland et al., 1992). The erosion produced a prominent erosion surface, the upper regional unconformity, URU (Solheim and Kristoffersen, 1984; Vorren et al., 1986). An upper glacigenic sediment sequence of varying thickness covers the URU (Solheim and Kristoffersen, 1984; Vorren et al., 1986). It reaches a maximum thickness of about 1000 m at the shelf edge, and has a secondary maximum on the inner shelf, adjacent to the Norwegian coast, where it fills a large glacial trough (Vorren et al., 1989, 1990). Associated with erosion, considerable late Cenozoic uplift took place, modeled by Riis and Fjeldskaar (1992) to 900-1400 m in the western Barents Sea. A major part of the fan is of late Pliocene and Pleistocene age (Eidvin and Riis, 1989; Eidvin et al., 1993), which implies very high erosion and sedimentation rates. High erosion rates for the mid-late Pleistocene are also inferred by Vorren et al. (1991), with 150 m regionally, and as much as 400 m locally, during the last 0.8 Ma, and by Sættem et al. (1992) who suggest erosion of 200-250 m or more for the last 0.44 Ma. Seismostratigraphic interpretations indicate that grounded glaciers may have reached the shelf break of the southern Barents Sea 5-10 times during the Pleistocene (Solheim and Kritoffersen, 1984; Vorren et al., 1988; Sættem et al., 1992).

This present study is focused on a small region along the western Barents Sea and the western margin of the Hammerfest Basin, the Loppa High and the Tromsø Basin/Ingøydjupet area (Fig. 1). The project is aimed to achieve a better understanding of the shallow geological and

seabed conditions and processes to support technical and environmental aspects of exploration within the study area. The project has the following subgoals:

- To detect pockmarks and seep-related features, including water column gas flares, and neo-tectonic structures
- To investigate the occurrence of gas hydrates (GH), bottom-simulating reflectors (BSR) and other related seismic anomalies
- To establish seismostratigraphy.

2. STUDY AREA

The study focuses on the western margin of the Hammerfest Basin/Loppa High and the Tromsø Basin/Ingøydjupet areas of the western Barents Sea (Fig. 1).

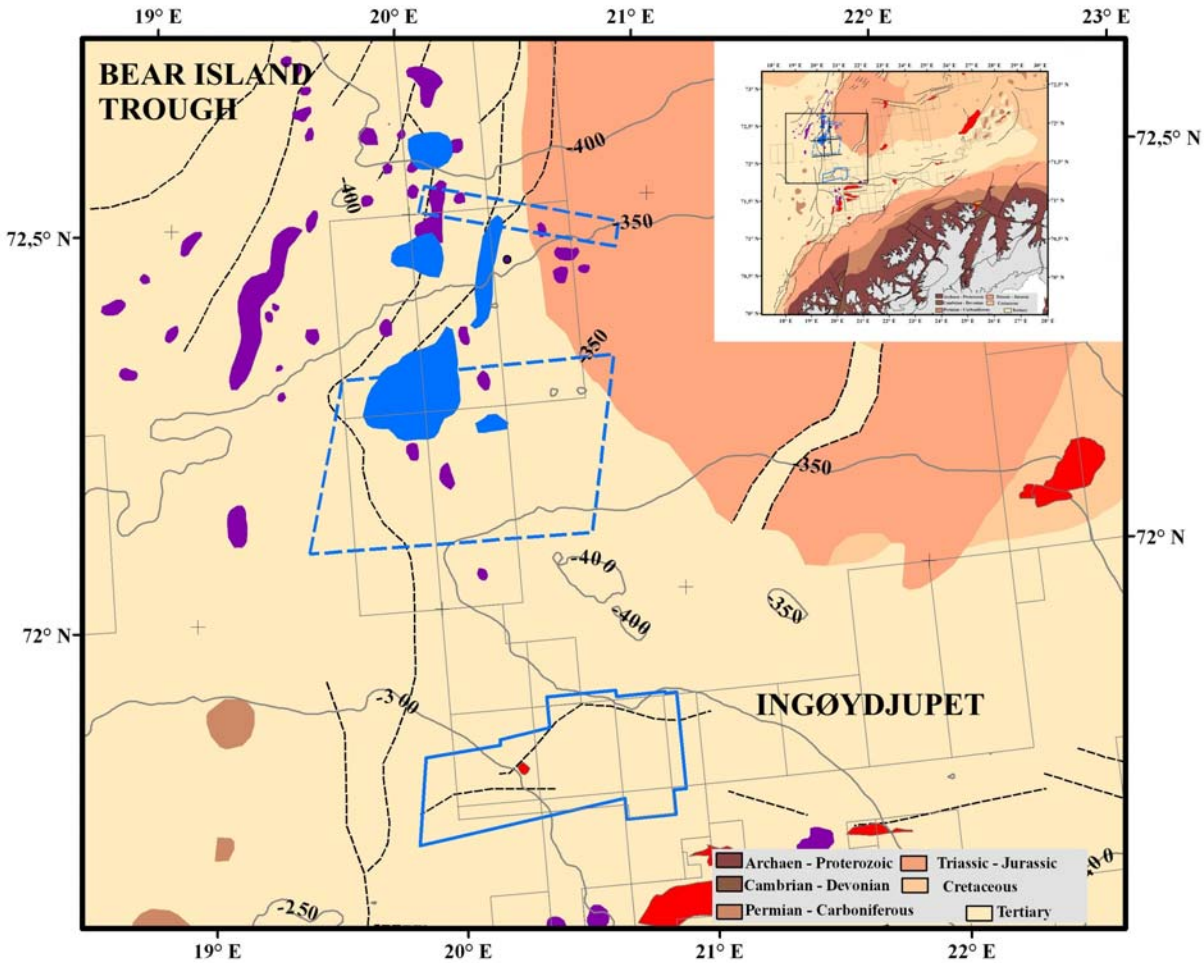

Figure 1. Structural map of the study area showing major geological formation boundaries at the base Plio-Pleistocene level and regional bathymetry (grey contours). Also shown are areas surveyed using EM710 multibeam echosounder (dashed blue polygon), 3D seismic (blue polygon), BSR occurrences (blue filled polygon), gas anomalies (purple) (Andreassen and Hansen, 1995), locations of faults (dashed black lines) and oil fields (red filled polygon).

3. MATERIALS AND METHODS

3.1 Bathymetry/Backscatter

The multi beam bathymetry (MBB) data was collected by Forsvarets Forskenings Institutt (FFI) using EM710 echo sounder (Fig. 2). The main advantage of the multibeam echosounder system is that it can record the water column data also. The operating frequency (70-100 kHz) is also advantageous for the intermediate water depths, between 200 m and 1000 m, where other systems usually need a change in frequency. The operating frequency of 70-100 kHz and the water depths of ca. 350 m at the study area give a Fresnel zone diameter (foot print) of around 4 m thus mapping 13 m^2 by each beam. As a general rule, features smaller than the size of one fourth the wavelength cannot be resolved (Sheriff, 1980) if there is adequate spatial sampling by the system used. Hence features larger than 1 meter in diameter can be theoretically detected using the system. The water column data recorded by the system can be used for detection of active gas seeps and also presence of fauna. Presences of fish schools can be easily identified and is hence useful to estimate the energy lose in the water column during detailed back scatter processing. The MBB data can also be used to derive the seafloor reflection (ie., backscatter) properties which will indirectly give an indication about the sediment type/grain size and/or hardness of the sea bottom.

3.2 TOPAS and 2D high resolution seismic

The TOPAS parametric subbottom profiler is used to acoustically map the sediments in the uppermost part of the seabed. Layering can be clearly interpreted if the source signal can penetrate the seafloor sediments thus giving a detailed stratigraphy going up to few tens of thousands of years. The 2D high resolution seismic using airgun gives a deeper penetration than the TOPAS, thus linking the near surface to shallow subsurface (Fig. 2). The single channel 2D seismic is limited in usability up to the first multiple and in our study area it is around 900 ms TWT.

3.3 2D/3D Seismic

The conventional 2D seismic covering the study area and the nearby region gives a regional perspective of the study area in relation to the surrounding geology. The occurrences of various formations in relation to structural features and stratigraphic discontinuities can be clearly delineated using these regional 2D seismic lines (Fig. 2). The 3D seismic data, LHS08M01 (Fig. 2), from south of the study area gives a detailed picture of the subsurface anomalies that can be expected in the shallow subsurface and can be used as guidance for interpreting anomalies from the study area.

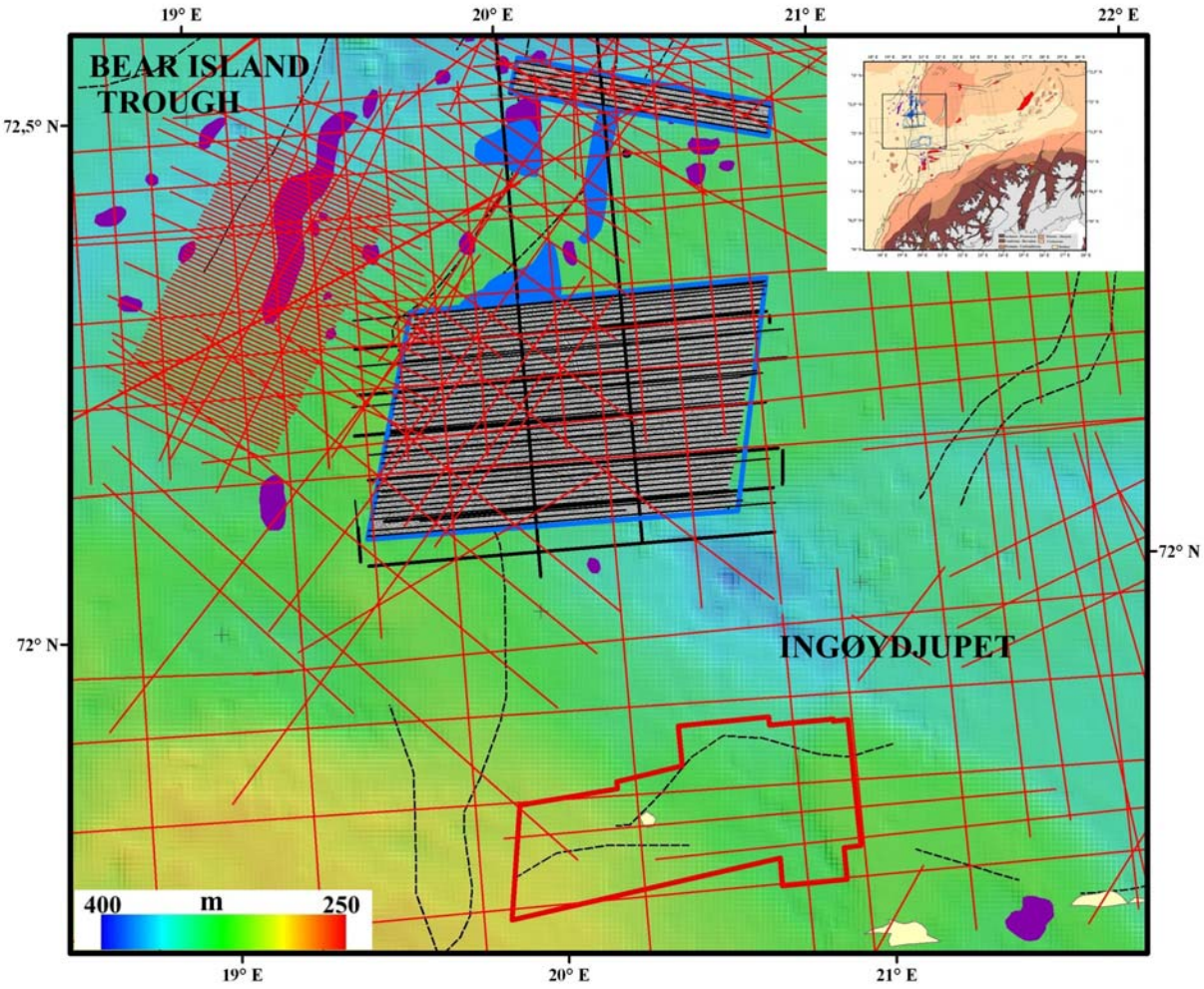

Figure 2. Regional bathymetry of the study area showing the locations of the multibeam bathymetry (MBB) (blue polygons), 3D seismic (red polygon), 2D industry seismic lines (red lines), FFI 2D seismic lines (thick black lines) and TOPAS lines (thin black lines). Also shown are the locations of gas anomalies (purple), BSRs (blue) (Andreassen and Hansen, 1995), hydrocarbon discoveries (yellow) and faults (dashed lines).

4. RESULTS

4.1 Pockmarks, gas flares and neotectonics

4.1.1 General morphology

The southernmost area mapped with MBB is located on a broad ridge, while the northernmost is located on the flank of the Bear Island Trough. The water depths (WD) range from 300 m to 400 m, with the deepest parts in the western end of the northern MBB area, and the SE corner of the southern MBB area (Fig 3). The southern area has two basins in the eastern part (A and B), separated by a ridge. The western part is flatter, with WD between 300 and 340 m. The northern area slopes from 330 m in the east, to 400 m in the west. Both areas are heavily

incised by iceberg ploughmarks (Fig. 4). The seabed has varying hardness, as shown by the backscatter (Fig. 5). The backscatter values range within the silty clay sediment type classification similar to those observed along the Tromsøflaket west of the study area. The basins have comparatively low reflectance, caused by a soft sediment cover. The range of backscatter values observed for the whole study area is very limited indicating that the sediments are almost uniform or at least the top few centimeters of the seafloor are draped by similar kind of sediments with minor changes associated with plough marks and pockmarks. The thickness in basin A is c. 30 ms TWT, while the sediment cover in basin B is c. 5 ms TWT. The soft sediments partly or totally cover older structures, like iceberg plough marks (Fig. 6).

4.1.2 Pockmarks

Pockmarks occur almost exclusively in basin areas A and B. Two general types of pockmarks can be recognized:

- Small circular pockmarks, generally less than 50 m in diameter and up to 2 m deep, with an average density of c. 100 pockmarks per square kilometer. The pockmarks are either randomly distributed, or occur in arrays along iceberg ploughmarks. The size and density of the pockmarks is pretty homogenous, apart from the c. 1 km broad boundary zone of the basins, where the pockmarks appear to be smaller, shallower and with a lower density. The size (both in depth and diameter) of the pockmarks is observed to decrease towards the margin peripheries where the soft sediment thickness also decreases. The occurrence of pockmarks altogether disappear after the soft sediment thickness reaches a threshold value either due to the absence of them or due to the resolution limits of the bathymetric mapping system. Particularly in basin A, the pockmarks have higher reflectivity than the surrounding sediments (Fig. 6-8).
- Large, irregular pockmarks, with diameters up to 300 m, depths up to 25 m, and with walls up to 30° (Fig. 9-10). They may have an irregular rim. In some places, iceberg ploughmarks start or end in these pockmarks, while other pockmarks have no obvious relation to ploughmarks. These pockmarks occur randomly over the entire area.

The small circular pockmarks are interpreted to be linked to fluid seepage (liquids and/or gas). It is not possible to indicate whether the source is of biogenic or thermogenic nature. The occurrence of pockmarks is primarily controlled by the existence of soft sediments in the basins. This means that fluid seepage could be occurring also outside the basins, but no pockmarks will form as the seabed sediment does not have the right properties (e.g. morainal material/till). This is similar to the observations from Goliat area of Ingøydjupet (Chand et al., 2009) where pockmarks were observed to be associated to subsurface faults but occurring throughout the basin but limited by the thickness of soft sediment cover. Chand et al (2009)

attribute this to diffused flow within the shallow basinal sediments after coming out of the focused fluid flow region of faults which connects it to the subsurface.

The large irregular pockmarks could have several origins. Explosive events related to gas escape could be one formation mechanism, and would be consistent with the crater-like appearance and the irregular rims. Another explanation could be that these structures are relict keel marks from grounding icebergs. Similar structures off Ireland (Porcupine and Rockall Banks) described as sub-circular craters up to 1000 m across and up to 20 m deep have been interpreted to be relict keel marks (X. Monteys et al., IGC2008). Complex iceberg crater marks on the seafloor of the Labrador shelf, partly in linear crater chains, has been described by Bass & Woodworth-Lynas (1988). These authors attribute the craters to a mechanism where icebergs alternatively impact and rotate free of the seabed. Broadly similar structures, termed "Iceberg gravity crater with pressure ridge" have been described by Longva & Thoresen (1991). These structures formed in the Romerike area of southwestern Norway, and were formed as the water level fell after a gigantic flood (jøkulhlaup) from the ice-dammed lake Nedre Glåmsjø. In conclusion – the large irregular pockmarks are interpreted as being related to icebergs, and not explosive events. The distinctly asymmetric nature of some of the pockmarks means that they can be described as mega-scale prod marks, indicating the iceberg drift direction.

4.1.3 Gas flares

The EM710 multibeam echosounder optionally records water column data. A selection of these data was studied during a two-day visit to FFI in May 2009, using the Kongsberg SIMRAD SIS software (Fig. 11A). This software allows the original recordings to be replayed and displayed at the same speed as data acquisition, but has no possibilities for fast rewinding, or extracting water column features. Lines crossing the pockmark areas, some of the large irregular pockmarks, and BSR/gas anomalies were chosen. No obvious gas flares were detected during this pilot study. Fish schools were detected, demonstrating the potential for gas bubble detection, since the acoustic character of fish is mainly caused by the gas filled swim bladder (Fig. 11B)

4.1.4 Neotectonic structures

We have studied seabed morphology in order to map surface expressions of neotectonic structures. No structures were identified, and neotectonic structures are thus probably not present. However, the highly irregular seabed morphology makes identification of subtle features difficult. No neotectonic structures have been indicated from the FFI 2D or TOPAS lines.

4.1.5 Possible biogenic macrostructures

The morphology of the seabed was studied to find possible biogenic structures. The approach was to study small-scale structures, and exclude clearly geological structures, such as sand waves, slumped masses from iceberg ploughmarks crossing older ploughmarks, slumped masses from the flanks of the ploughmarks (e.g. Fig. 4), or iceberg ploughmark ridges formed during the ploughmark formation process (for the latter, see below).
A few candidates occur outside the basin areas. An example of circular to sub-circular mounds occurring in iceberg ploughmarks can be observed in (Fig. 12A). Structures crossing the iceberg ploughmarks can be observed at several places, and one example is shown in Fig. 12B. This structure (X) crosses a c.45 m wide iceberg ploughmark at c. 80^{o} angle, and is c. 5m high. Along the flanks of the iceberg ploughmarks, several mounds (M) which are a few meter high occur. An iceberg ploughmark ridge (IPR) is found on the northern side of the ploughmark. Coral mounds occurring on the flanks or growing across iceberg plough marks are know from previous studies on the mid Norwegian shelf (Thorsnes et al., 2004; Hovland et al., 2005). An example of this is shown in Fig. 12C. The backscatter data was inspected as part of the study. The reflectivity varies from medium to high, and does not provide any conclusive indications for the origin of the structures.

The shape, dimension and mode of occurrence of mounds observed in the survey area are compatible with coral reef mounds documented on the mid-Norwegian shelf and on the shelf off Troms (e.g. the Malangen Reef – http://www.mareano.no/nyhetere/2007/nytt_korallrev). Crosscutting structures have been observed, but occur in far fewer cases. The present area is located north of the known coral reef occurrences, sponge build-ups of this dimension which are possible to detect with acoustic methods is not known, as far as we know. We consider the probability of the mounds and crosscutting to be of biogenic origin to be low, but existing. We therefore suggest that some of the objects should be studied more closely using appropriate high-resolution acoustic or visual methods.

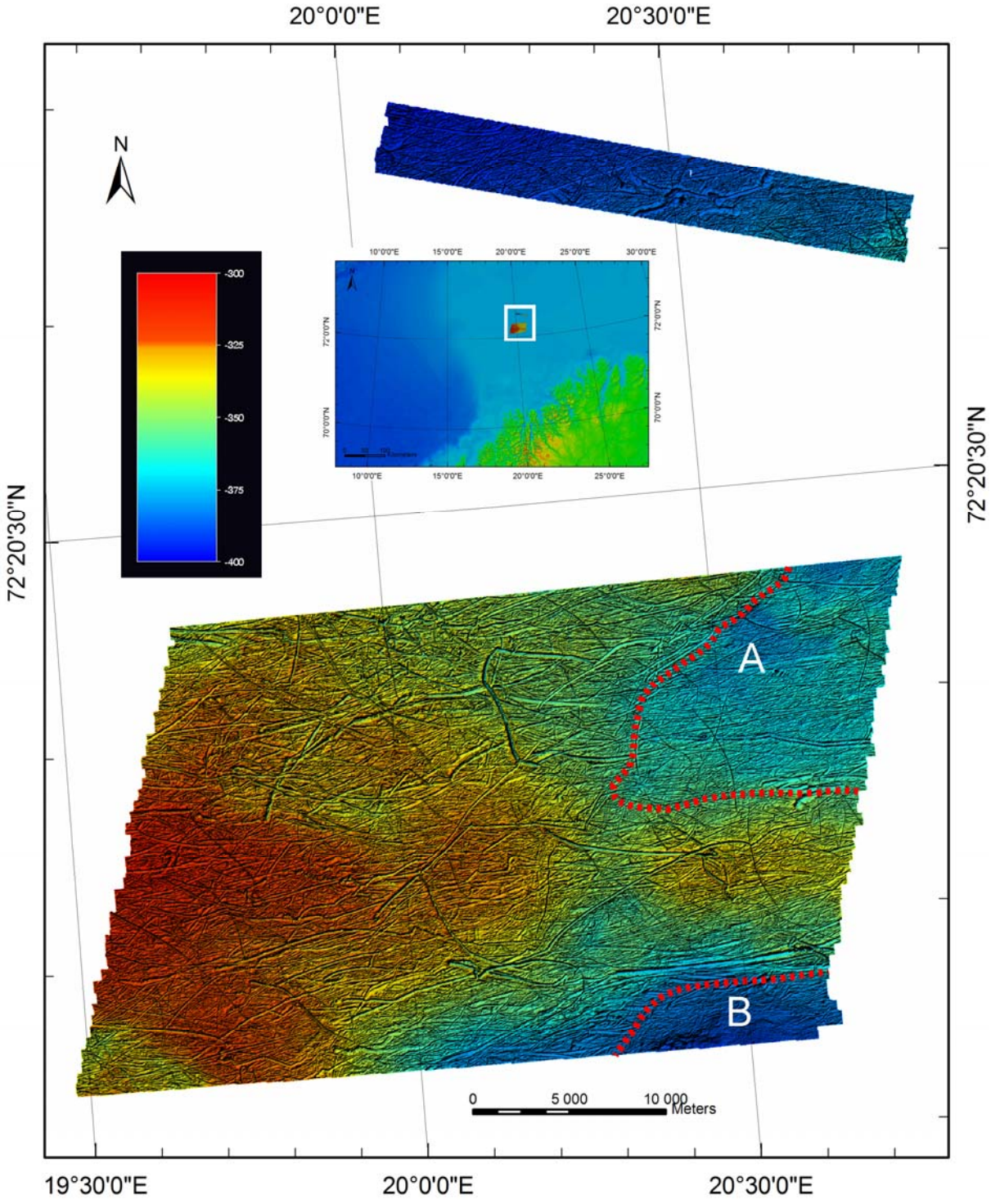

Figure 3. Overview of water depths for the MBB area. The red stippled lines indicate boundary between areas with pockmarks (basins areas A and B) and areas with no or few pockmarks.

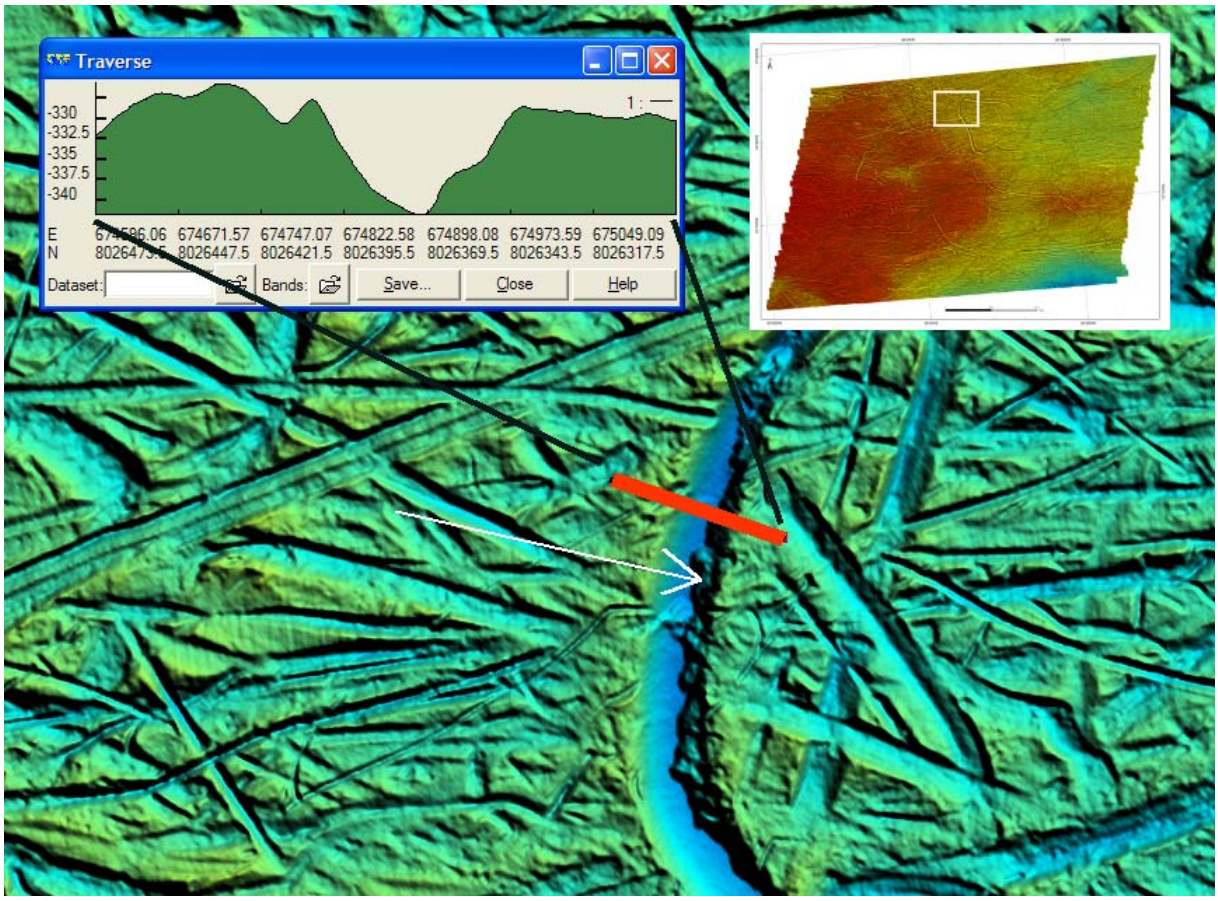

Figure 4. Nearly 15 m deep iceberg ploughmark. Note slump deposits along the eastern margin (arrow).

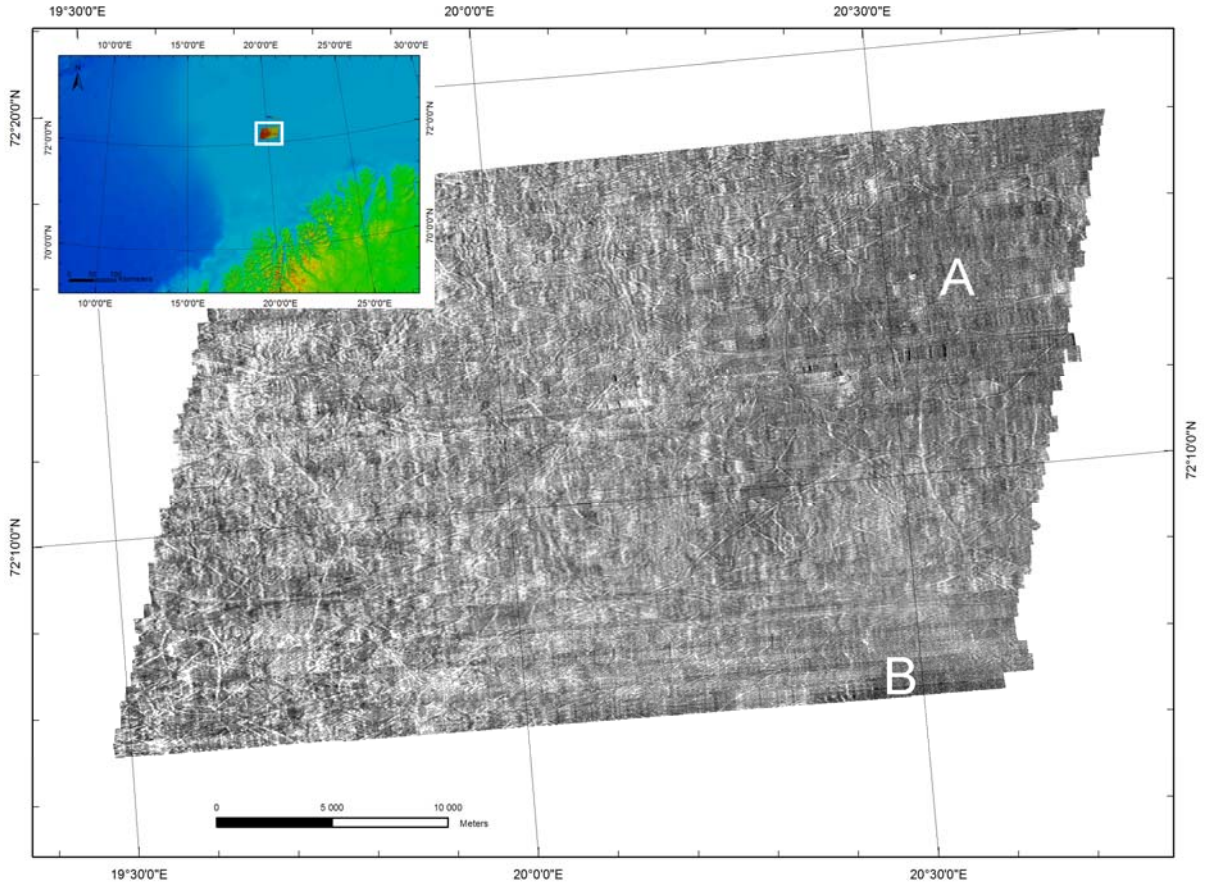

Figure 5. Backscatter data from the southern MBB area. Note low reflectance in basin areas A and B.

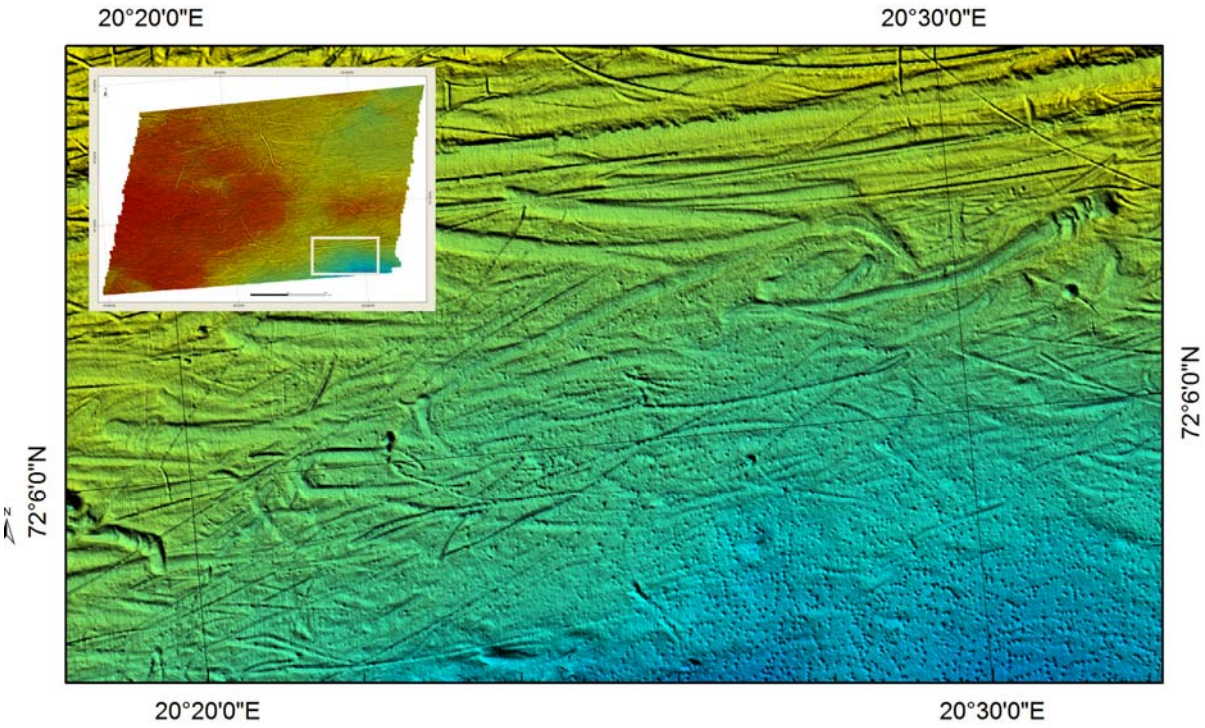

Figure 6. Part of basin B, showing how soft sediments (lower right corner) cover iceberg ploughmarks.

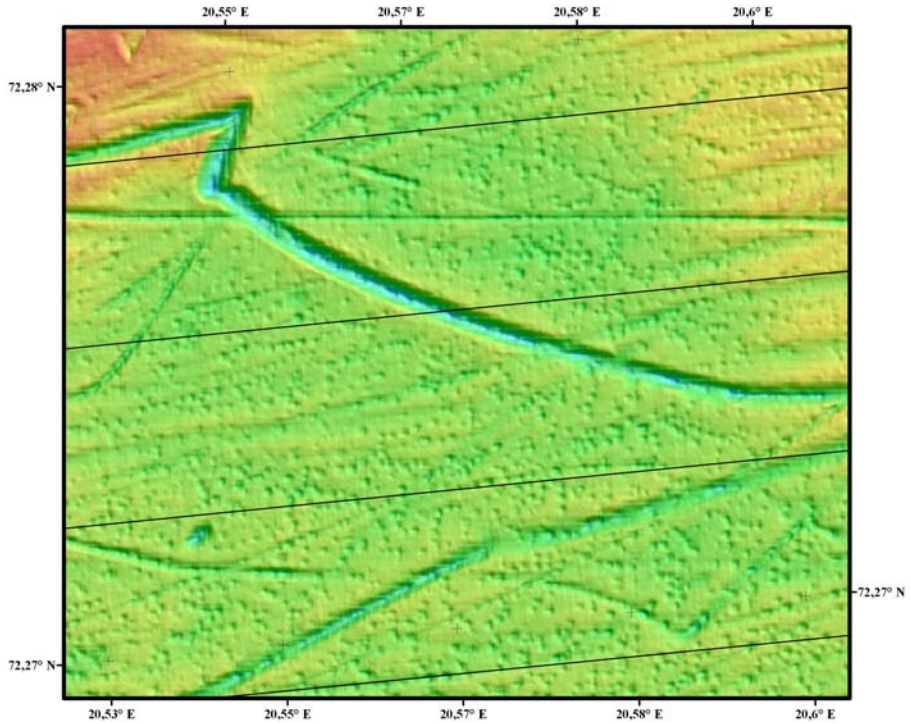

Figure 7A. Detailed bathymetry from basin A (Fig. 5) showing coexistence of pockmarks with iceberg ploughmarks. Black lines indicate ship tracks.

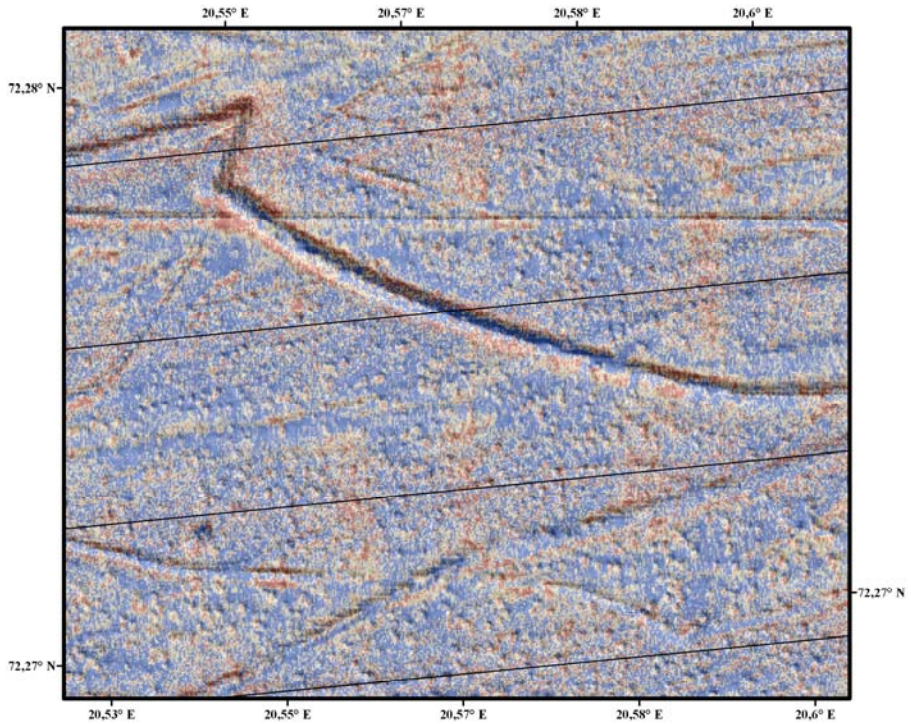

Figure 7B. Detailed backscatter of the area shown in Fig. 7A from basin A (Fig. 5) showing backscatter signatures of pockmarks and iceberg ploughmarks. Notice high backscatter (red) associated with pockmarks and at the rims of ploughmarks.

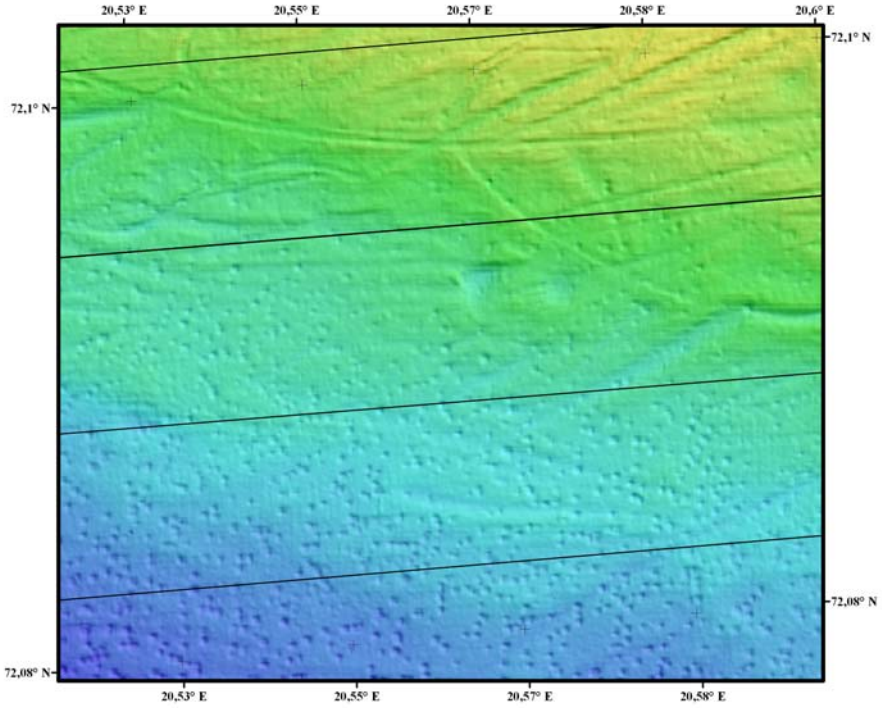

Figure 8A. Detailed bathymetry from basin B (Fig. 5) showing co-existence of pockmarks in recent sediments and partly buried iceberg ploughmarks.

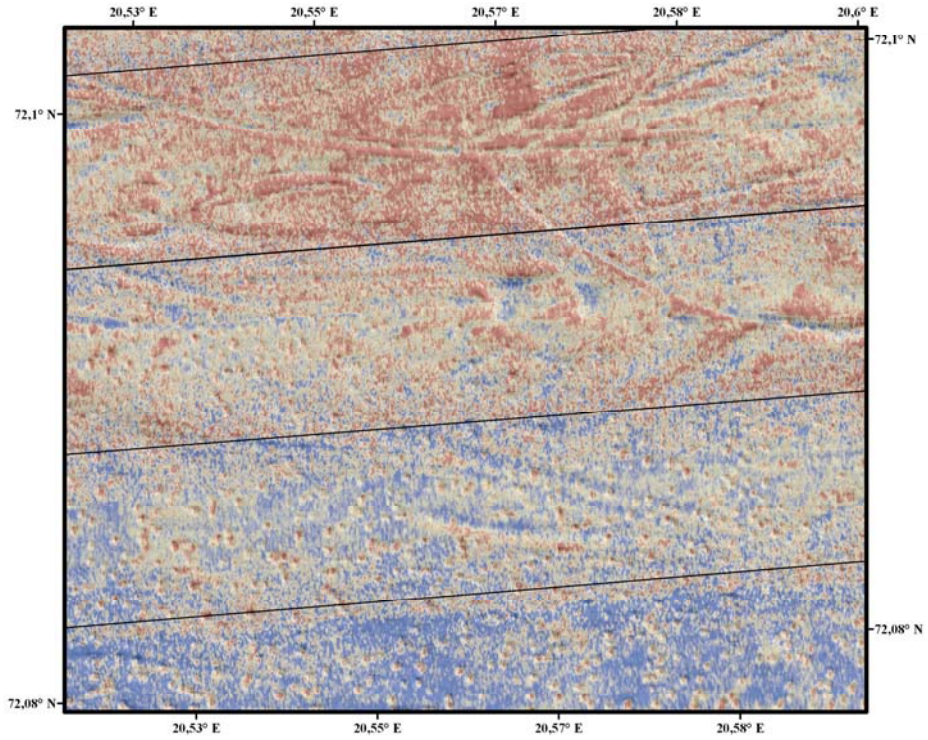

Figure 8B. Detailed backscatter of the area shown in Fig. 8A from basin B (Fig. 5) showing backscatter signatures of pockmarks and iceberg ploughmarks. Notice high backscatter associated with pockmarks and at the edges of ploughmarks.

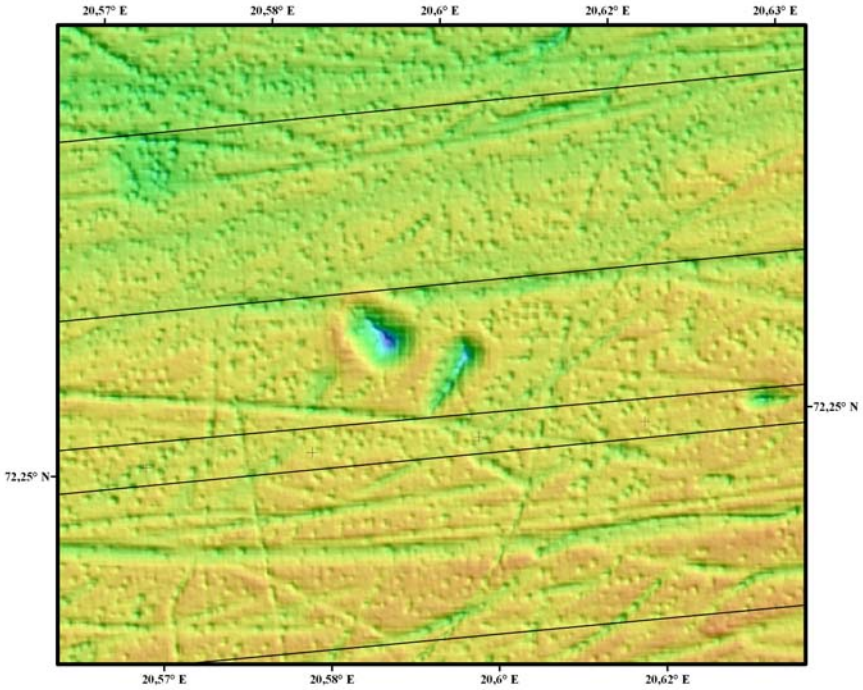

Figure 9A. Detailed bathymetry from pockmark area showing a large pockmark-like feature from basin A (Fig. 5) in coexistence with smaller pockmarks and iceberg ploughmarks.

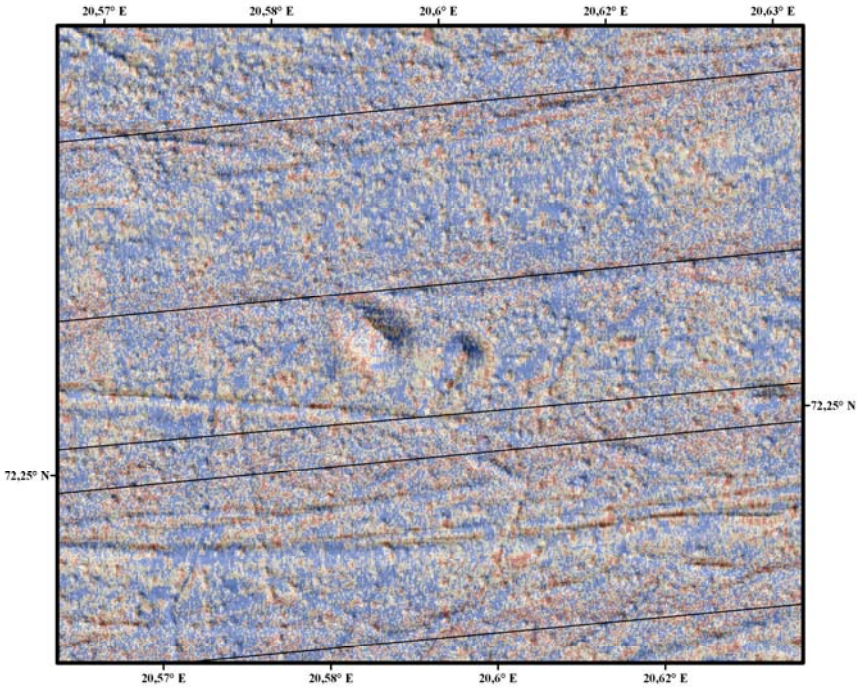

Figure 9B. Detailed backscatter of the area shown in Fig. 9A from basin A (Fig. 5) showing backscatter signatures of pockmarks and iceberg ploughmarks. Notice high backscatter associated with pockmarks and at the rims of ploughmarks. The large pockmark-like features have high backscatter rims indicating a probable iceberg plunging/ploughing origin.

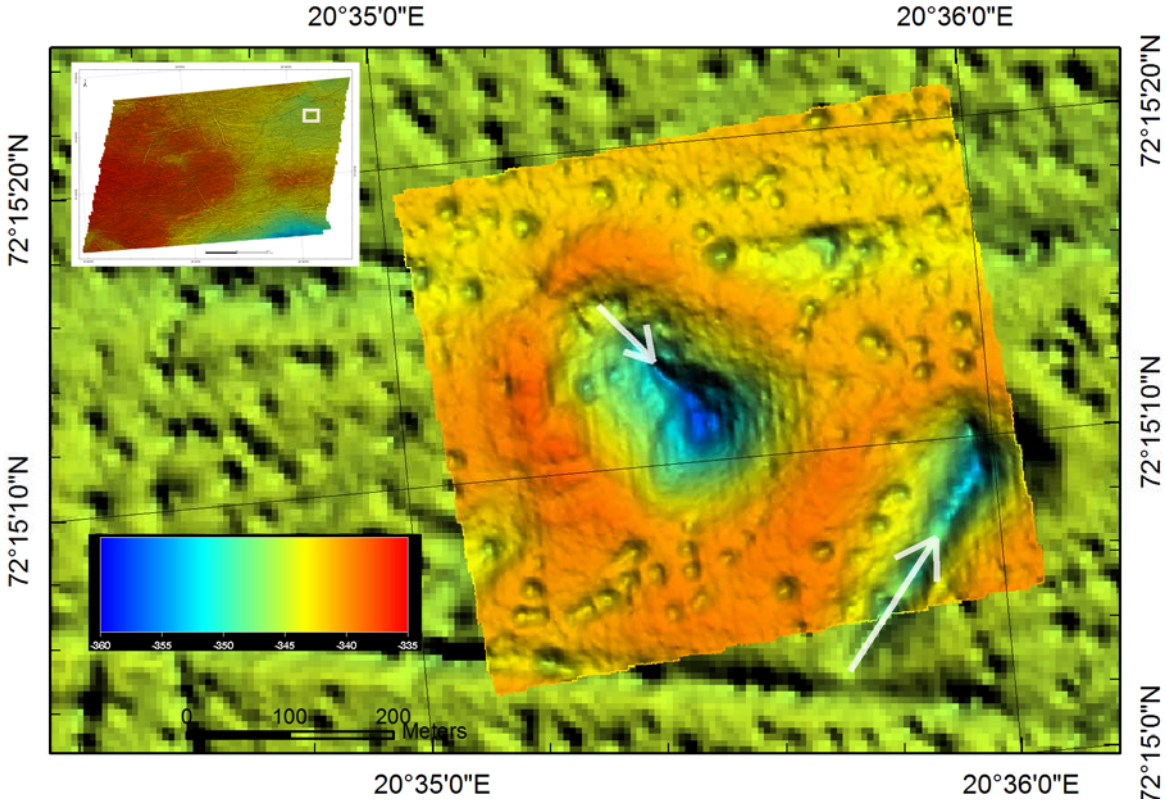

Figure 10. Large irregular pockmark (same as shown in Fig. 9A), 20 m deep. Bathymetry grid size around the large pockmark is 1 m, while it is 5 m in the background. Both pockmarks are asymmetric, indicating an origin as a mega-scale prod mark. Iceberg drift direction is indicated by arrows.

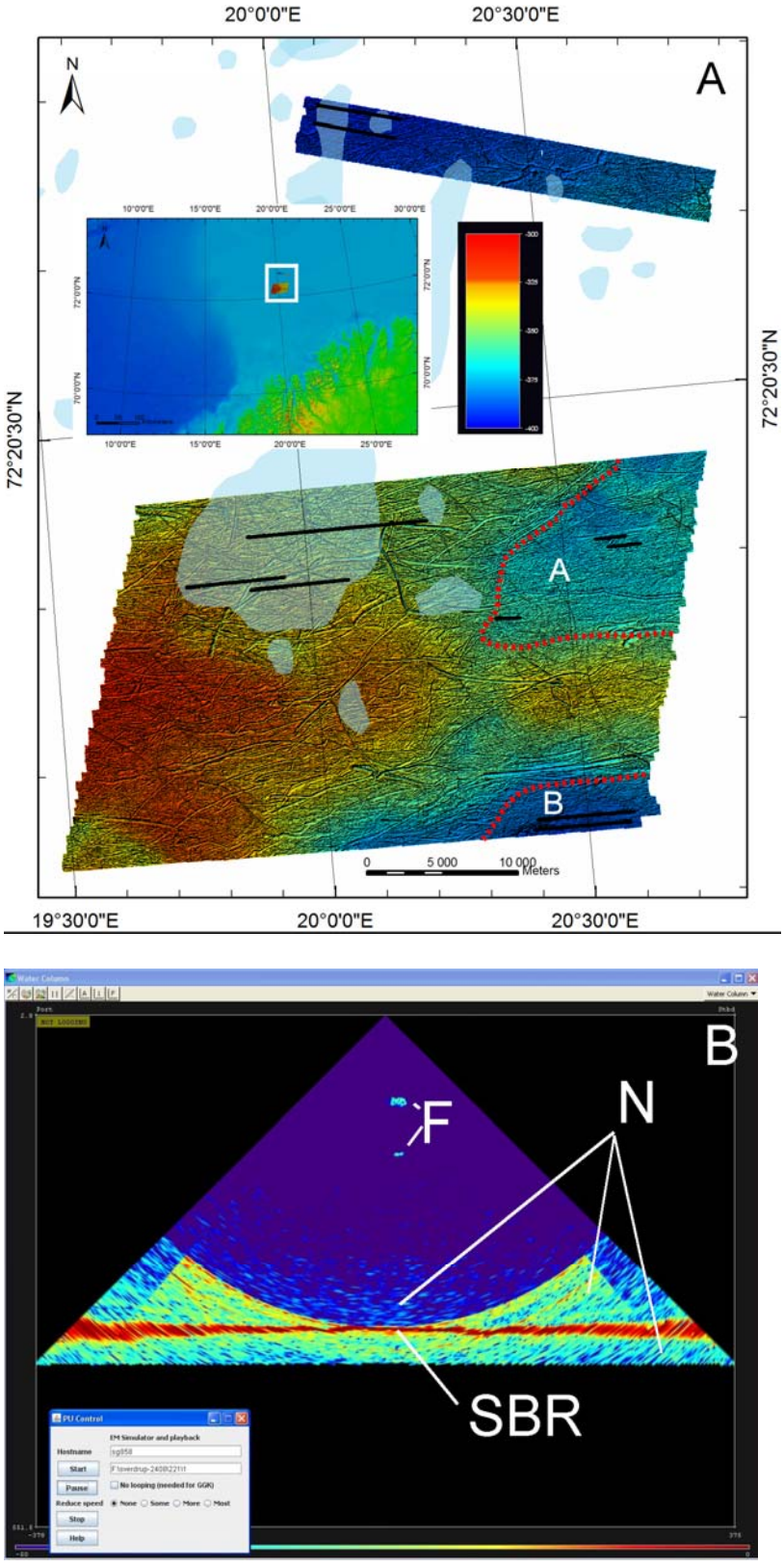

Figure 11. A) Overview map showing the distribution of investigated lines (black lines), and BSR occurrences and gas anomalies (blue transparent polygons, from Andreassen & Hansen, 1995). B) Example_Fish_school: Screen dump from the Kongsberg SIMRAD SIS software. F – fish schools; N – noise; SBR – seabed reflector. Width of view – c. 750 m.

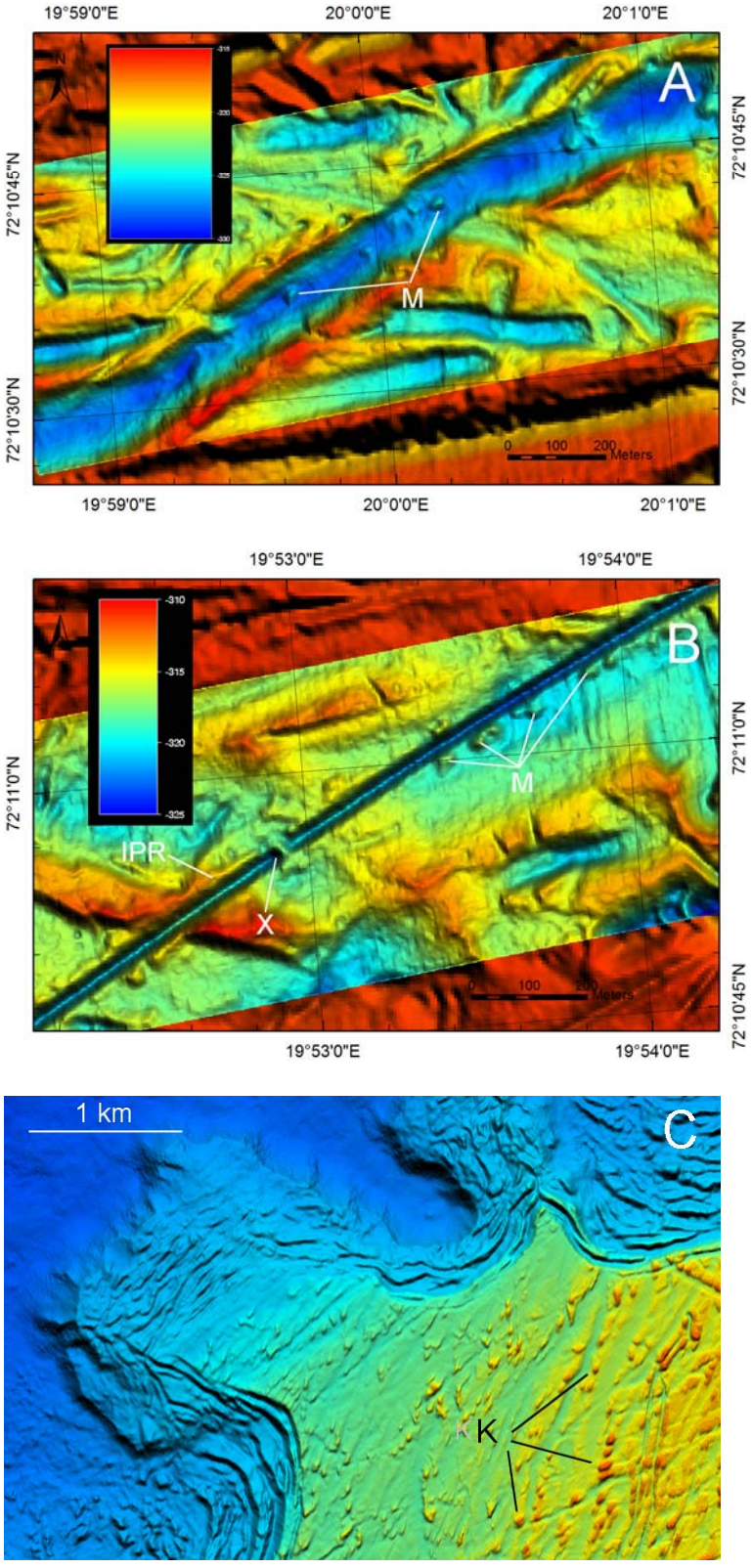

Figure 12. A and B: Examples of possible biogenic structures (M – mounds; X – cross-cutting structures) and glacigenic structures (IPR – iceberg ploughmark ridges). C: Coral reef mounds (K) as they occur on the Røst Reef (water depth -400m on the shelf, and down to -600 m in the upper left (blue) part).

4.2 Gas hydrates and BSR

Occurrences of gas hydrates in marine conditions are often associated with the presence of a bottom simulating reflector (BSR) (Fig. 13). A BSR is a seismic reflector described as one which sub-parallels the seafloor reflection and is opposite in polarity (Shipley et al., 1979). The BSR indicates an acoustic impedance change across a high velocity layer of gas hydrate filled sediments overlying a gas filled layer (Stoll and Bryan, 1979). The BSR is paralleling the seafloor since the gas hydrate stability zone (GHSZ) is primarily decided by the hydrostatic pressure induced by the water column thickness (Fig. 13) (Sloan, 1990). The nature and properties of the BSR and their occurrences vary depending on the sedimentary environment and fluid flow (Chand and Minshull, 2003; Hobbro et al., 2005; Westbrook et al., 2008). It is observed in many parts of the world that the BSR depths are altered by the presence of one or more of the gas hydrate inhibitors (NaCl, N_2, warm fluids, isostatic uplift, sliding) or facilitators (CO_2, H_2S, higher order hydrocarbon gases, increase in sea level, subsidence). Hydrates formed from pure methane assumes molecular structure I while in the presence of higher order hydrocarbon gases it takes structure II. Structure I and II gas hydrates have different stability conditions and physical properties. Hence, it is complicated to interpret the presence of gas hydrates in areas with mixed gas origin with disturbed BSRs or region outside methane hydrate stability, where entire gas hydrates are formed as structure II type. The most often observed anomaly in gas hydrate provinces is a palaeo BSR, which is described as occurring due to a shift in sea level. The BSR is also shifted due to the influx of warm or salty fluids from below, altering gas hydrate stability conditions (Fig. 14) (Holbrook et al., 2002; Hustoft et al., 2009). In such places, high amplitude reflections below and above methane hydrate stability depths could be due to gas hydrate patches which are often misinterpreted as gas anomalies (Figs. 14 and 15). It has been observed and modeled that gas hydrates could give similar anomalies as gas due to their high acoustic impedance contrast and attenuative properties with surrounding non-hydrate bearing sediments (Chand et al., 2004; Chand and Minshull, 2004; Chand et al., 2005) (Fig. 15).

The detection of BSRs is also complicated due to their variation in properties depending on the frequency used and the kind of boundary formed at the base of the GHSZ (Vanneste et al., 2001) (Fig. 16). Often GHSZ is controlled by the presence of permeable layers and the presence of a BSR is limited to locations where such layers cross cut the GHSZ (Fig.17). Gas hydrates are associated with high acoustic compressional and shear wave velocities and attenuations (Figs. 18 and 19) (Guerin et al., 2002; Chand and Minshull, 2004). An example from the Barents Sea indicated patchy, high amplitude reflections, which is interpreted as due to a BSR formed from structure II gas hydrates (Fig. 20) (Laberg et al., 1998). It has been modeled that the area where these anomalies are observed lie outside the methane hydrate stability conditions, and only gas composition of methane with higher order hydrocarbon gases or CO_2 can form gas hydrates. A similar study carried out along the western flank of

Ingøydjupet indicated patchy reflections in the subsurface but again the region is outside methane hydrate stability zone (Fig. 21) (Chand et al., 2009). No drilling has been carried out for hydrate sampling along the Barents Sea margin, but a surface gravity core from the Nordkapp Basin indicated presence of hydrate (Chand et al., 2008). High amounts of CO_2 (up to 78%) is reported from south of our study area in well 7019/1-1 along the Tromsø Basin, indicating that CO_2 may be of importance while modelling gas hydrate stability for this region (NPD well report 7019).

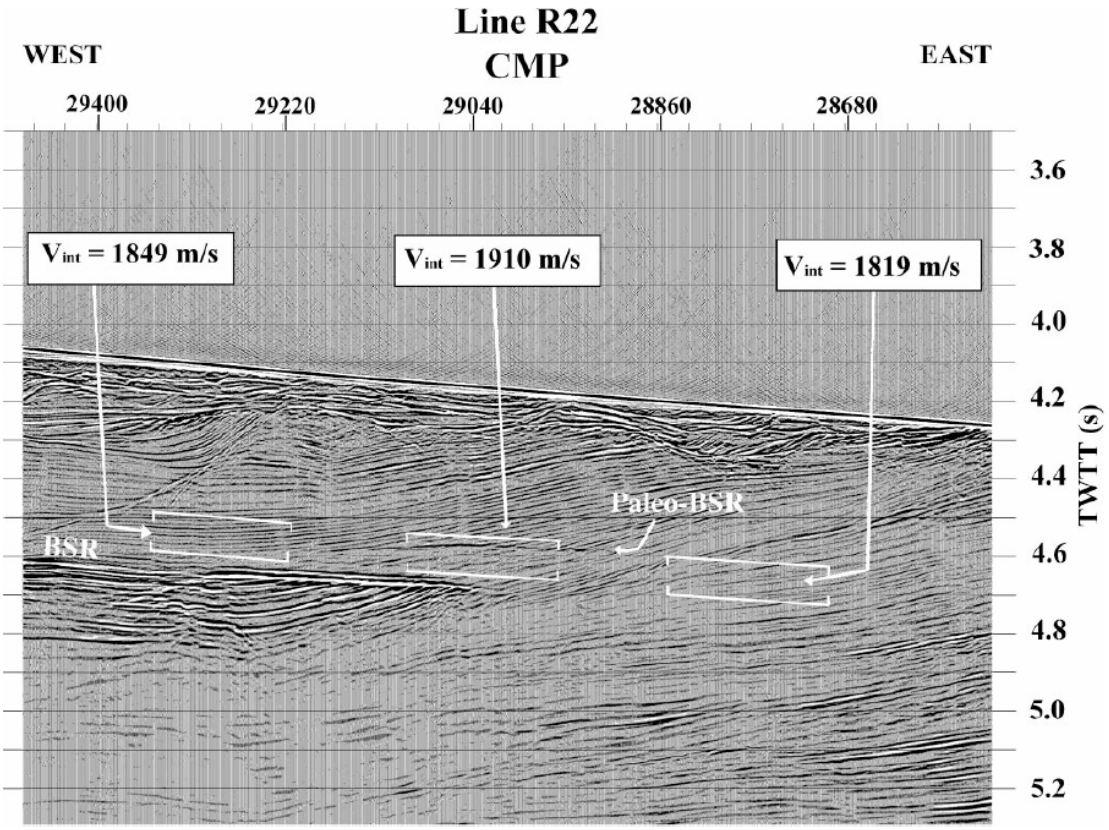

Figure 13. Example of a continuous bottom simulating reflector (BSR) from Blake Ridge. Amplitude blanking shown in the figure is still not considered as genuine, since many places blanking is more representative of the sediment uniformity in a gas devoid environment (Hornbach et al, 2003).

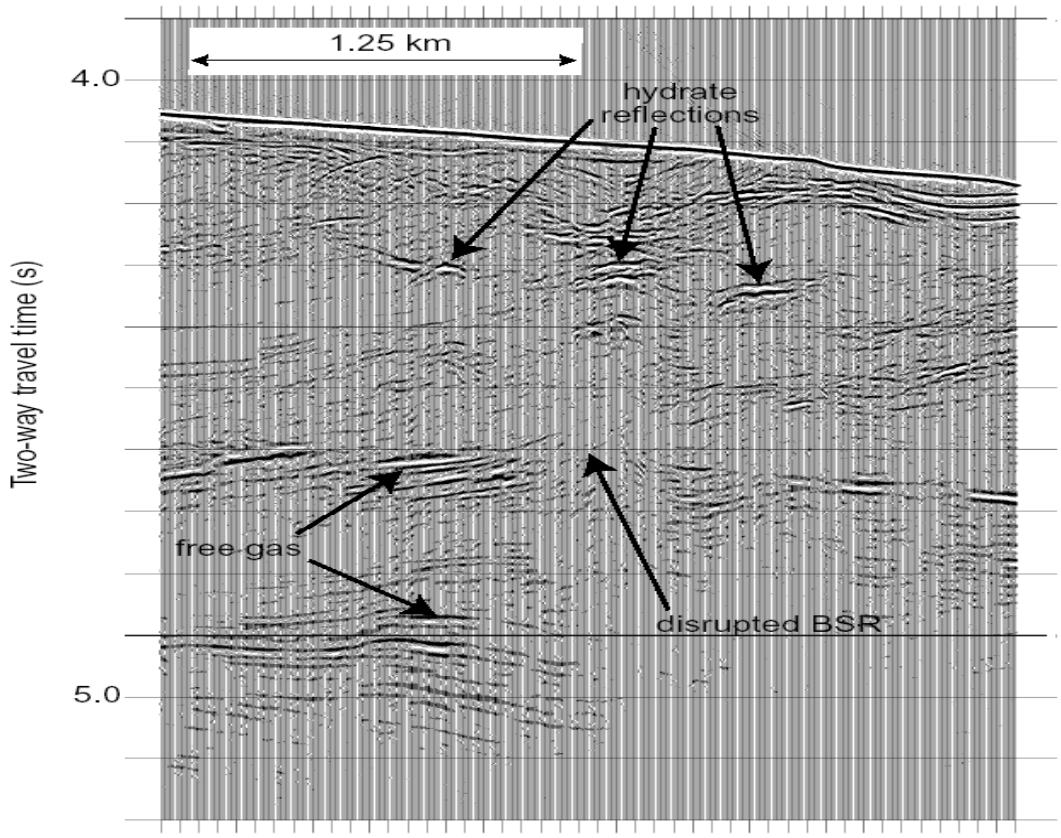

Figure 14. Disrupted BSR or gas hydrate anomalies within methane hydrate stability region from Blake Ridge (Holbrook et al., 2002).

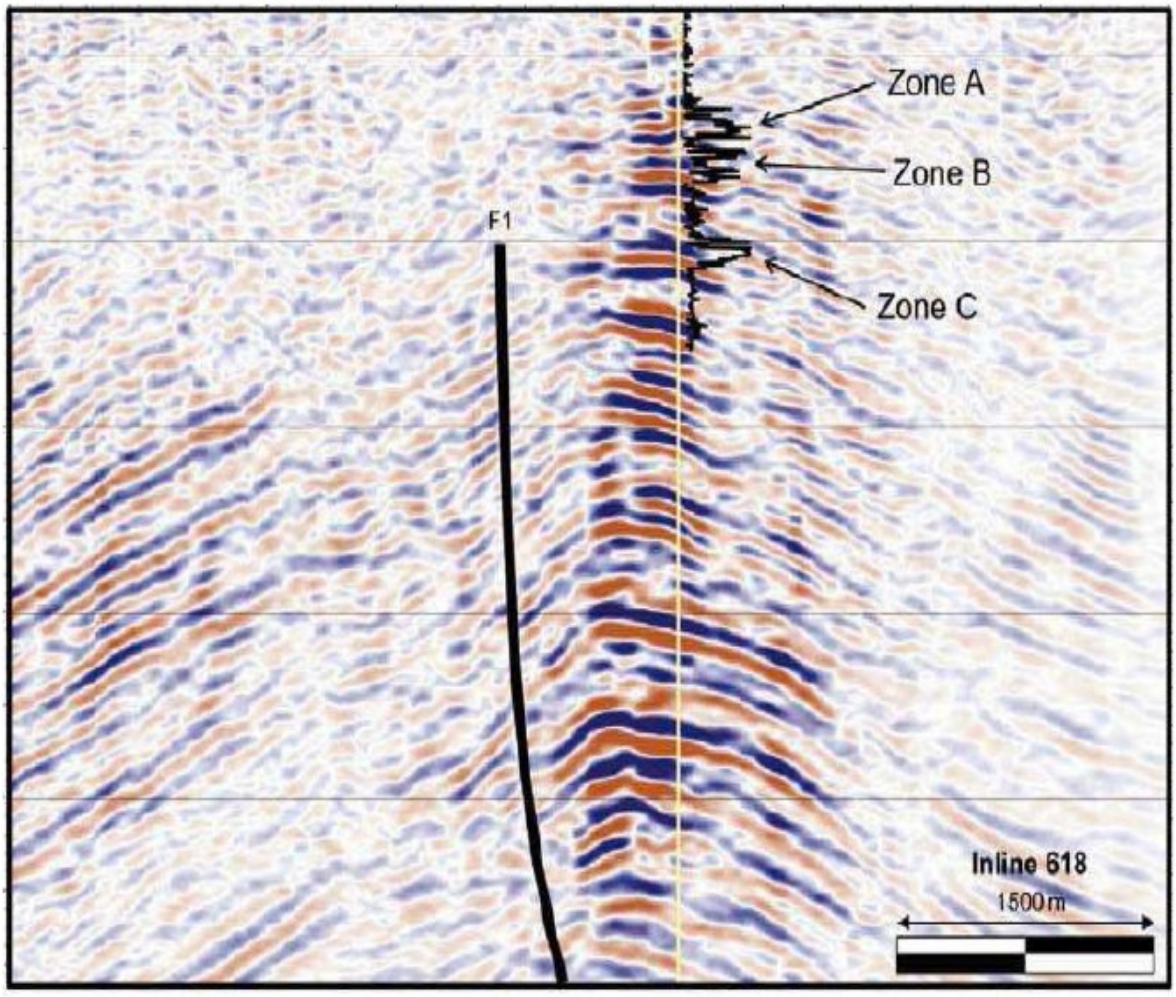

Figure 15. Gas hydrate region from the Mallik well showing gas-like reflections within and below methane hydrate stability depths. Also shown is the sonic log showing the high gas hydrate concentration zones (Bellefleur et al., 2006).

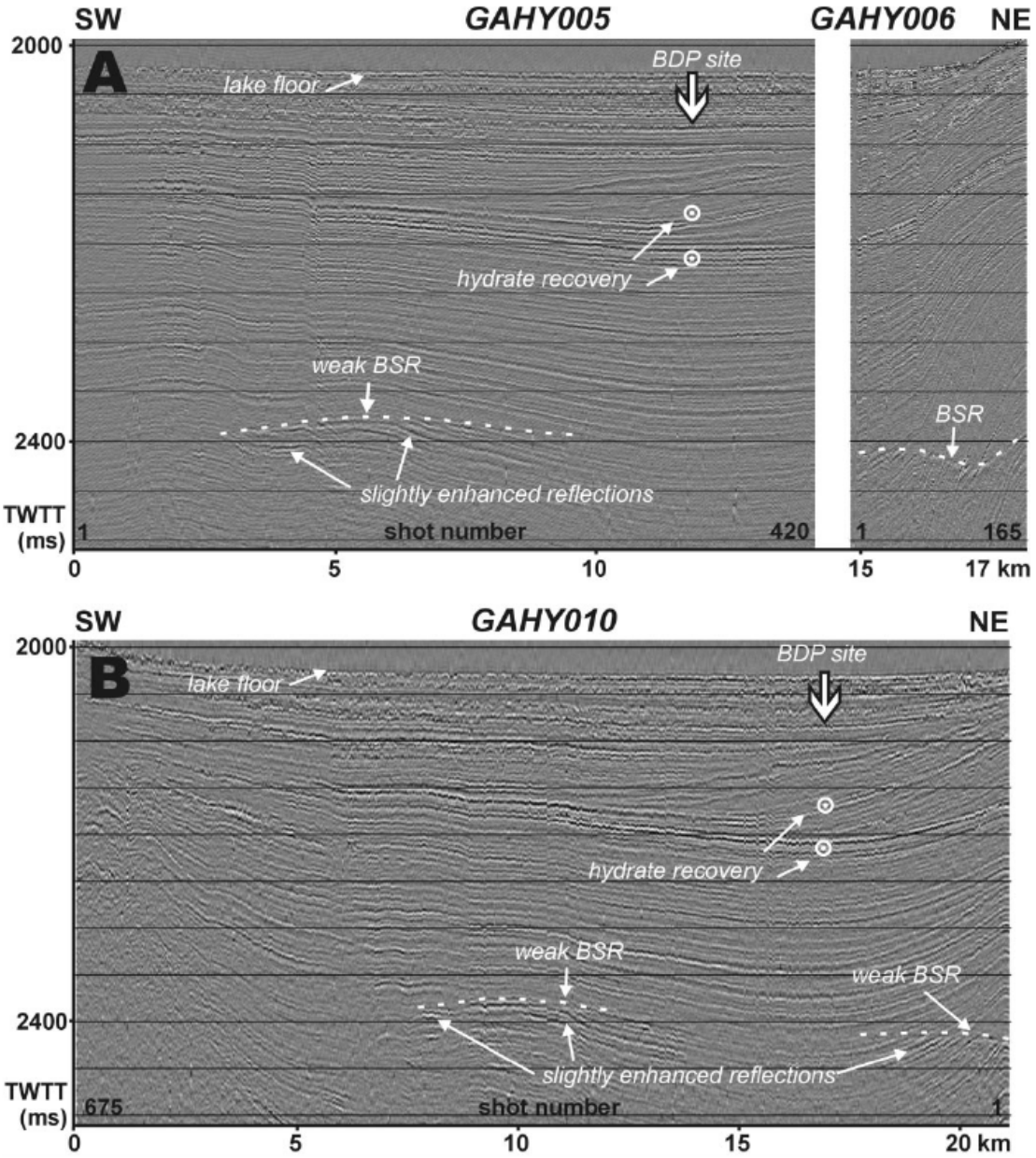

Figure 16. High frequency single airgun data showing very feeble BSR signature in a gas hydrate zone from lake Baikal. Notice that there is no BSR beneath the gas hydrate recovery site (Vanneste et al., 2001).

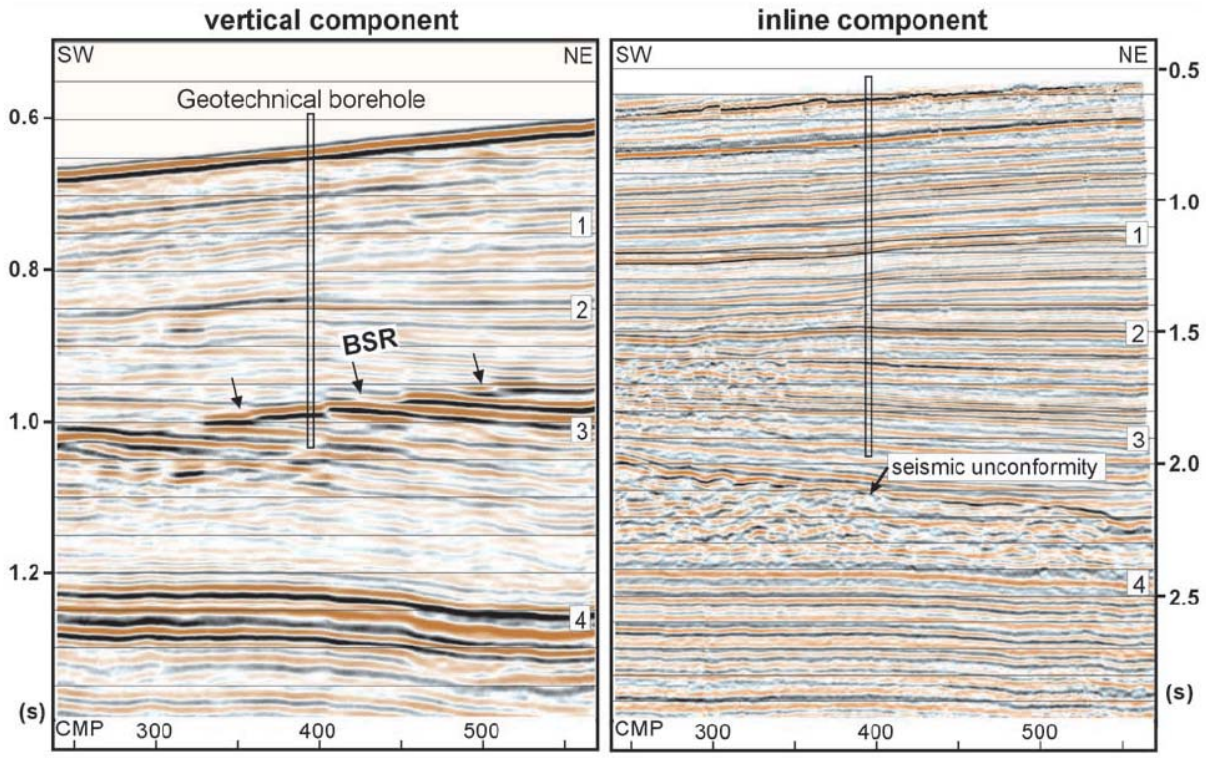

Figure 17. OBC data from the BSR zone within the Storegga Slide area, offshore Norway showing the seismic signatures across a BSR in a low gas hydrate concentration zone (Buenz and Mienert, 2004). The BSR is shown up as a change in amplitude across a permeable layer in the PP section (vertical component) while such anomalies are absent above and below layers. Due to low concentration of gas hydrates no significant anomaly is produced in the PS section (inline component).

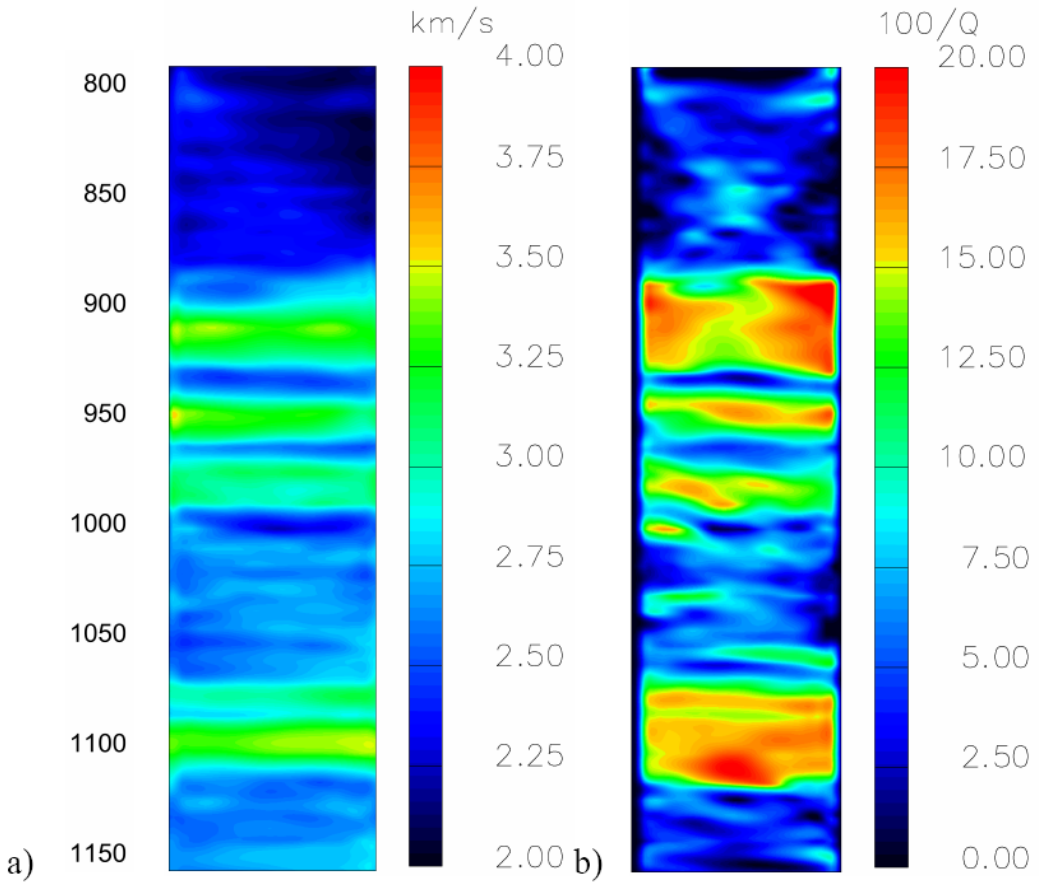

Figure 18. VSP derived P wave a) velocity and b) attenuation from Mallik 2L 38 well Mackenzie delta Canada showing the distinctive acoustic properties of hydrate bearing sediments (Pratt et al., 2003)

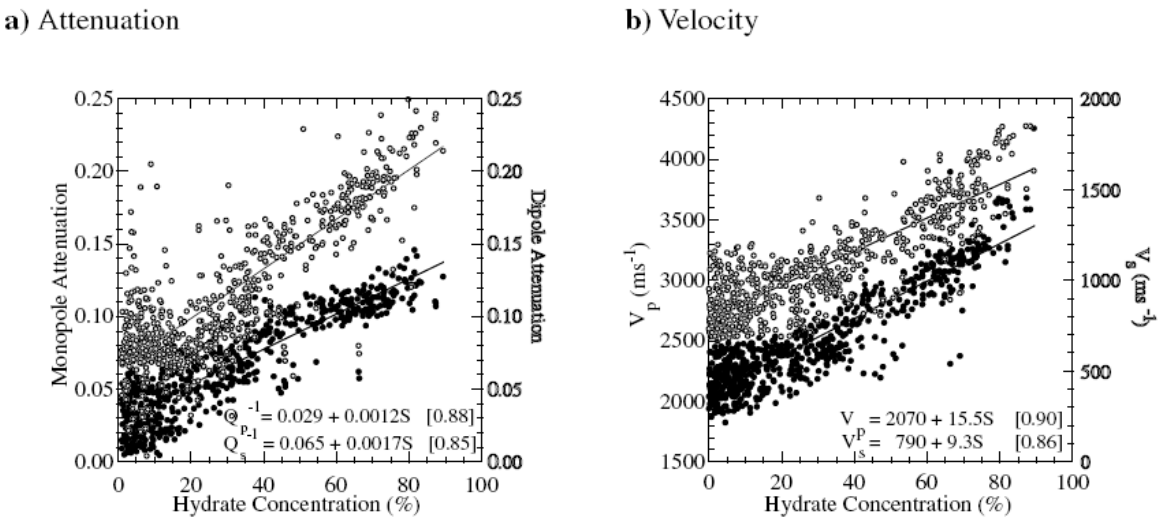

Figure 19. Log derived P and S wave a) attenuations and b) velocities in hydrate bearing sediments at Mallik 2L-38 well Mackenzie delta, Canada (Guerin and Goldberg, 2002). The hydrate bearing sediment velocities and attenuations increase with hydrate saturation.

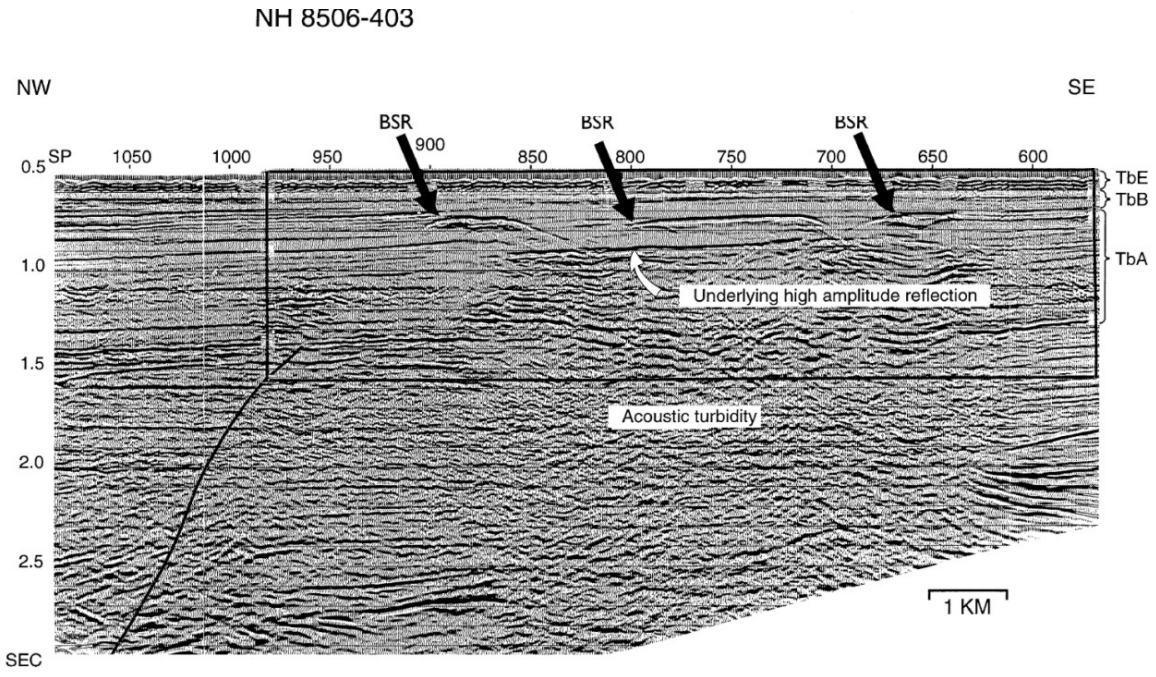

Figure 20. Example from the Barents Sea showing patchy reflections which are interpreted as due to gas hydrates (Laberg et al., 1998).

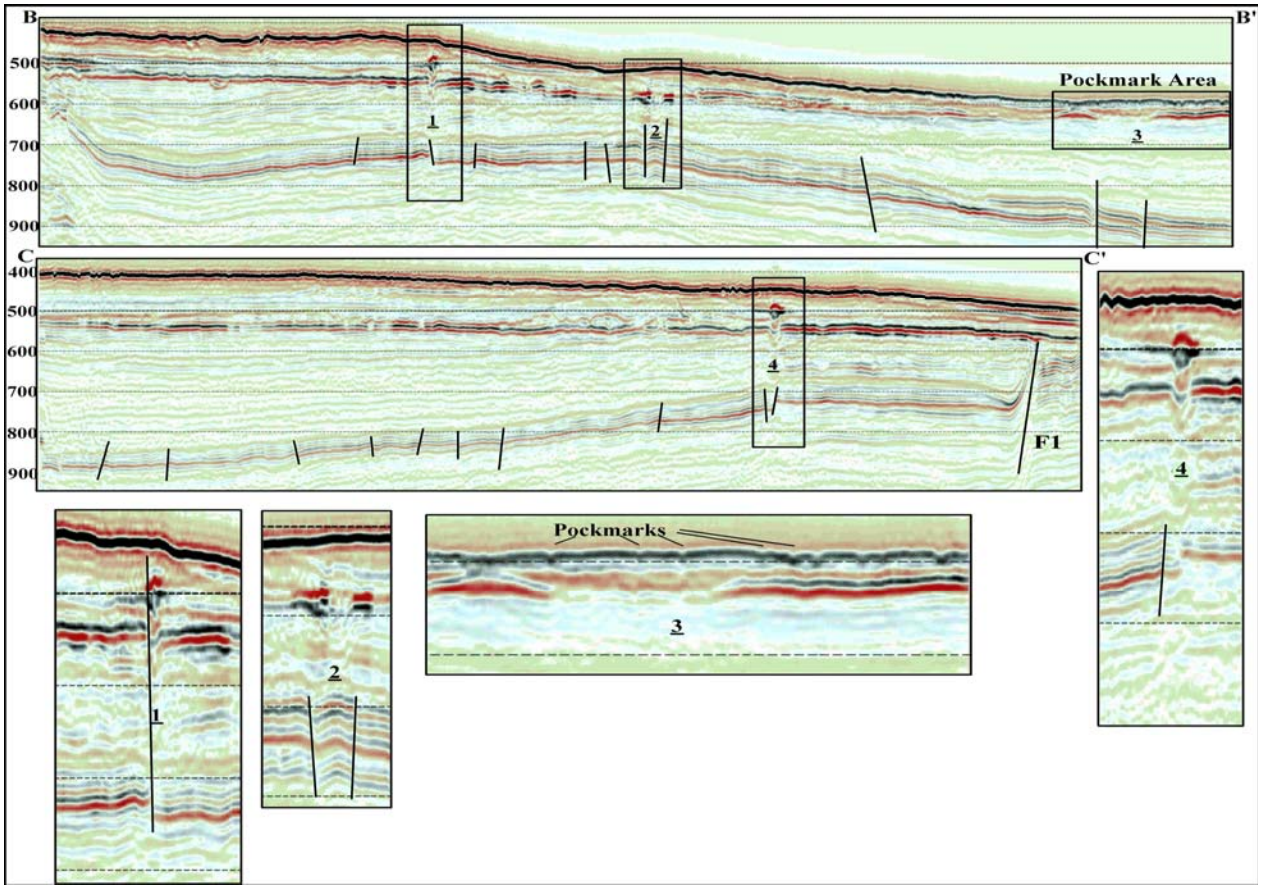

Figure 21. Patchy high amplitude reflections close to the seafloor in and around region of pockmarks indicating active fluid flow blocked by the possible presence of gas hydrates (Chand et al., 2009).

Based on knowledge from various projects and the background information about gas hydrates, a thorough analysis of the 2D and 3D seismic data was carried out. Gas anomalies and possible BSR anomalies are interpreted based on gas hydrate stability modeling. The regional gas hydrate stability depths estimated for the Barents Sea (Chand et al., 2008) was modified based on more accurate bathymetry, a geothermal gradient of 32^{o} C/km and various gas compositions and formation water salinities (Fig. 22). It has been found earlier that the BSR observed partly covering our study area is best described by a gas composition consisting of 96% methane, 3% ethane and 1% propane (Laberg et al, 1998). The estimated two way time (TWT) milliseconds (ms) thickness of the gas hydrate stability zone is around 250-300 ms assuming an 1800 m/s velocity for the sediments (220-270 ms TWT using 1990 m/s velocity observed at well 7220, hereafter case 2) (Fig. 23). The total TWT to the GHSZ from the sea surface assuming 1470 m/s for the seawater ranges between 700 and 750 ms TWT (670-720 ms for case 2) (Fig. 24). The bathymetry data used for this calculation was from a regional dataset, and hence the accuracy of the GHSZ depths is within 20 ms TWT for that specific gas and geothermal gradient model assumed.

The high resolution 2D seismic acquired by FFI were used to map any possible gas and gas hydrate related anomalies. Industry 2D seismic data available from the study area were also interpreted for possible occurrences of gas and BSR anomalies. A compilation of all these anomalies and examples are given in Figs. 25 to 30.The 3D seismic data available south of the main study area was also interpreted for possible gas/BSR anomalies. The gas anomalies and fluid pathways through links upwards can be clearly noticed (Fig. 31). Selected profiles from the 3D seismic datasets are verified for gas anomaly variation with offset using near and far offset stacks of the same line (Fig. 32 & 33). Most of the anomalies have variation along the offset indicating they are real gas anomalies. But some anomalies are very weak to compare the difference mainly due to the reason that we picked fluid flow related anomalies also even if there is very limited amplitude brightening in the full stack data.

The TOC content of the shallow sediments from this area indicate low concentrations (1.21 to 1.4 %) with TC of 1.7-1.98% and $CaCO_3$ content of 4.84 to 5.26% from the borehole 7222/09-U-01 (Sættem et al., 1992). This will hence add the possibility of formation of gas and hydrate from microbial activity.

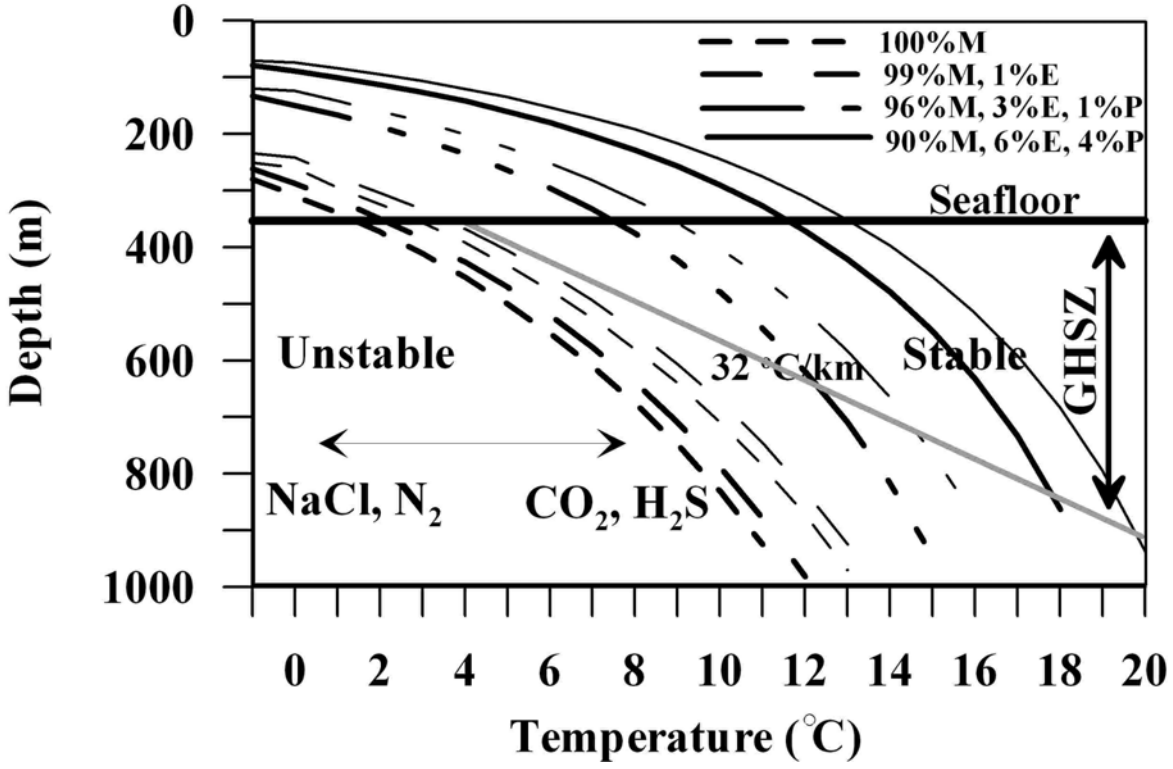

Figure 22. Hydrate stability curves for various gas compositions and salinities (thick: seawater; thin: fresh water). The region to the right of the geothermal gradient curve is GHSZ and the thickness of it is the difference between seafloor and where the geothermal gradient cuts the stability curve for the particulate gas composition. The bottom water temperature is taken from the World Ocean Database (WOD05) and varies between 1.5 and 5.5 ^{o}C within the area shown. A linear geothermal gradient is assumed from this sea bottom temperature. NaCl and N_2 are inhibitors for hydrate formation and makes hydrate unstable, while presence of CO_2 and H_2S facilitate hydrate formation at deeper depths than normal, predicted above.

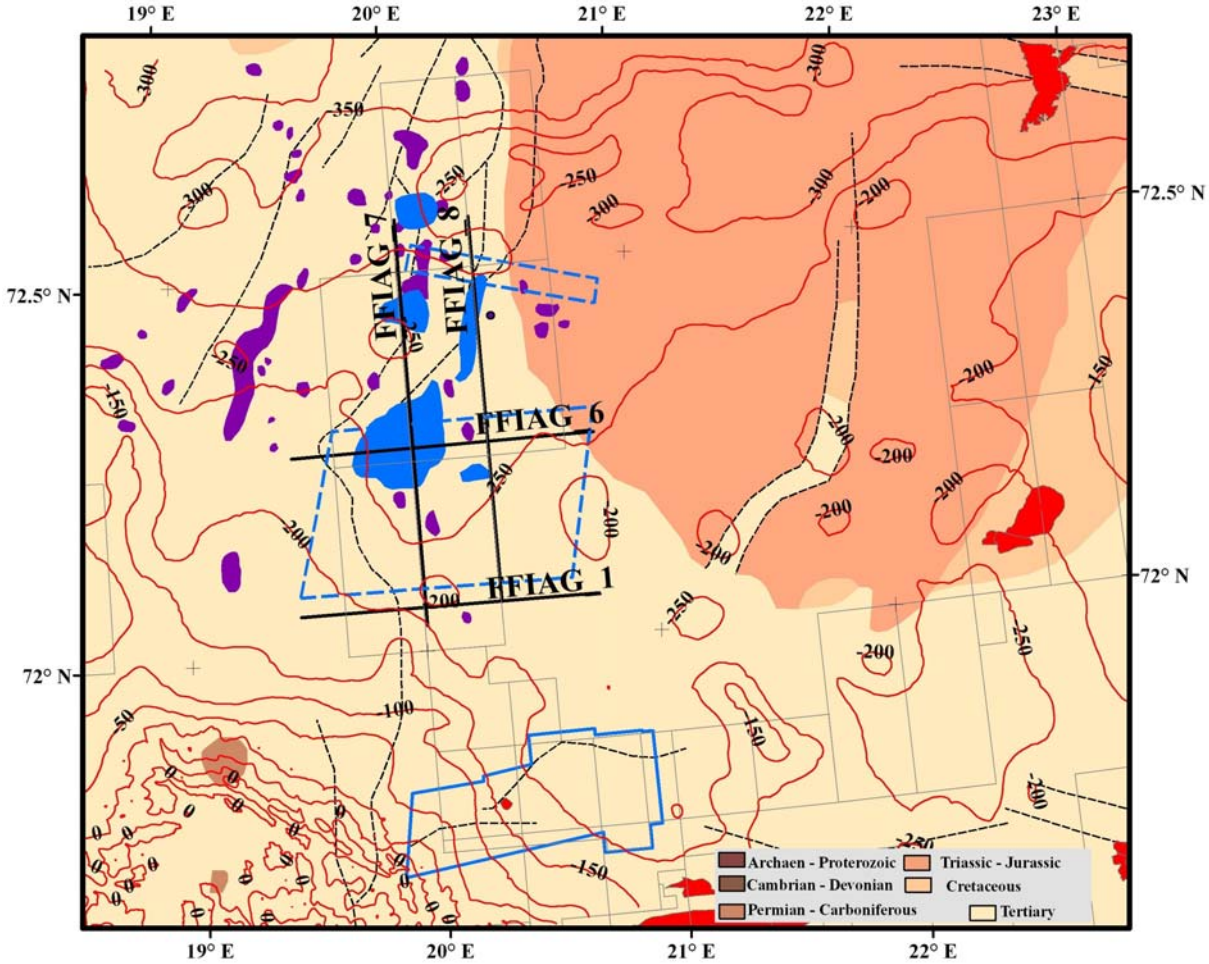

Figure 23. Two way time (ms, TWT) contour map of the GHSZ below seafloor shown on the structural map of the study area. The locations o MBB& 3D seismic datasets (blue polygons), and FFI 2D seismic profiles (black lines).

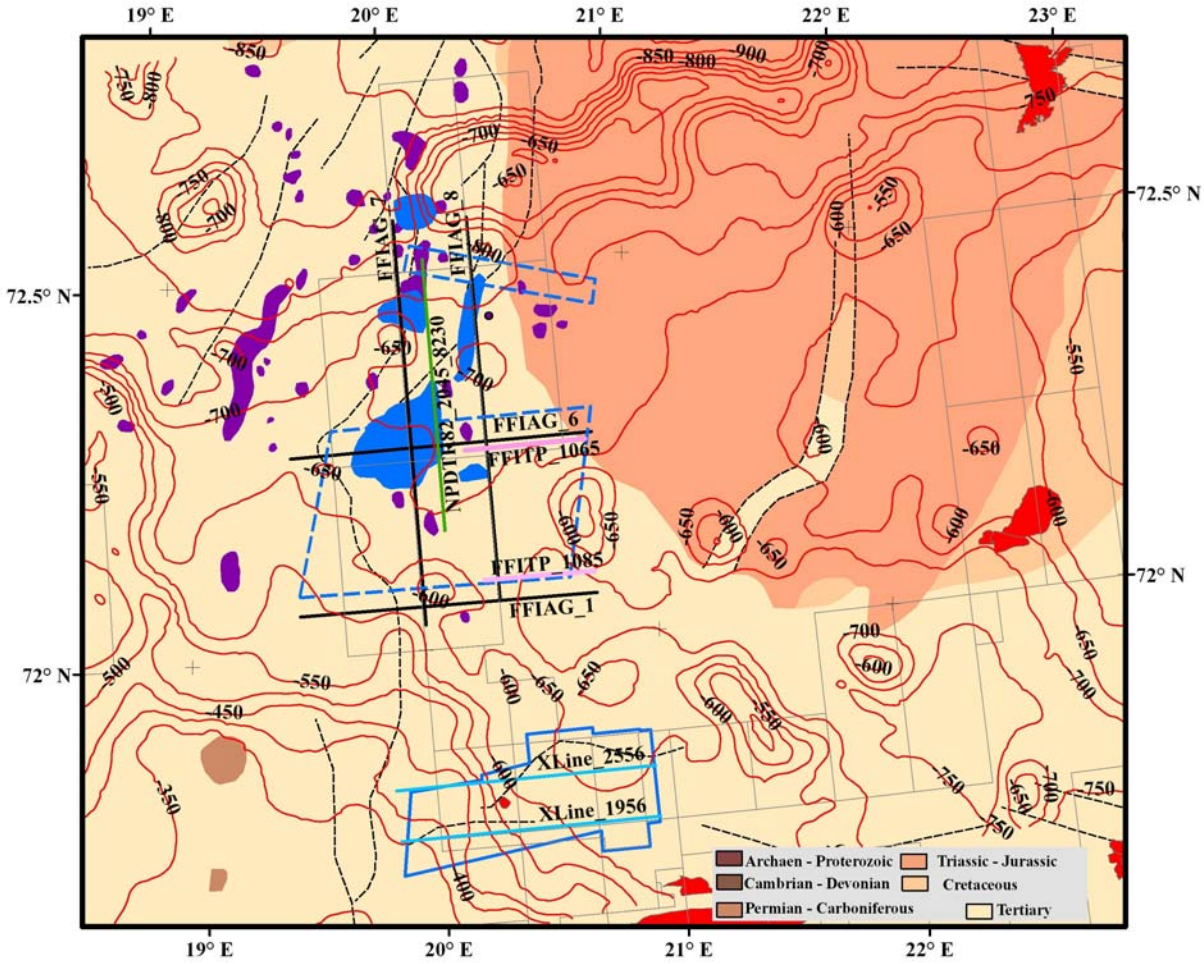

Figure 24. Two way time (ms, TWT) contour map of the GHSZ below sea surface shown on the structural map of the study area. Also shown is the TWT to base Tertiary (colour range 500 to 2500 ms), the locations of MBB & 3D seismic (LH08M01) datasets (blue polygons), and FFI 2D seismic profiles (black lines), two FFI TOPAS Seismic lines (pink), 2D industry seismic line NPDTR82_2045_8230 (green) and two cross lines from LHS08M01 (light blue).

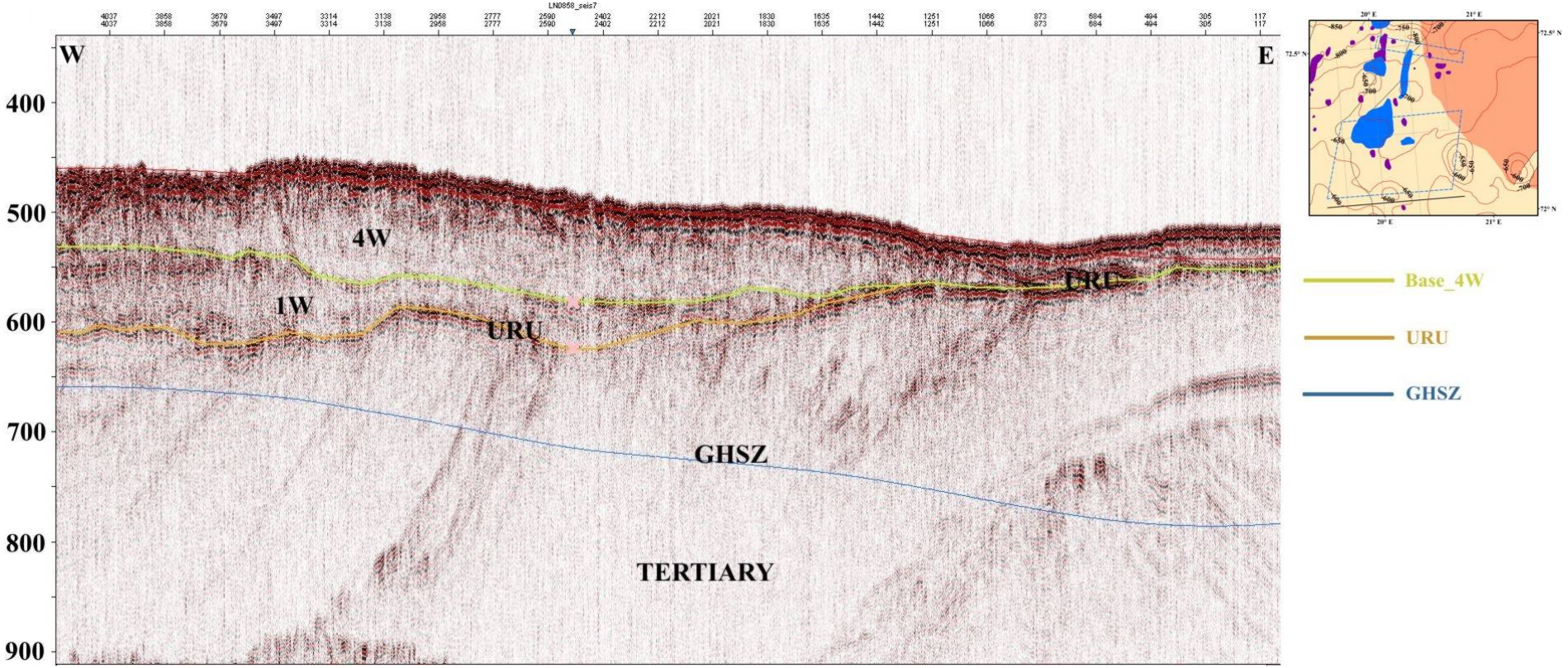

Figure 25. FFIAG_1 2D seismic line (see Fig. 24 for location) in W-E direction indicating gas anomalies below the URU (orange).

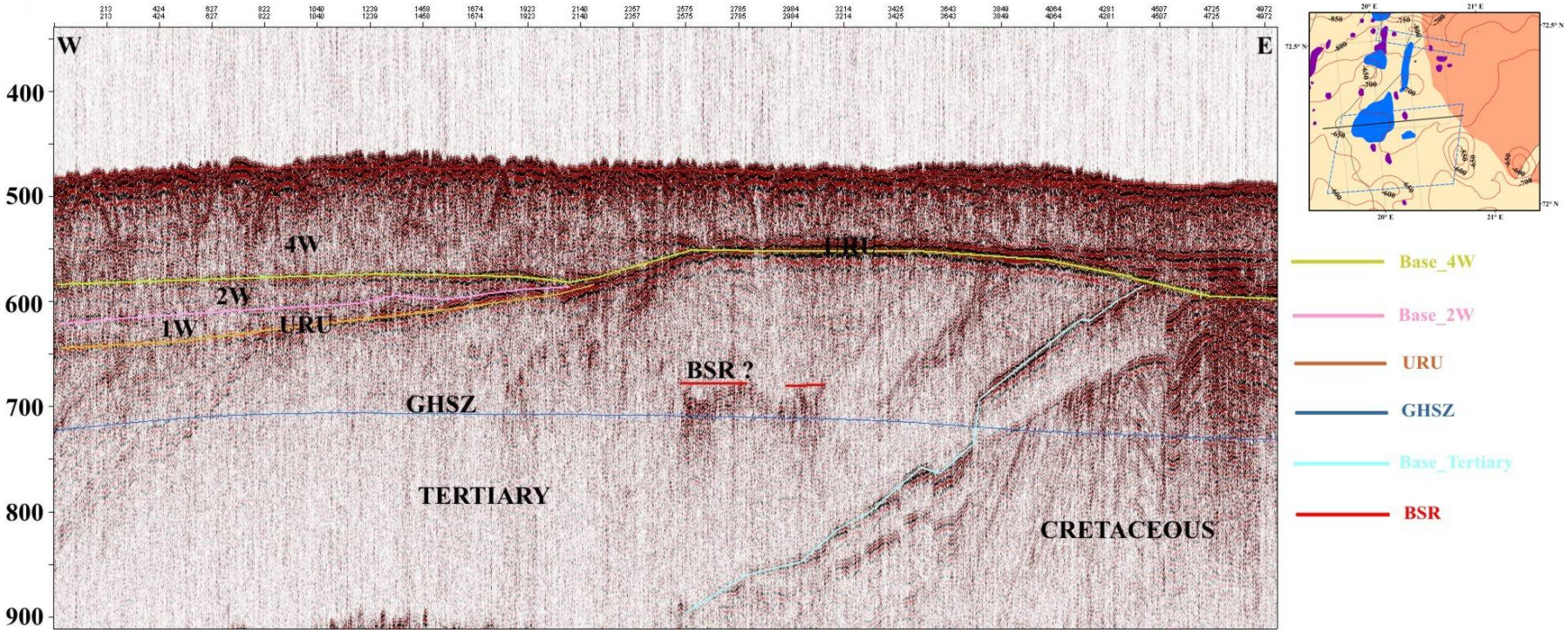

Figure 26. FFIAG_6 2D seismic line (see Fig. 24 for location) in W-E direction indicating gas anomalies below the URU (orange).

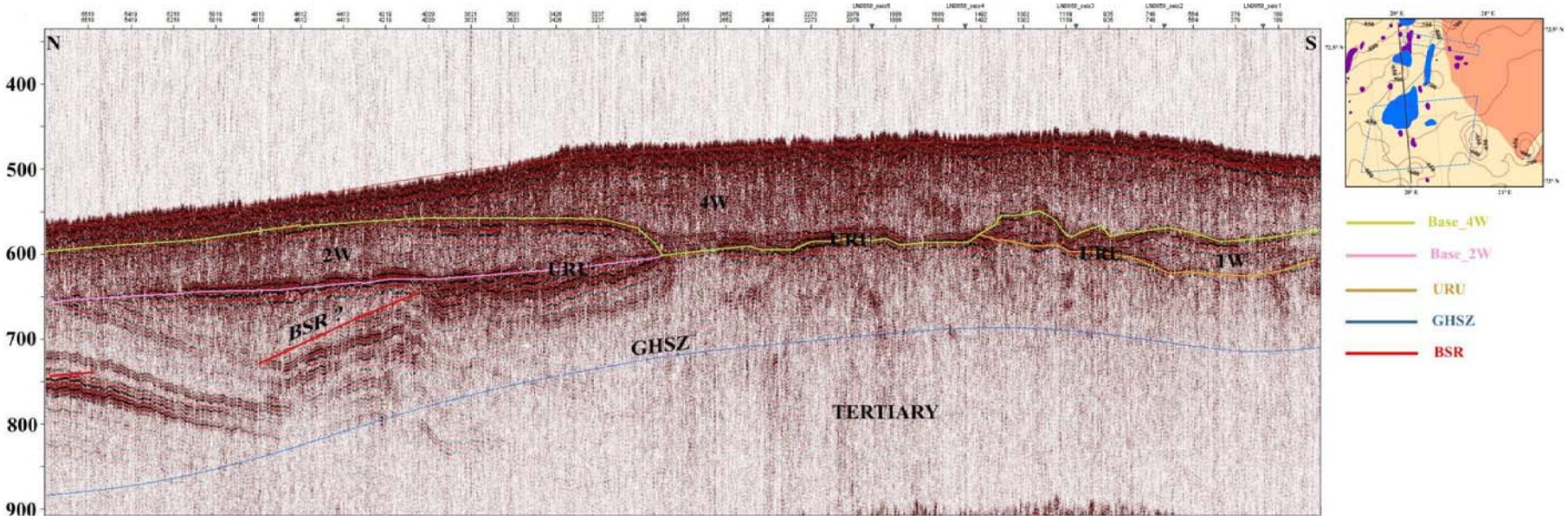

Figure 27. FFI AG_7 2D seismic line (see Fig. 24 for location) in N-S direction indicating gas anomalies below the URU (orange).

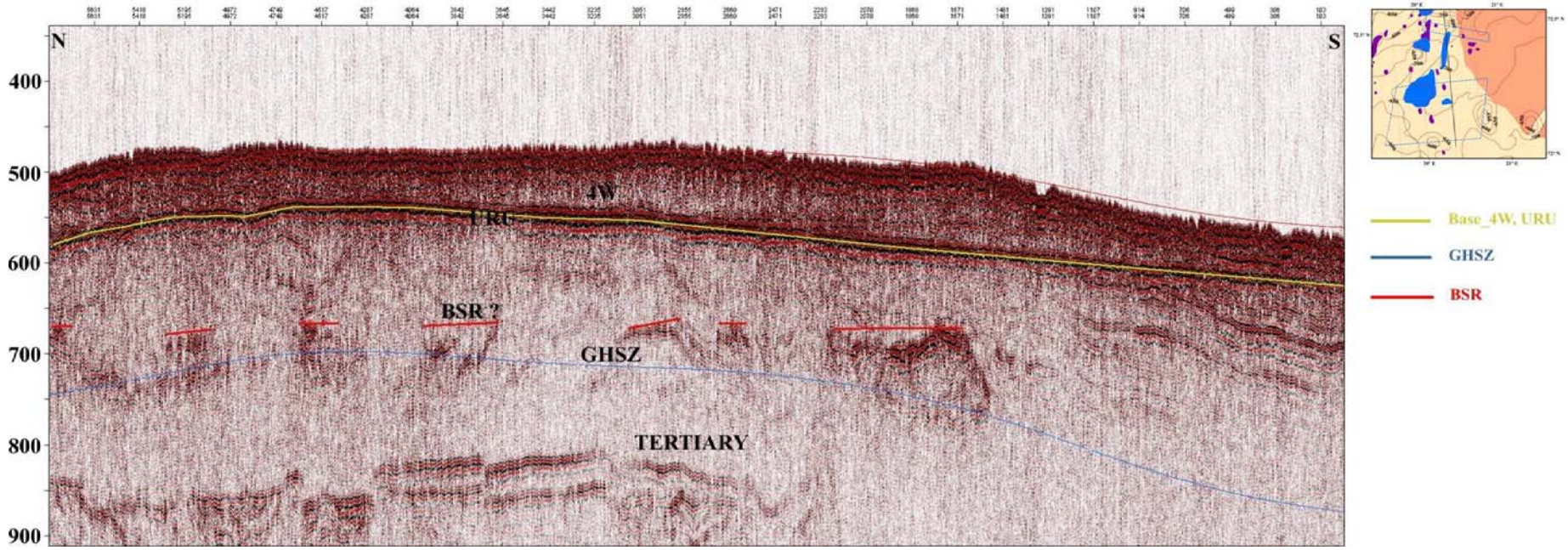

Figure 28. FFIAG_8 2D seismic line (see Fig. 24 for location) in N-S direction indicating gas anomalies below the URU (orange).

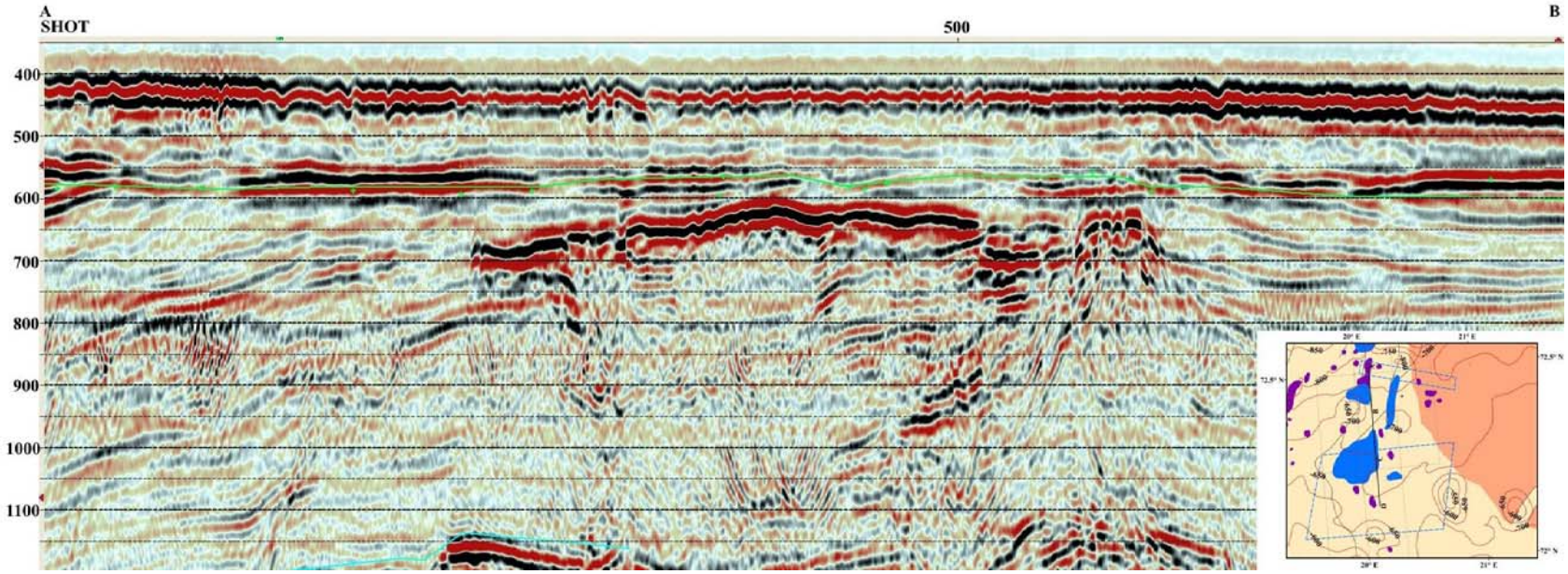

Figure 29. NPD line TR 82-2045_8230 showing a major gas anomaly paralleling the seafloor. The anomaly falls at the BSR depths predicted.

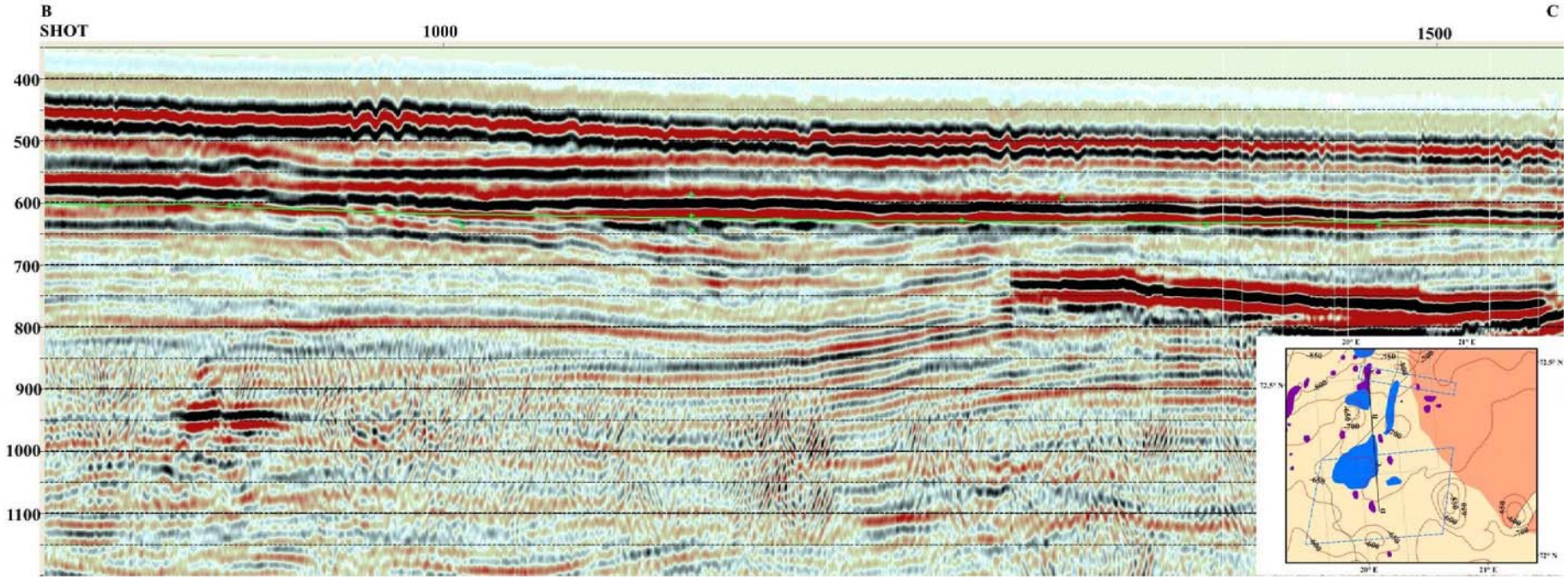

Figure 30. NPD line TR 82-2045_8230 showing a major gas anomaly paralleling the seafloor. The anomaly falls at the BSR depths predicted.

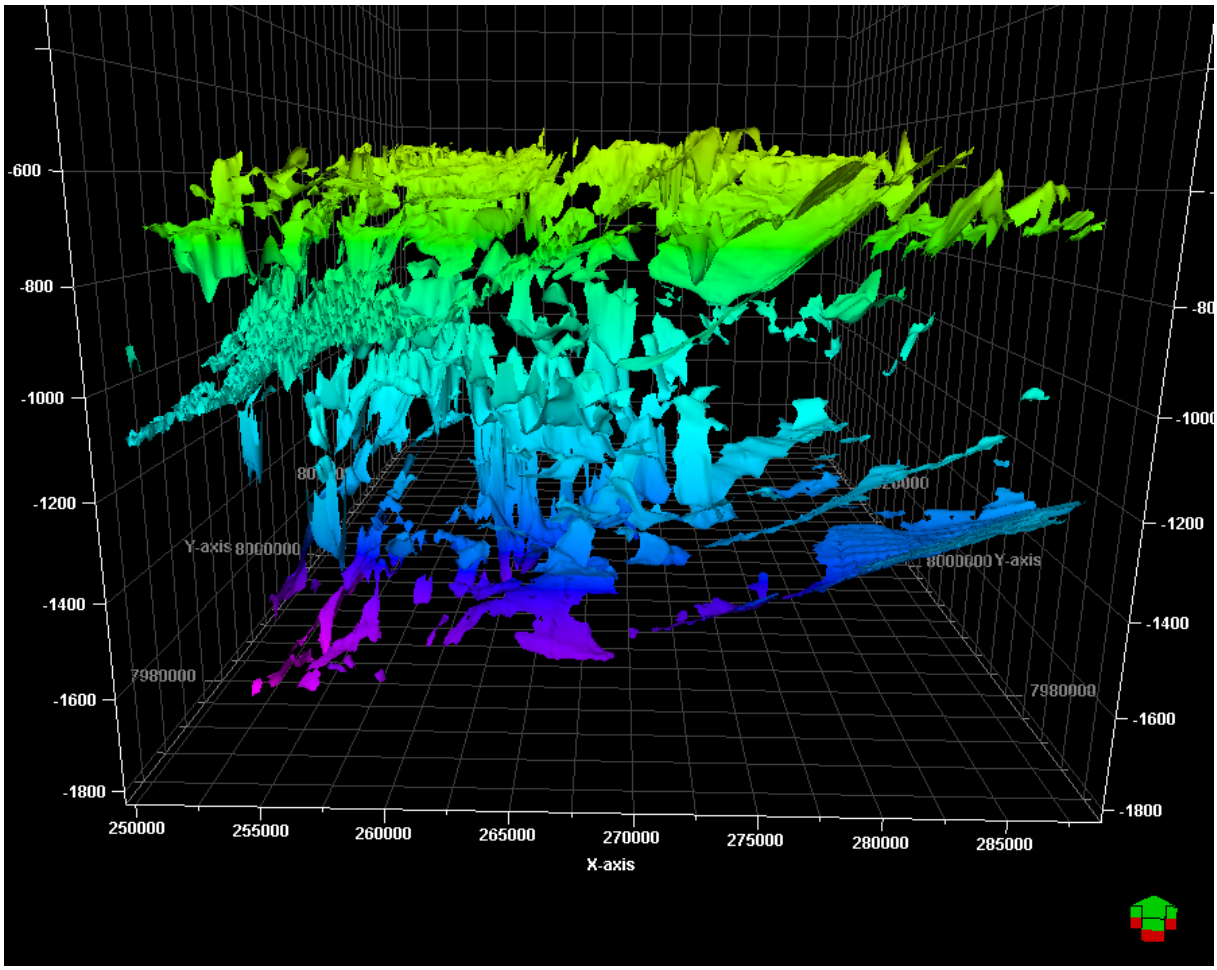

Figure 31. Gas patches interpreted on LHS08M01 3D seismic block at different levels. Notice the connectivity of gas at different levels and focussing at specific sites. These sites are coincident with faults which are occasionally continuous and other times interlinked at different levels. The gas patches interpreted are those above base Tertiary reflector. Selected profiles across the anomalies are shown on figures 32and 33.

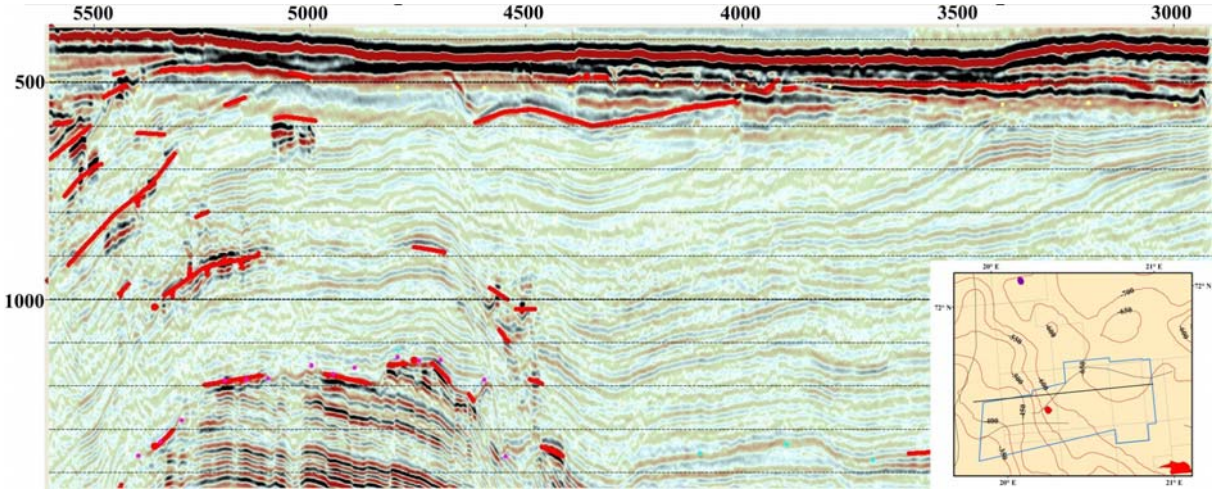

Figure 32. A) Gas anomalies along X line 2567 from full stack 3D seismic area LH08M01.

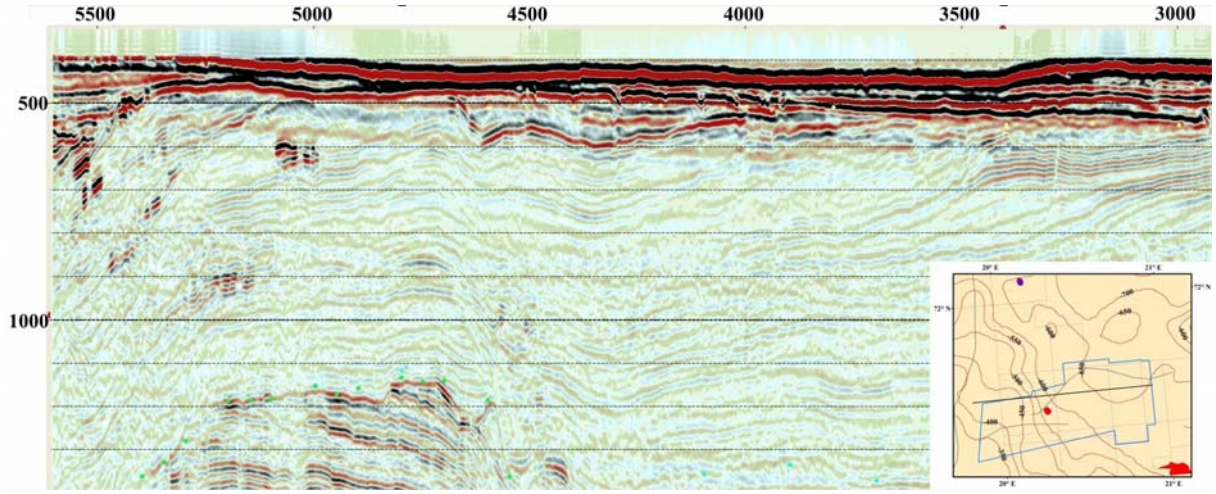

Figure 32. B) Near stack of the X line 2567 along the 3D seismic area LH08M01.

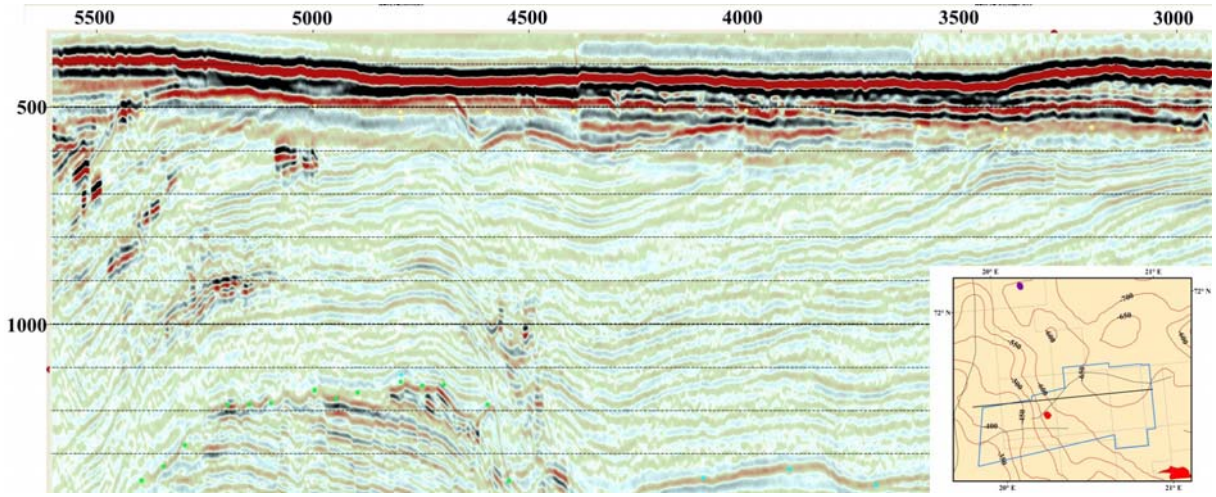

Figure 32. C) Far stack of the X line 2567 along the 3D seismic area LH08M01.

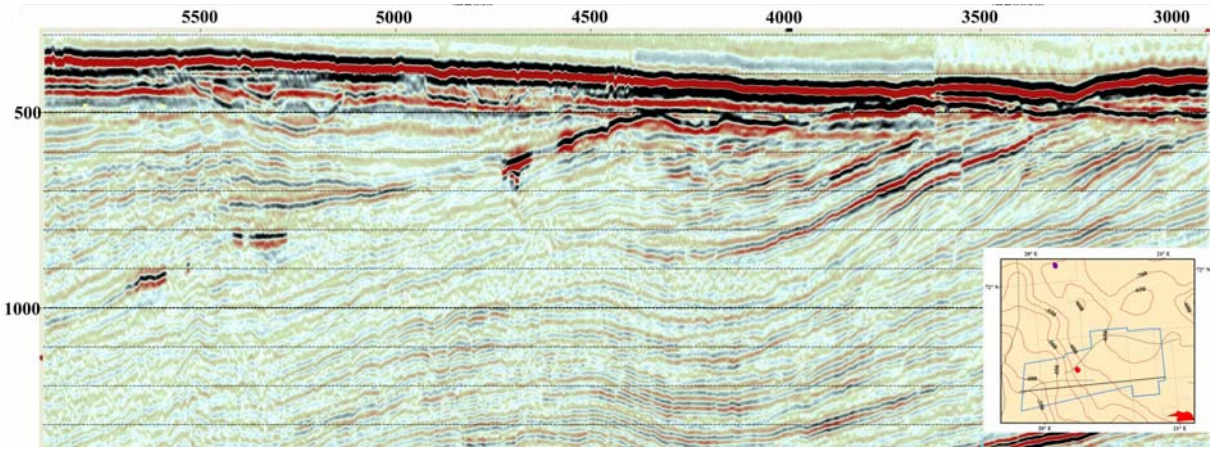

Figure 33. A) Gas Anomalies along X line 1967from full stack 3D seismic area LH08M01.

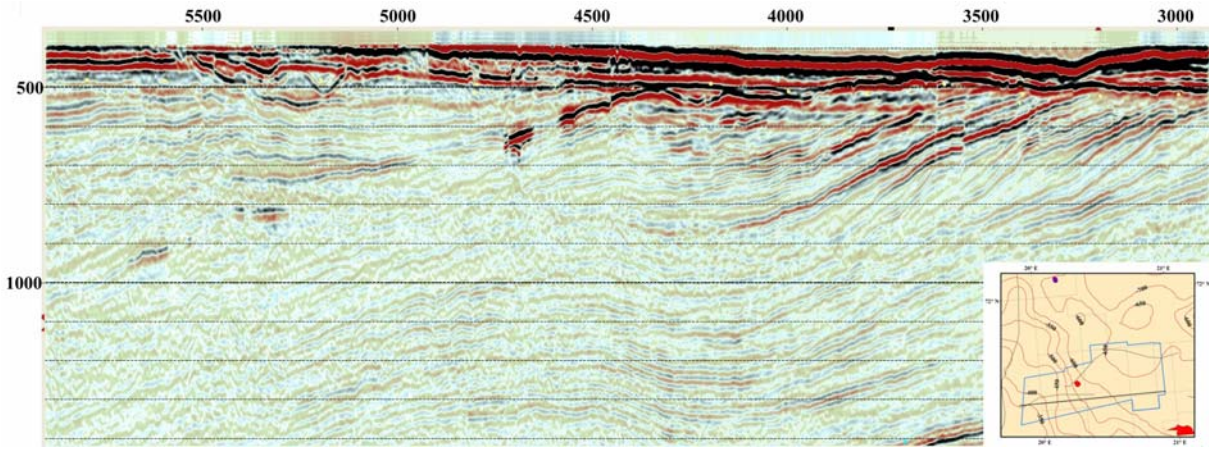

Figure 33. B) Near stack of the X line 1967 from the 3D seismic area LH08M01.

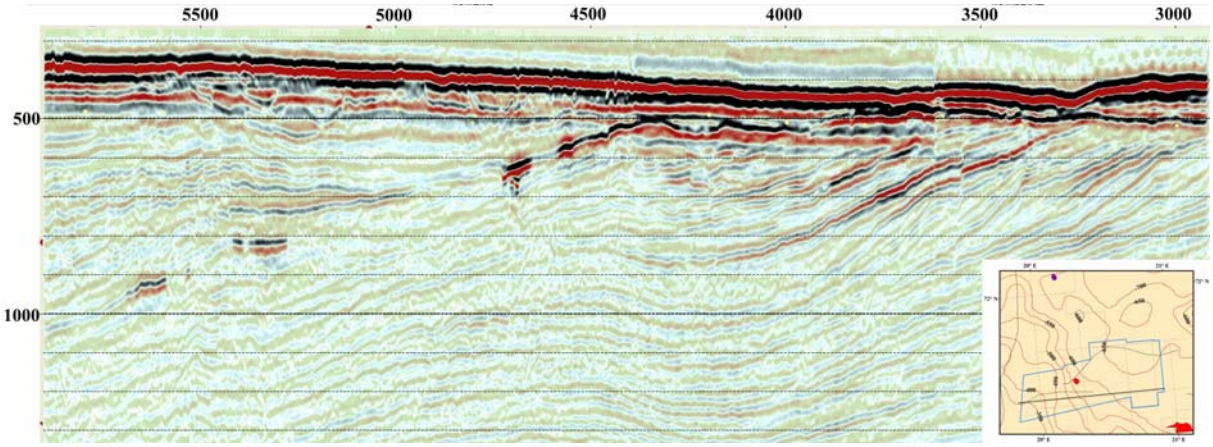

Figure 33. C) Far stack of the X line 1967 from the 3D seismic area LH08M01.

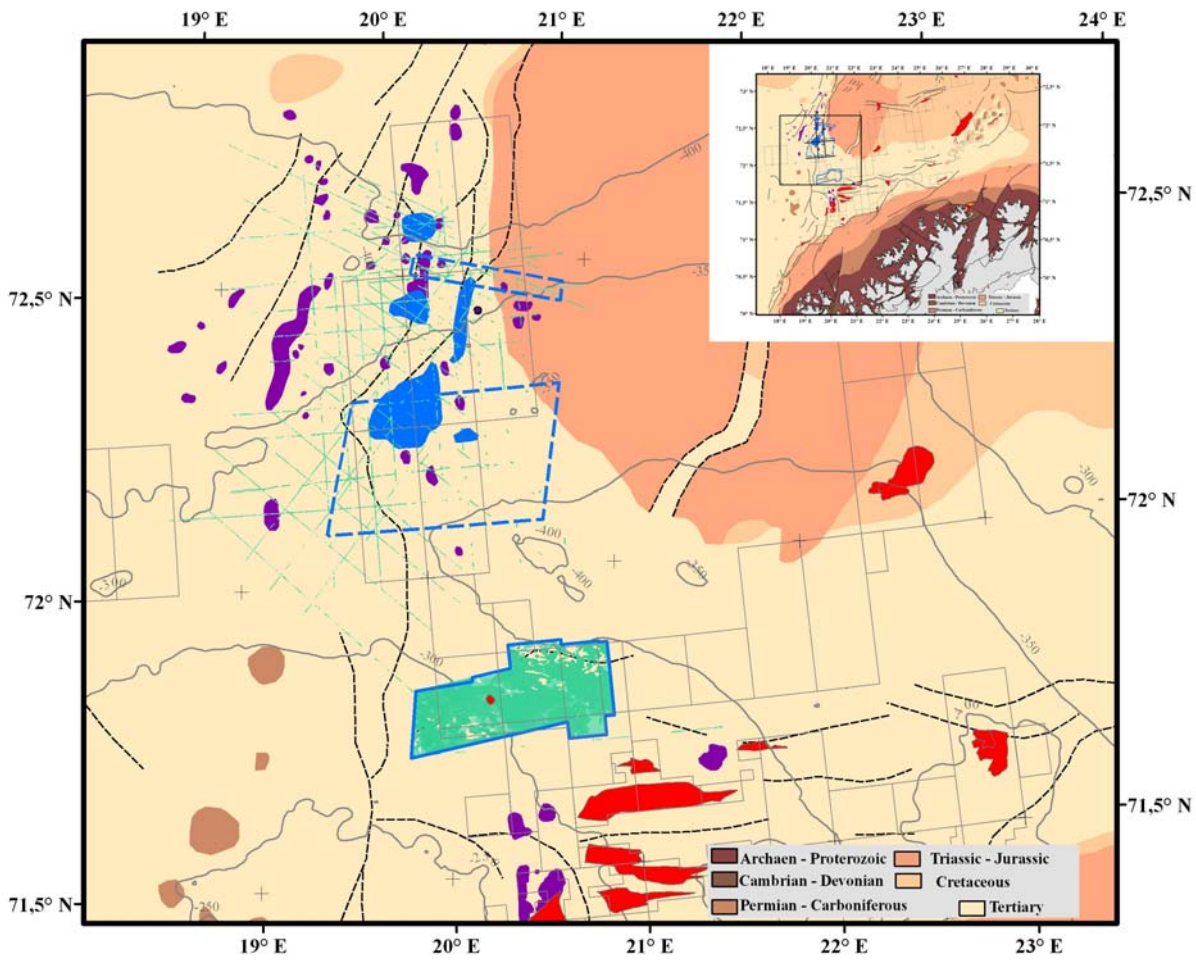

Figure 34. Gas indications (green) in the study area interpreted from 2D and 3D seismic data. The locations of gas (purple) and BSR (blue) interpreted in earlier studies are also shown. The gas occurrences shown are at different depth levels.

4.3 Seismostratigraphy

Most of the Quaternary deposits at the Barents Sea shelf (ie., above URU) comprise stiff to hard tills (Sættem et al., 1992; Vorren et al., 1989). According to Hald et al. (1990) who investigated samples from 13 boreholes, the sediments relate mainly to the last ice age (i.e., <100,000 yrs) probably with most sediments deposited during the late Weichselian (<30,000 yrs). However, Sættem et al (1992) detected Eemian sediments in the Bear Island Fan and suggest that tills below could be up to 400,000 yrs old (Table I). After the last glacial advances in the Barents Sea, a glacial marine depositional environment with numerous icebergs drifting around prevailed to c. 10 ka BP. Shortly after the ice sheet receded from the shelf, large icebergs made numerous furrows into the glacial seafloor. The most intense iceberg ploughing occured on the banks, while glaciomarine sediments (silty clay with ice rafted clasts) were deposited in the troughs. In Ingøydjupet, these sediments are acoustically fairly transparent and up to 200 ms TWT thick and are inferred to be deposited under fairly low effective ice load without significant erosion (Rise et al., 1993). The upper 5-20m thick unit is acoustically laminated comprising soft fine grained sediments. IKU boreholes 7222/09-U-01 and 7220/02-U-01 indicated an average seismic sound velocity of 1788 m/s of the 101.5 m thick Quaternary cover east of the study area. Borehole 7220/02-U-01 close to our study area penetrated only about 14 m into an about 70 m thick Quaternary succession, and velocities measured were up to 1990 m/s. High degree of compaction at about 14 m suggests an overall high seismic velocity at this site (Rise et al., 1993). Our study area is located along the northernmost part of the borehole and close to a morainal high, and is thus affected by ice load to a certain extent.

Seismo-stratigraphic interpretations along the southwestern Barents Sea indicated four major intra Quaternary units along the study area (Lebesbye, 2000) (Figs. 35-38). The thickness is maximum for the most recent glacial unit 4W in our study area (Figs. 35-38). A regional geological profile across the western Barents Sea show their juxtaposition in relation to various other underlying units as well as units extending eastward (Fig. 39). The general glaciation model for the southwestern Barents Sea based on seismo-stratigraphic interpretations and datings is shown in Fig. 40 (Lebesbye, 2000). The model proposed by Lebesbye (2000) (Fig. 41) based on compilation of all interpretations indicate the following sequence of events: A) Ice margins covering Ingøydjupet during GA2 and 3 and the related deposition of unit E2, B) Ice margins up to the present Barents shelf edge during GA5 and the related deposition of units E3 and E4 and with following phases; 1: The initial advance outside the coast, 2: a phase during the advance when much sedimentation took place in Ingøydjupet and at its periphery, 3: LGM1 (23 ^{14}C ka BP) marks the terminal position of the ice sheet at the shelf edge, C) Ice margins again reaching Barents shelf edge during GA6-9 and the sedimentation units E5 and E6 (Lebesbye, 2000) with following phases, 1: Approximate ice position when large parts of unit E5 and parts of E6 were deposited, 2: ice

maximum position (LGM II (18 ^{14}C ka BP)), partly along the shelf edge, D) Ice margin position during the last deglaciation; 1: ice margin during deposition of most of the unit E7, 2: the Risvik substage (Lebesbye, 2000).

Shallow and deep stratigraphy below base Cretaceous was interpreted based on the tie from 3D seismic PL438 along the X-line 833 supplied by Lundin. The available 2D industry seismic data was used to extend the interpretation throughout the study area. Three major horizons were interpreted which include base Cretaceous (Fig. 42), base Tertiary (Fig. 43) and base Quaternary/URU (Fig. 44). Using high resolution 2D seismic and TOPAS data collected by FFI, intra Quaternary reflectors were also identified (45-48). The study area falls at the western edge of the Loppa High, at the westernmost boundary of the postglacial depositional system (Fig. 39). Three Quaternary units described by Lebesbye (2000) (Fig. 35-38) were identified; 4W (uppermost), 2W and 1W (lowermost). We used the TOPAS data to establish a high resolution stratigraphy within the top few tens of milliseconds (Fig. 49 & 50). The TOPAS profiles indicated two reflectors (4W1 & 4W2) within the shallow part of the 4W succession in the southern basinal part of the MBB area.

We propose that probably the stage B and C described above for the E units from the east of Loppa High coincides with the deposition of intra 4W units, namely 4W2 and 4W1, during LGM1 and LGM II respectively when the glaciers were close to the present shelf edge. Laberg and Vorren, (1996) correlated unit 1W, 2W and 3W to units III (486-430 ka), V (313-258ka) and VI (194-128) respectively (Table 1). This is comparatively older than the boundary R1 (200-400 ka) (which also is base of 1W) proposed by Butt et al. (2000) and Solheim et al. (1998) and generally accepted for this region (Andreassen et al., 2005; Knies et al., 2009). A brief correlation of various stratigraphic compilations are given in Table 2. The study indicates that the thickest glacial unit 4W was probably deposited during the last two glaciations covering a period of about 28 kyrs and correlate with the deposition of E3, E4, E5, E6 and E7 units. The units 3W, 2W and 1W were deposited contemporaneous with E2 with oldest age of 200 kyrs for base of unit 1W or boundary R1. We do not have unit corresponding to E1 in our study area but probably they are contemporaneous with units I to II and between URU and R1.

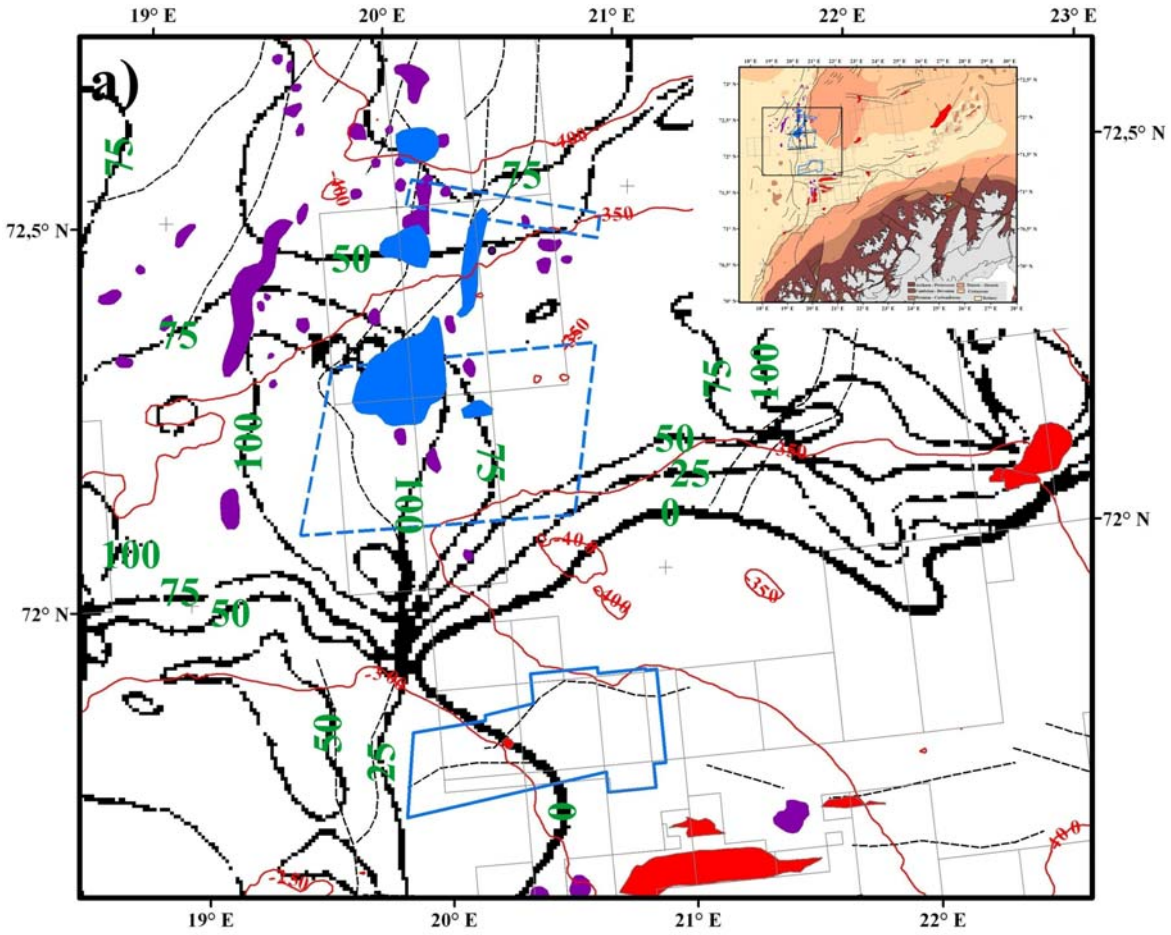

Figure 35. Contour map of Unit 4W (black; Lebesbye, 2000) overlaid on the bathymetry contour (red) map of the Barents Sea. Also shown are the locations of MBB and 3D seismic datasets, gas anomalies (purple), BSR (blue), oil discoveries (red) and faults (dashed lines).

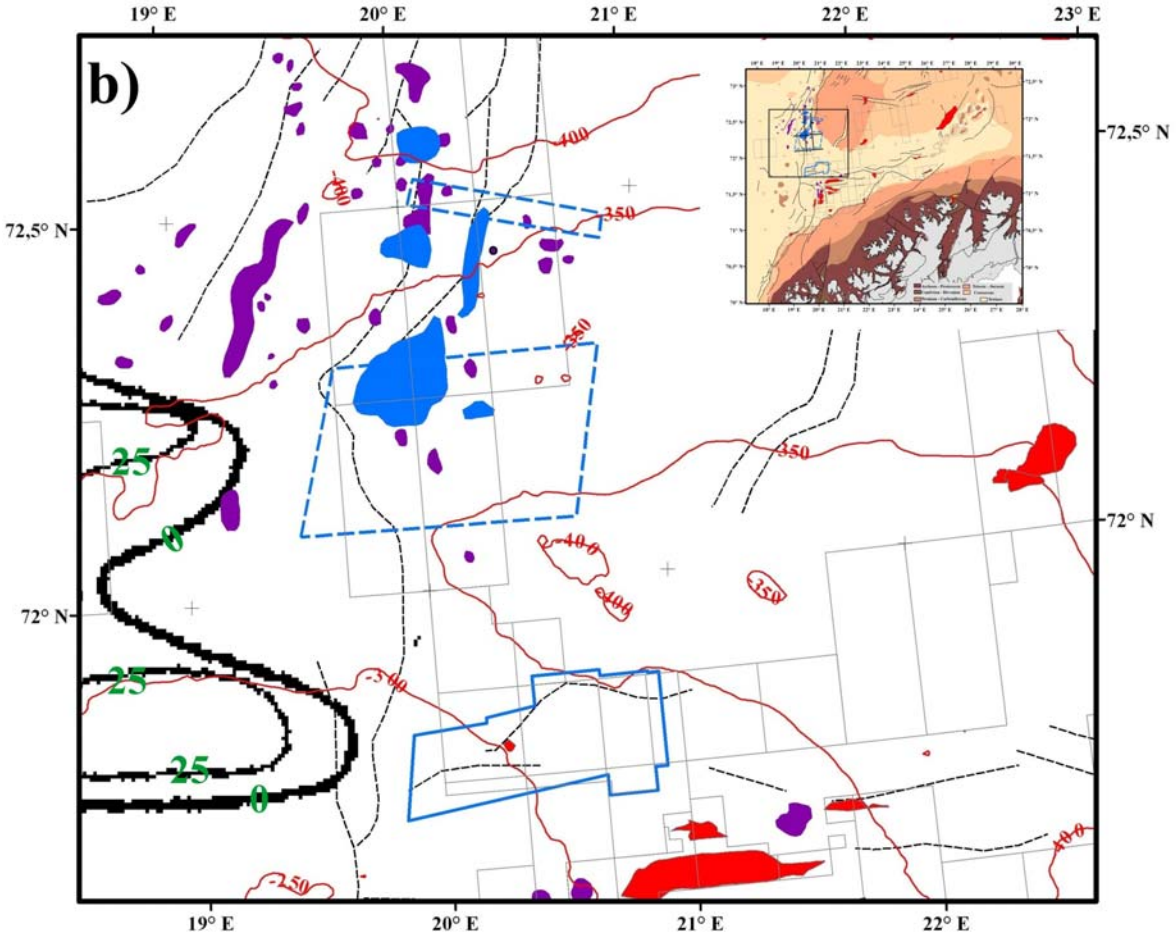

Figure 36. Contour map of Unit 3W (black; Lebesbye, 2000) overlaid on the bathymetry contour (red) map of the Barents Sea. Also shown are the locations of MBB and 3D seismic datasets, gas anomalies (purple), BSR (blue), oil discoveries (red) and faults (dashed lines).

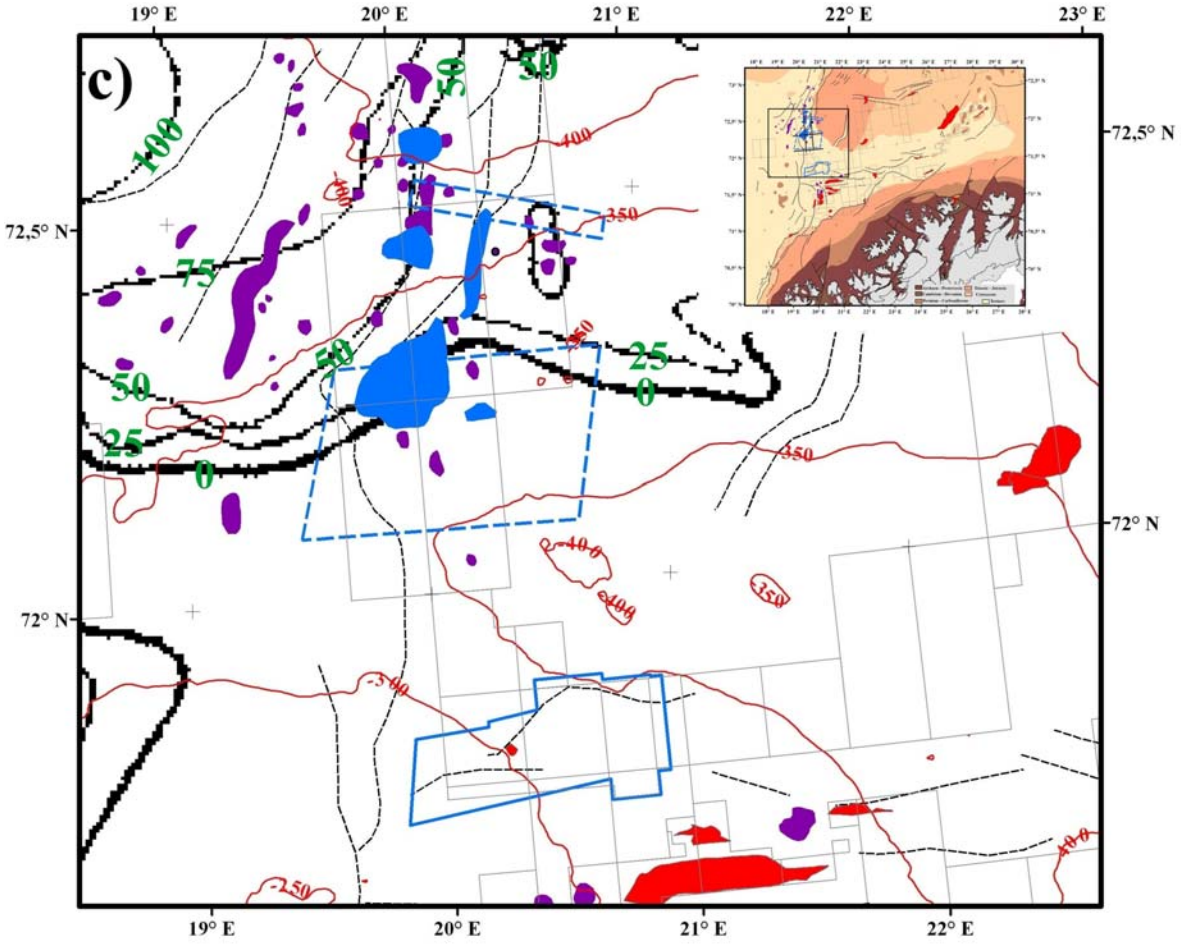

Figure 37. Contour map of Unit 2W (black; Lebesbye, 2000) overlaid on the bathymetry contour (red) map of the Barents Sea. Also shown are the locations of MBB and 3D seismic datasets, gas anomalies (purple), BSR (blue), oil discoveries (red) and faults (dashed lines).

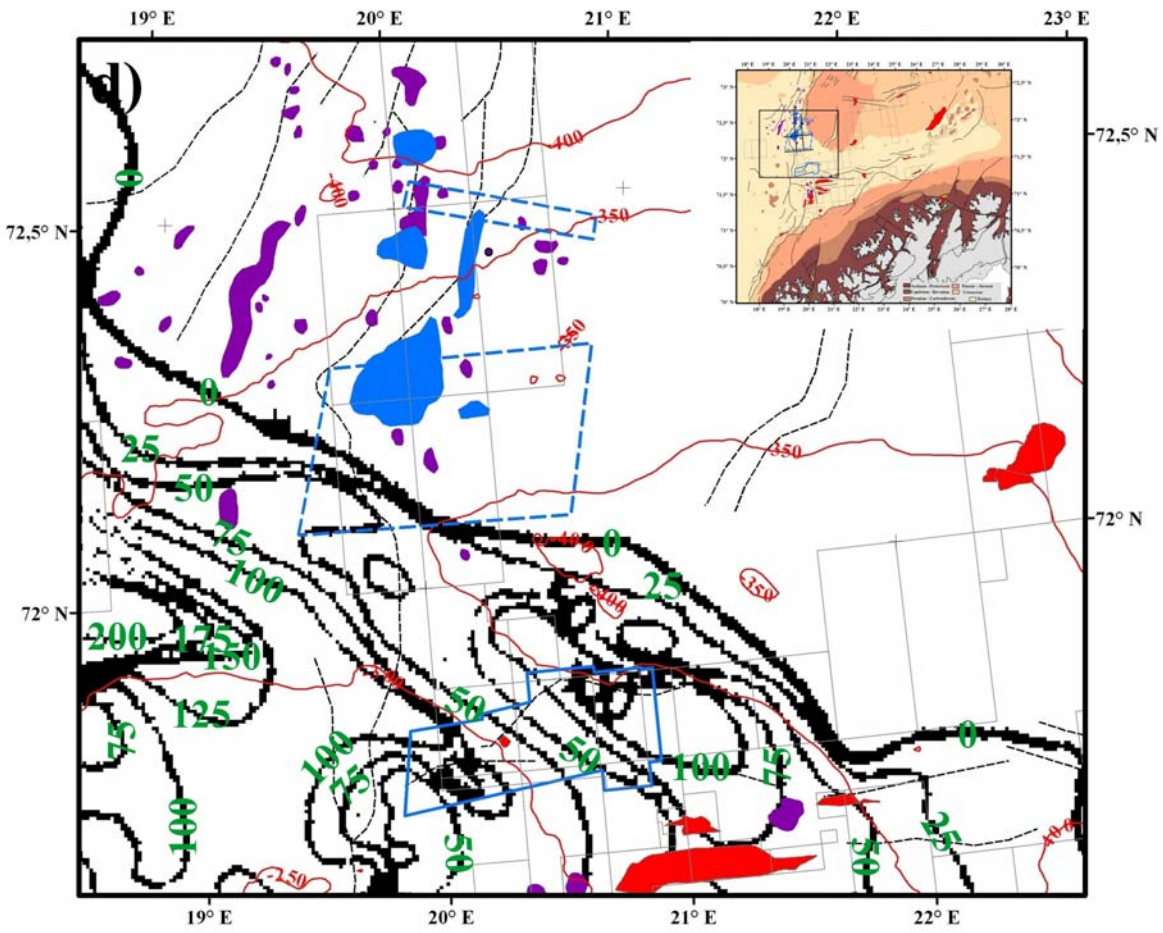

Figure 38. Contour map of Unit1W (black; Lebesbye, 2000) overlaid on the bathymetry contour (red) map of the Barents Sea. Also shown are the locations of MBB and 3D seismic datasets, gas anomalies (purple), BSR (blue), oil discoveries (red) and faults (dashed lines).

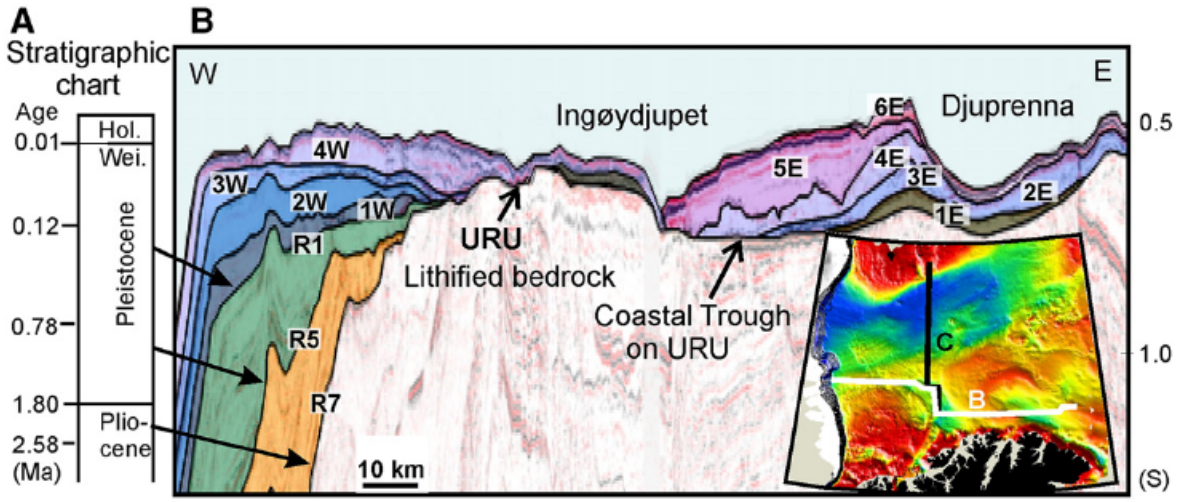

Figure 39. Geological cross section across the western Barents sea showing various units from the Quaternary (Andreassen et al., 2008). Notice that our study area is west of Ingøydjupet partially covering various units marked as 1W to 4W north of this line.

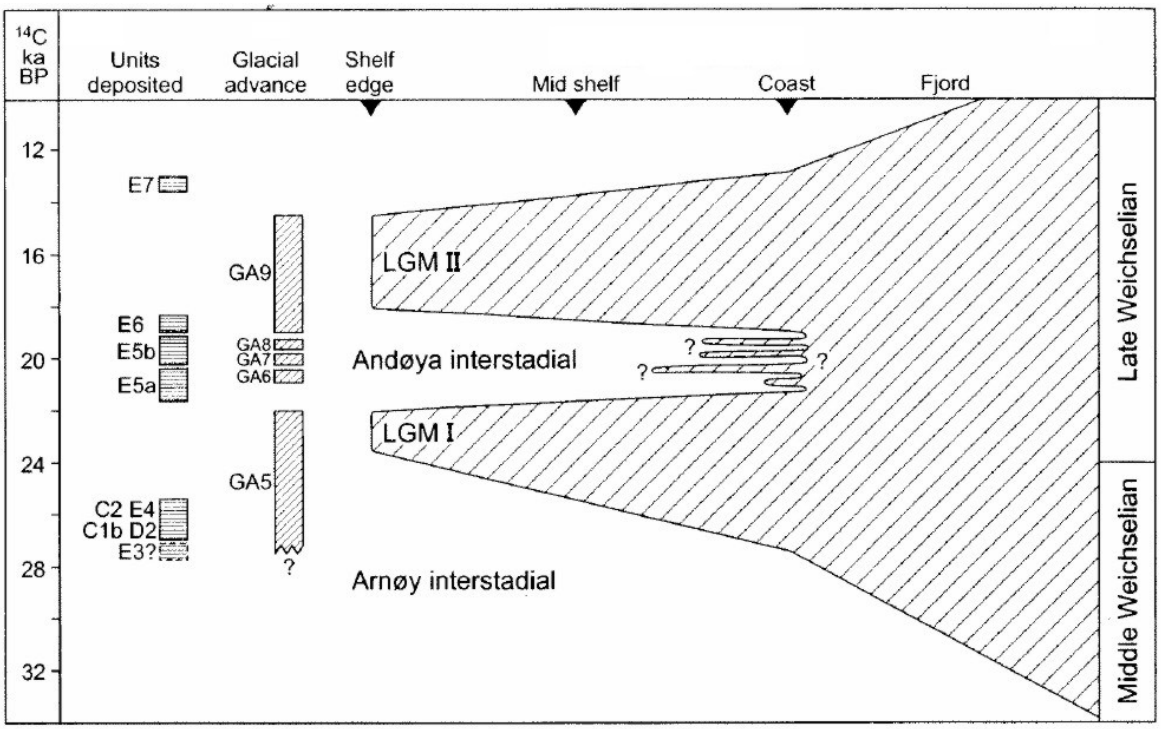

Figure 40. Glaciation curve for the Mid/Late Weichselian ice expansion in the southwestern Barents Sea. Approximate timing of glacial advances (GA5-9) and deposition of sismostratigraphic units is also indicated (Lebesbye, 2000).

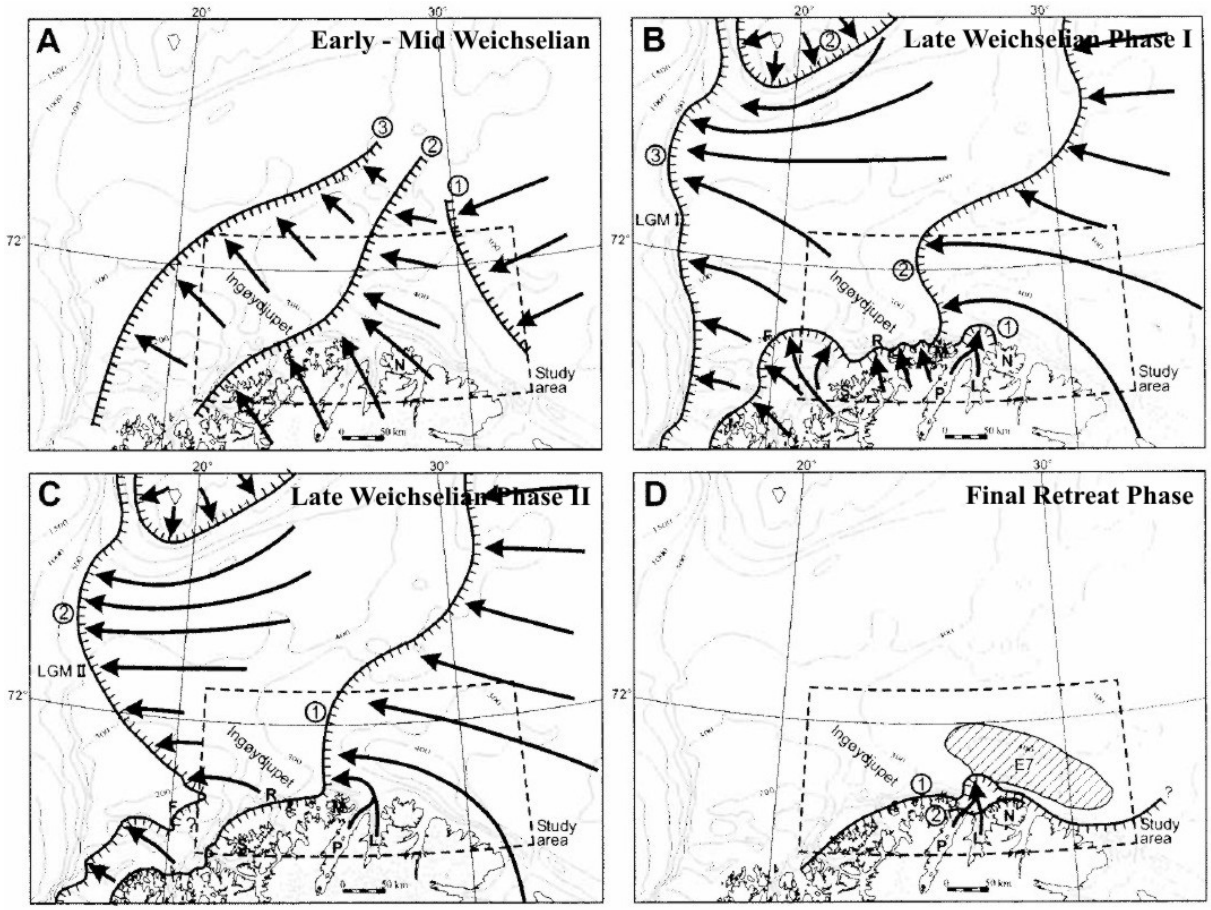

Figure 41. Reconstructed ice marginal positions and ice flow directions in the southwestern Barents Sea based on seismo-stratigraphic interpretations (Lebesbye, 2000). A) Ice margins during GA2 and 3, and the related deposition of unit E2, B) Ice margins during GA5 and the related deposition of E3, E4 and 4W2 (this study); 1: The initial advance outside the coast, 2: a phase during the advance when much sedimentation took place in Ingøydjupet and at its periphery, 3: LGM1 (23 ^{14}C ka BP) marks the terminal position of the ice sheet at the shelf edge, C) Ice margins during GA6-9 and the sedimentation units E5, E6 (Lebesbye, 2000), and 4W1(this study) 1: Approximate ice position when large parts of unit E5 and parts of E6 were deposited, 2: ice maximum position (LGM II (18^{14}C ka BP)), partly along the shelf edge, D) Ice margin position during the last deglaciation; 1: ice margin during deposition of most of the unit E7, 2: the Risvik substage.

Table 1. Correlation of various units observed in the Barents Sea. Compiled by Laberg and Vorren (1996).

Vorren et al. (1990)	Sættem et al. (1992)		Laberg & Vorren, 1996	Isotope stage (Williams et al. 1988)	Age (ka)
	Units	Age (ka)			
4W	G		VIII	2	
< 28 ka [a]	F	< 30	VII	2	24–12
	E	130–?			
3W	D_2	< 200–130	VI	6	194–128
2W	D_1	< 330	V	8	313–258
	C		IV	10	386–359
1W		< 440	III	12	486–430
	B		II	14	544–521
< 800 ka [b]		< 730 [c]	I	16	622–589

[a] = AMS radiocarbon-date (Vorren et al., 1990), [b] = age tentatively suggested by Vorren et al. (1991) and [c] = dating result based on magnetopolarity, the other results of Sættem et al. (1992) are based on aminostratigraphy.

Table 2. Correlation of various units from western the Barents Sea based on compilation of information from various studies (Lebesbye 2000; Butt et al. 2000; Solheim et al. 1998; Sættem et al. 1992) and to those from this study.

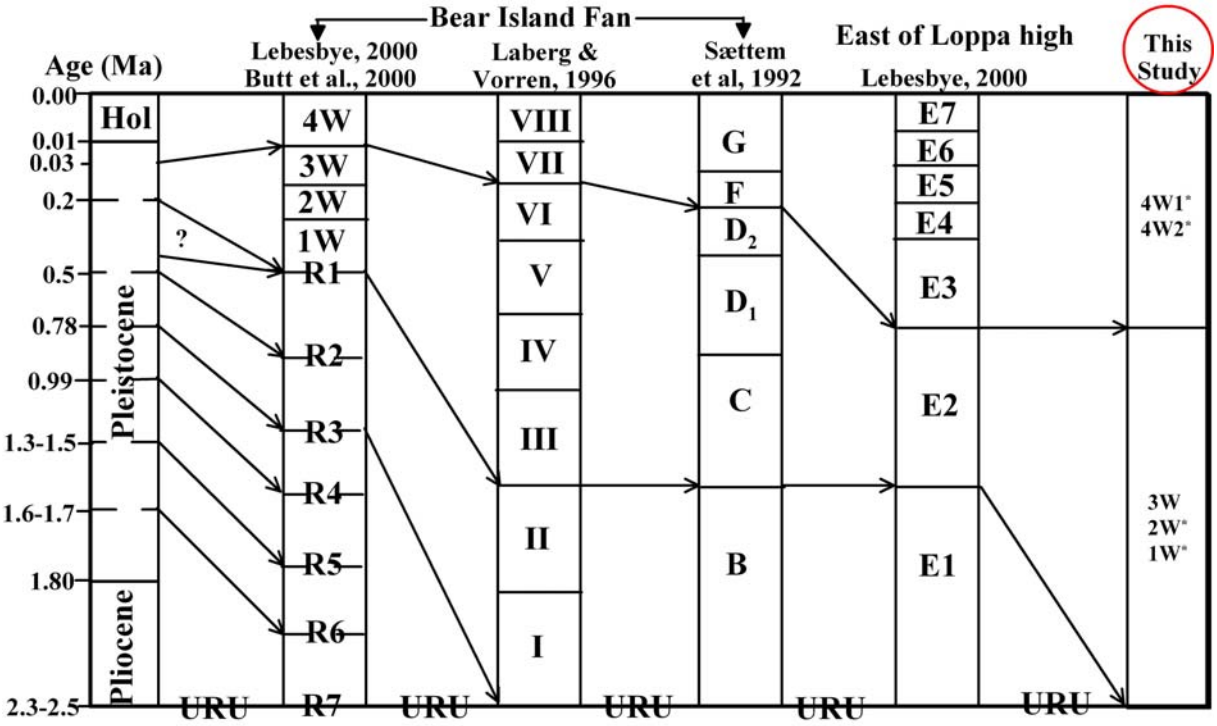

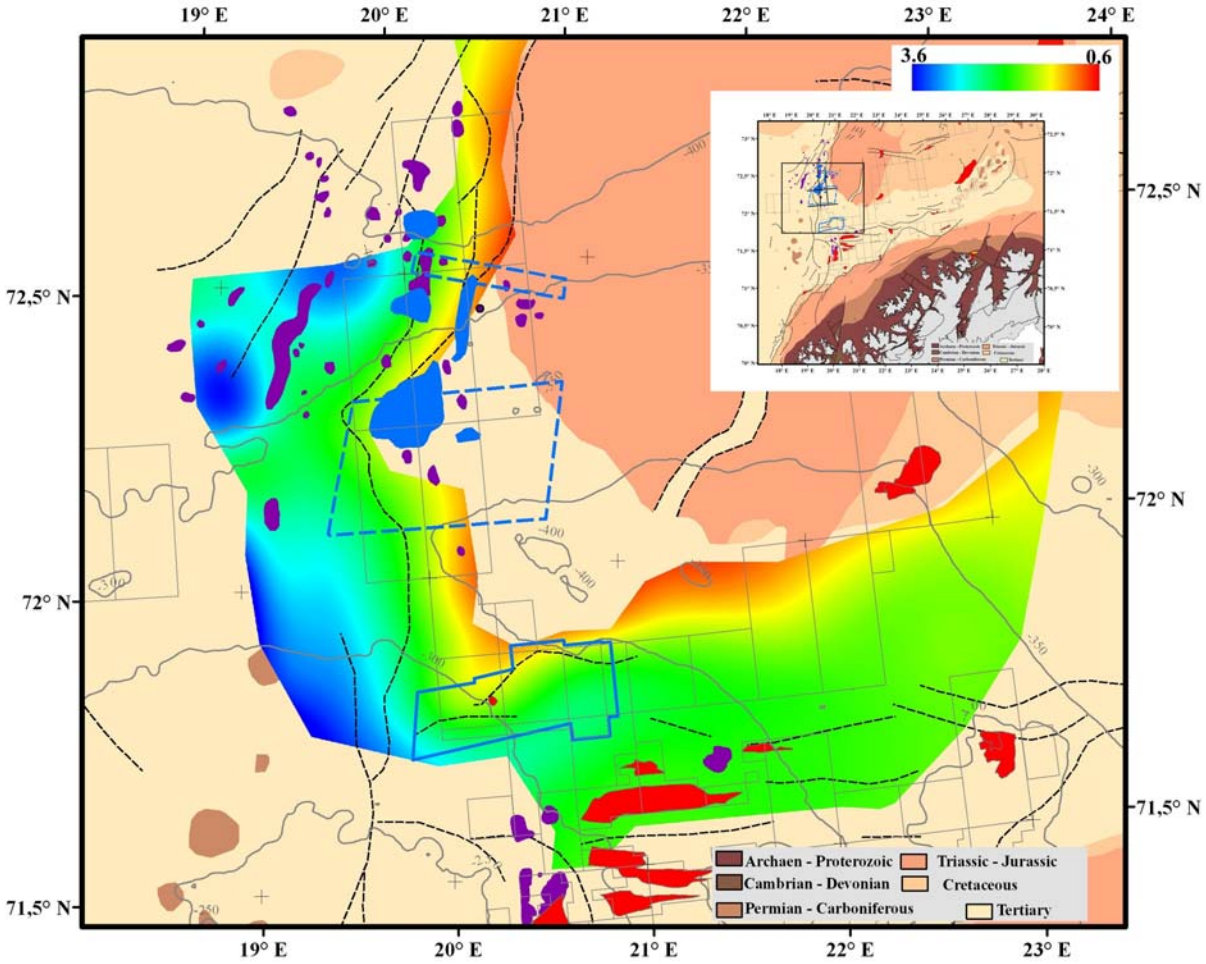

Figure 42. Base Cretaceous TWT (sec) map overlaid on structural and bedrock map of the Barents Sea. Also shown are locations of the MBB and 3D seismic datasets (blue), oil discoveries(red), gas indications (purple), BSR (blue) and regional bathymetry of the study area (contours).

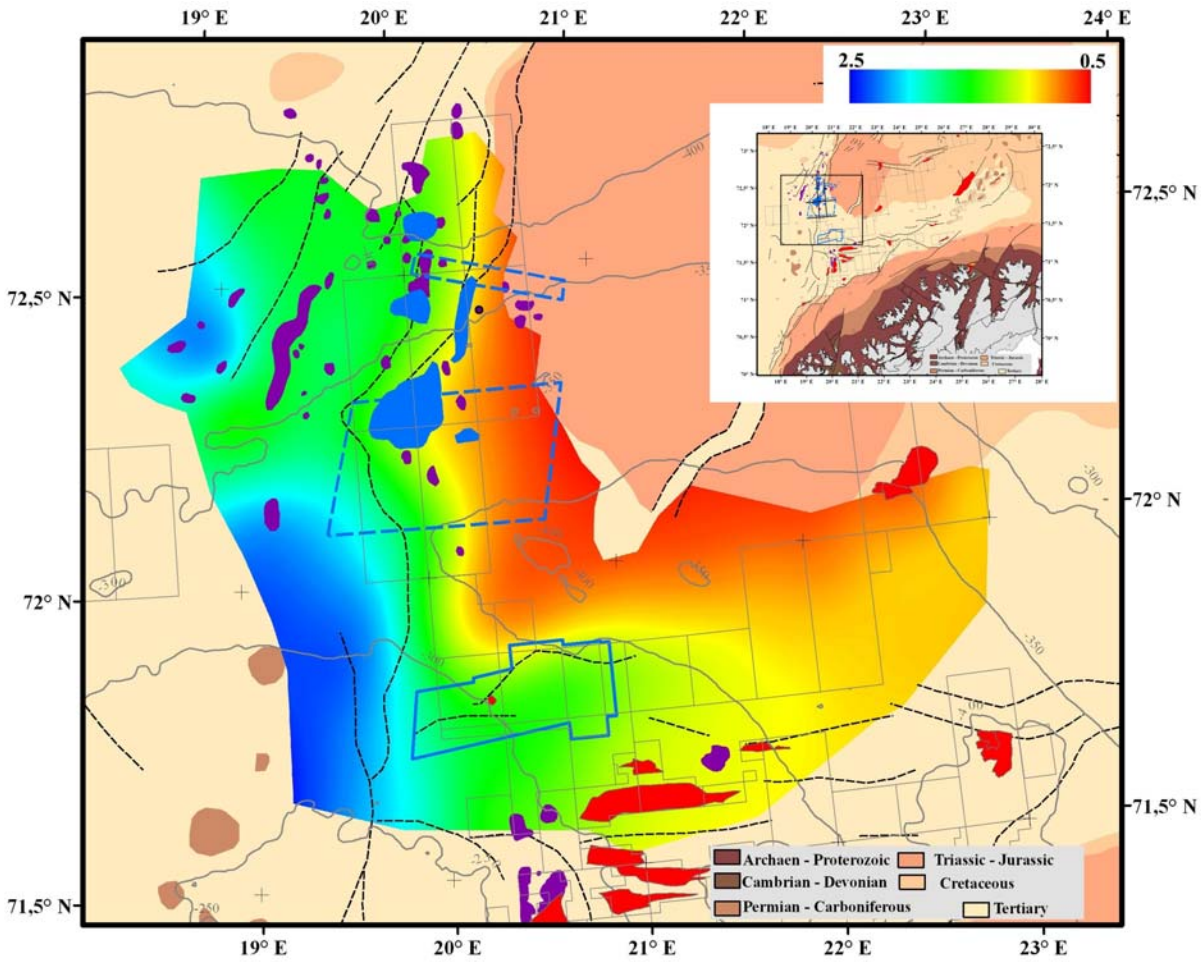

Figure 43. Base Tertiary TWT (sec) map overlaid on structural and bedrock map of the Barents Sea. Also shown are locations of the MBB and 3D seismic datasets (blue), oil discoveries(red), gas indications (purple), BSR (blue) and regional bathymetry of the study area (contours).

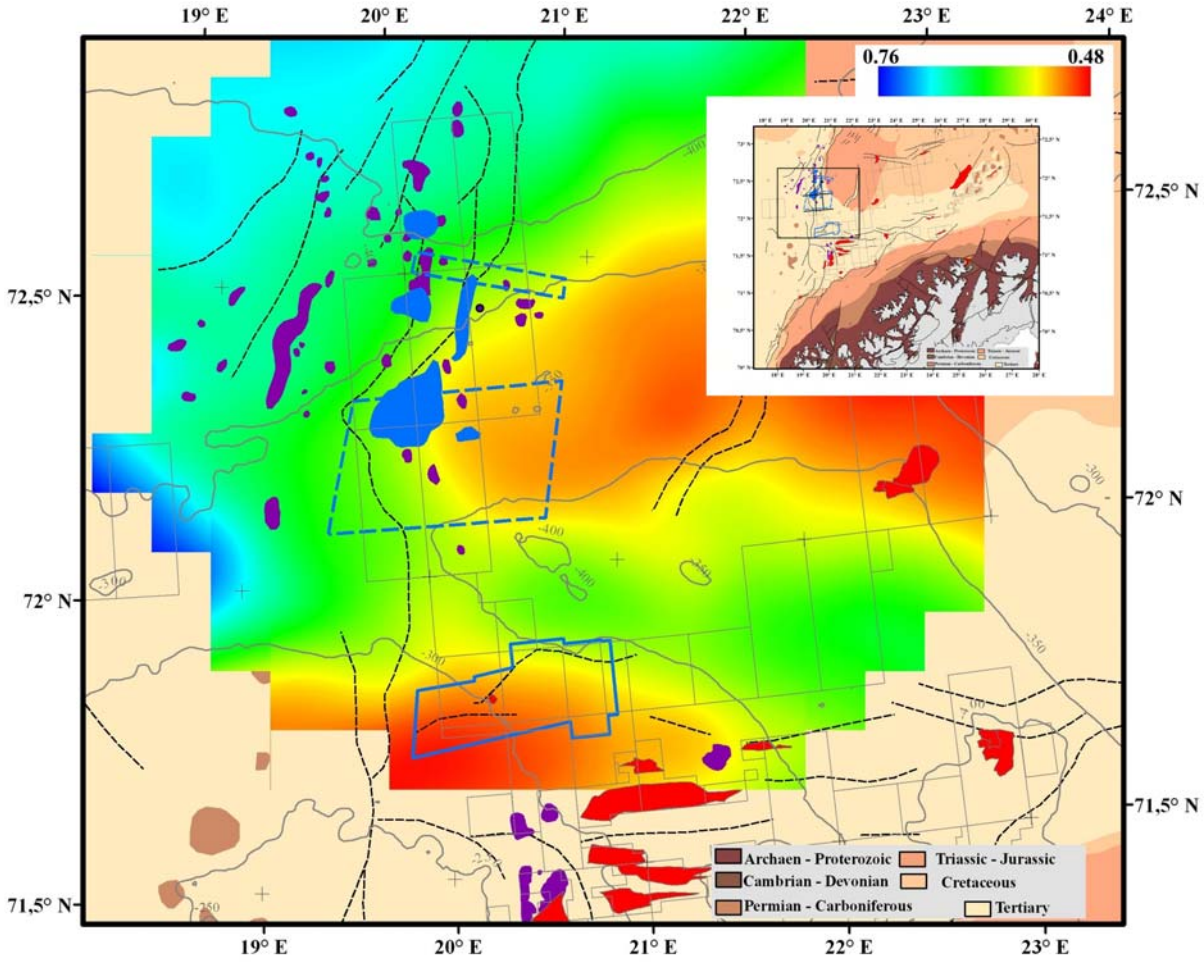

Figure 44. Base Quaternary/URU TWT (sec) map overlaid on structural and bedrock map of the Barents Sea. Also shown are locations of the MBB and 3D seismic datasets (blue), oil discoveries(red), gas indications (purple), BSR (blue) and regional bathymetry of the study area (contours).

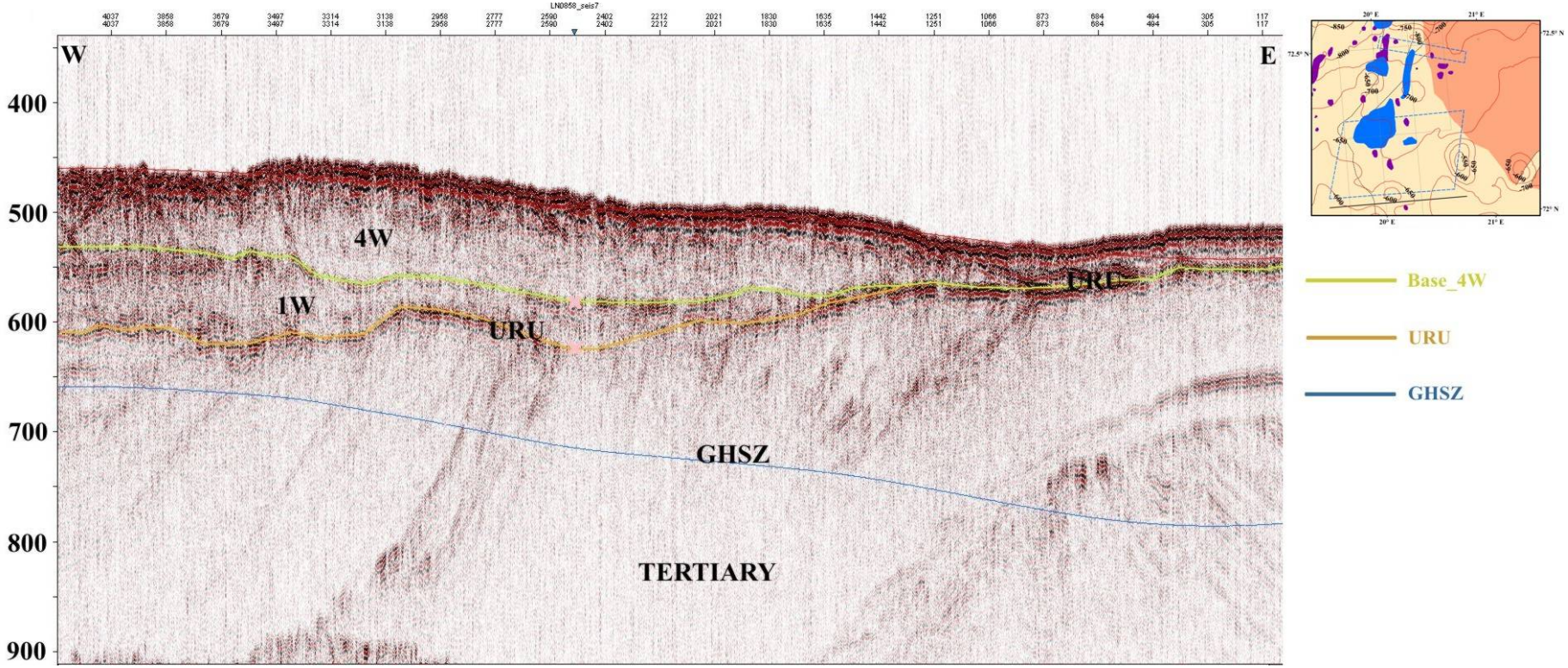

Figure 45. FFIAG_1 2D seismic line (see Fig. 24 for location) in W-E direction indicating gas anomalies below the URU (orange).

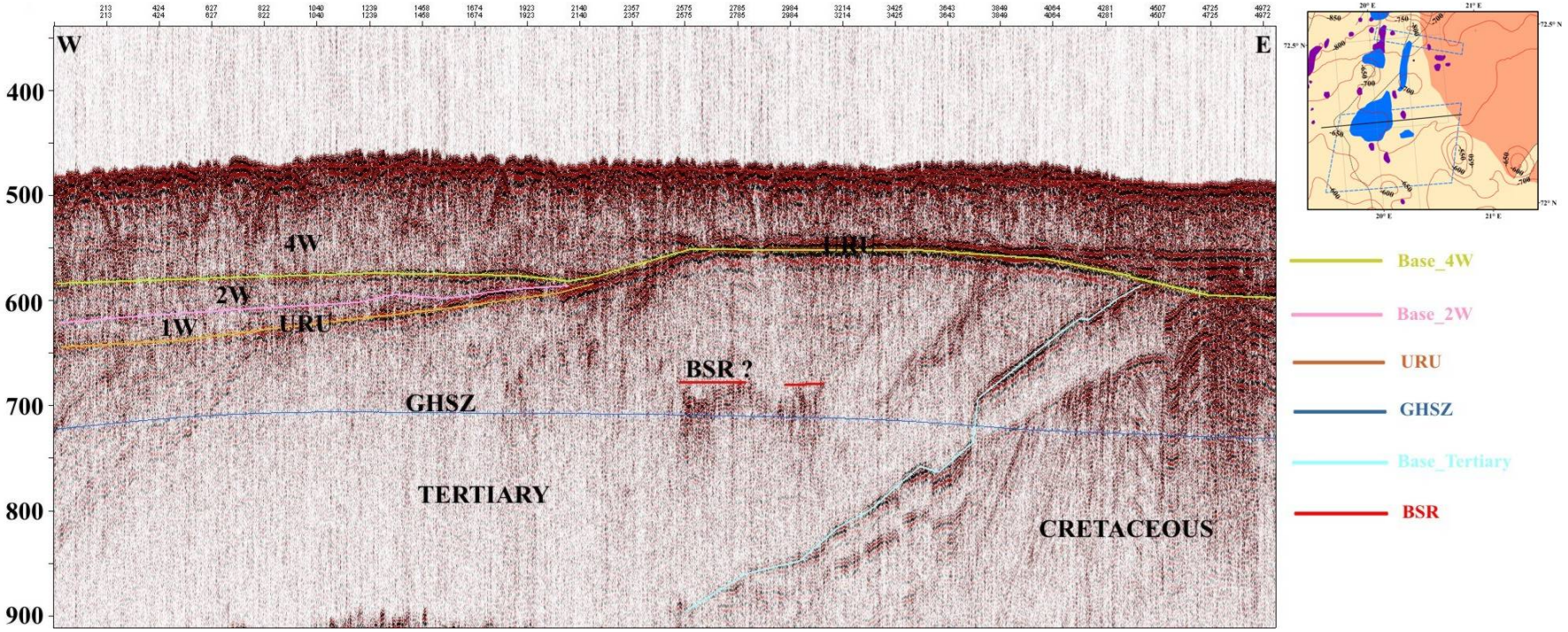

Figure 46. FFIAG_6 2D seismic line (see Fig. 24 for location) in W-E direction indicating gas anomalies below the URU (orange).

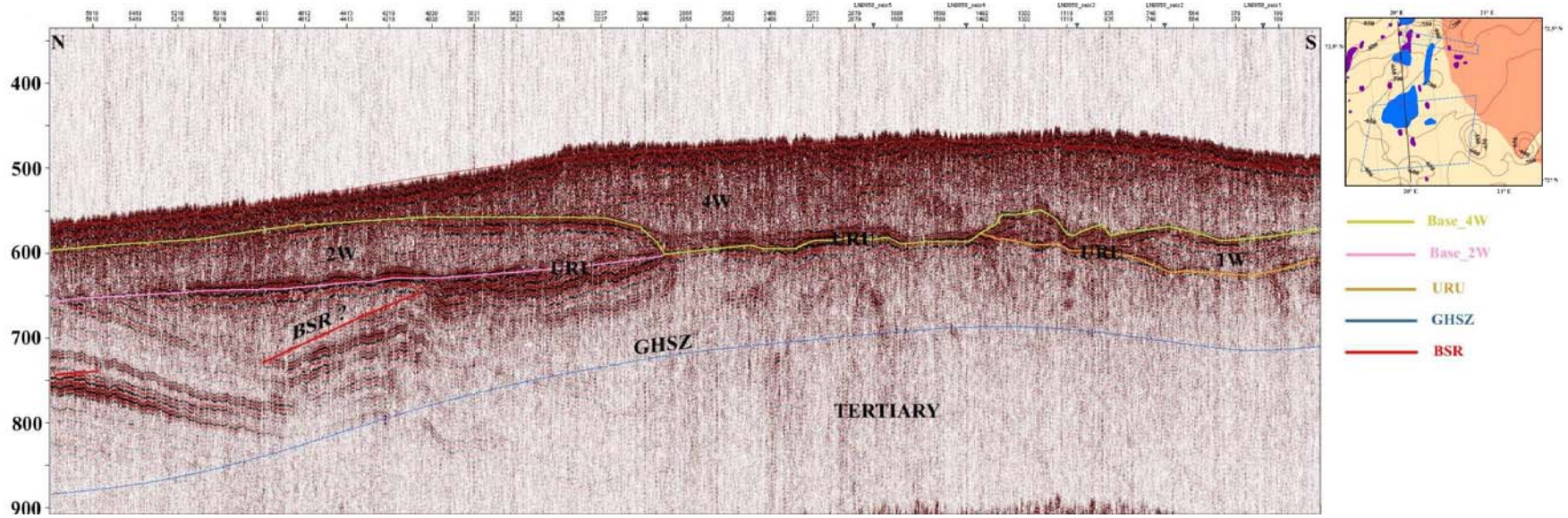

Figure 47. FFIAG_7 2D seismic line (see Fig. 24 for location) in N-S direction indicating gas anomalies below the URU (orange).

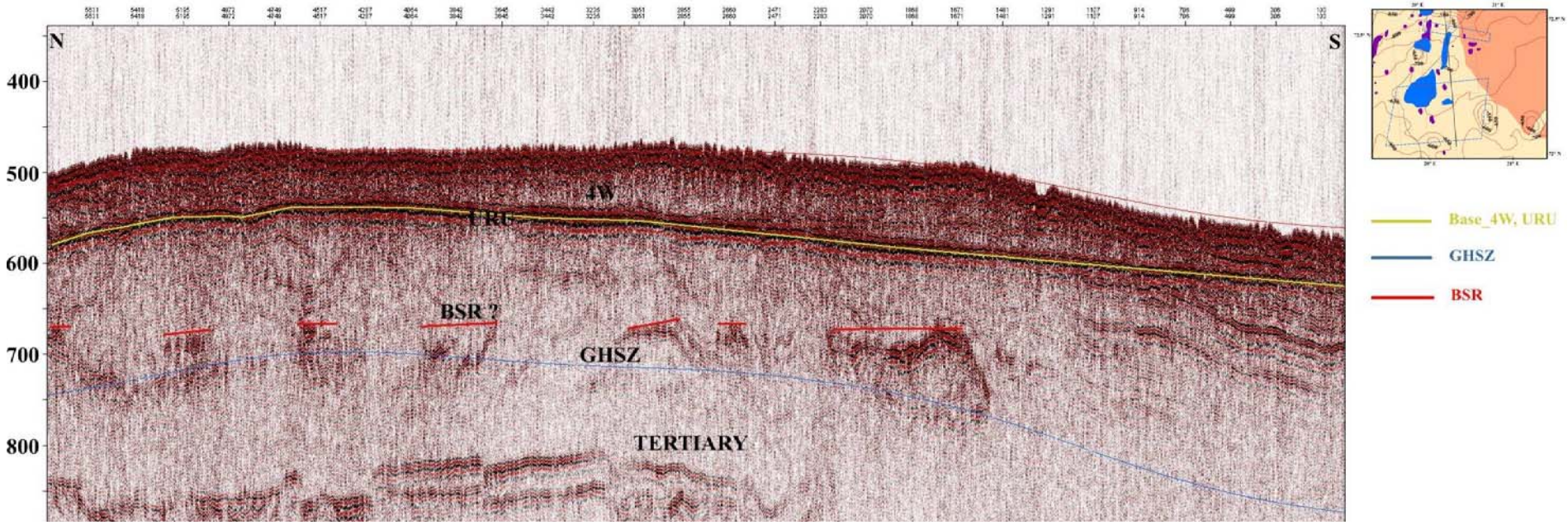

Figure 48. FFIAG_8 2D seismic line (see Fig. 24 for location) in N-S direction indicating gas anomalies below the URU (orange).

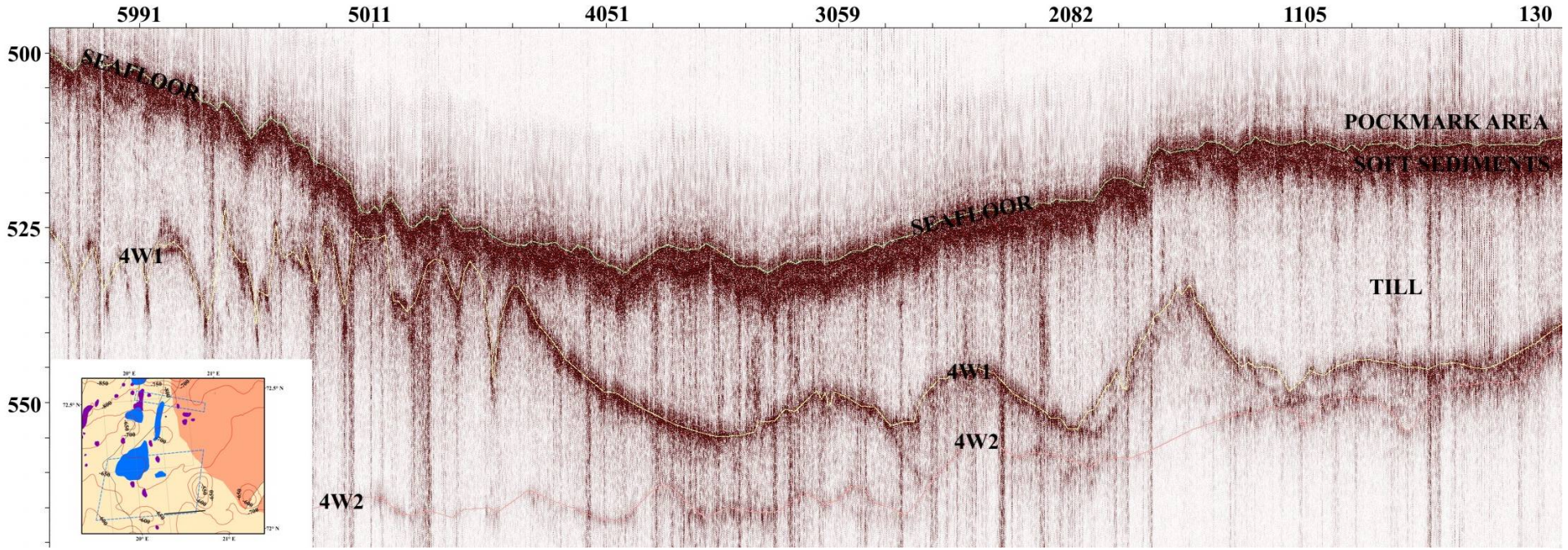

Figure 49. FFI TOPAS line 101085 in W-E direction indicating intra 4w reflections 4W1 and 4W2 within the unit 4W. The southern pockmark area is underlain by a thin layer of soft sediments overlying glacial till from the last glaciation (4W1) is also indicated. Another intra 4W unit can be identified (4W2) which indicate deposition from a previous intra glacial cycle.

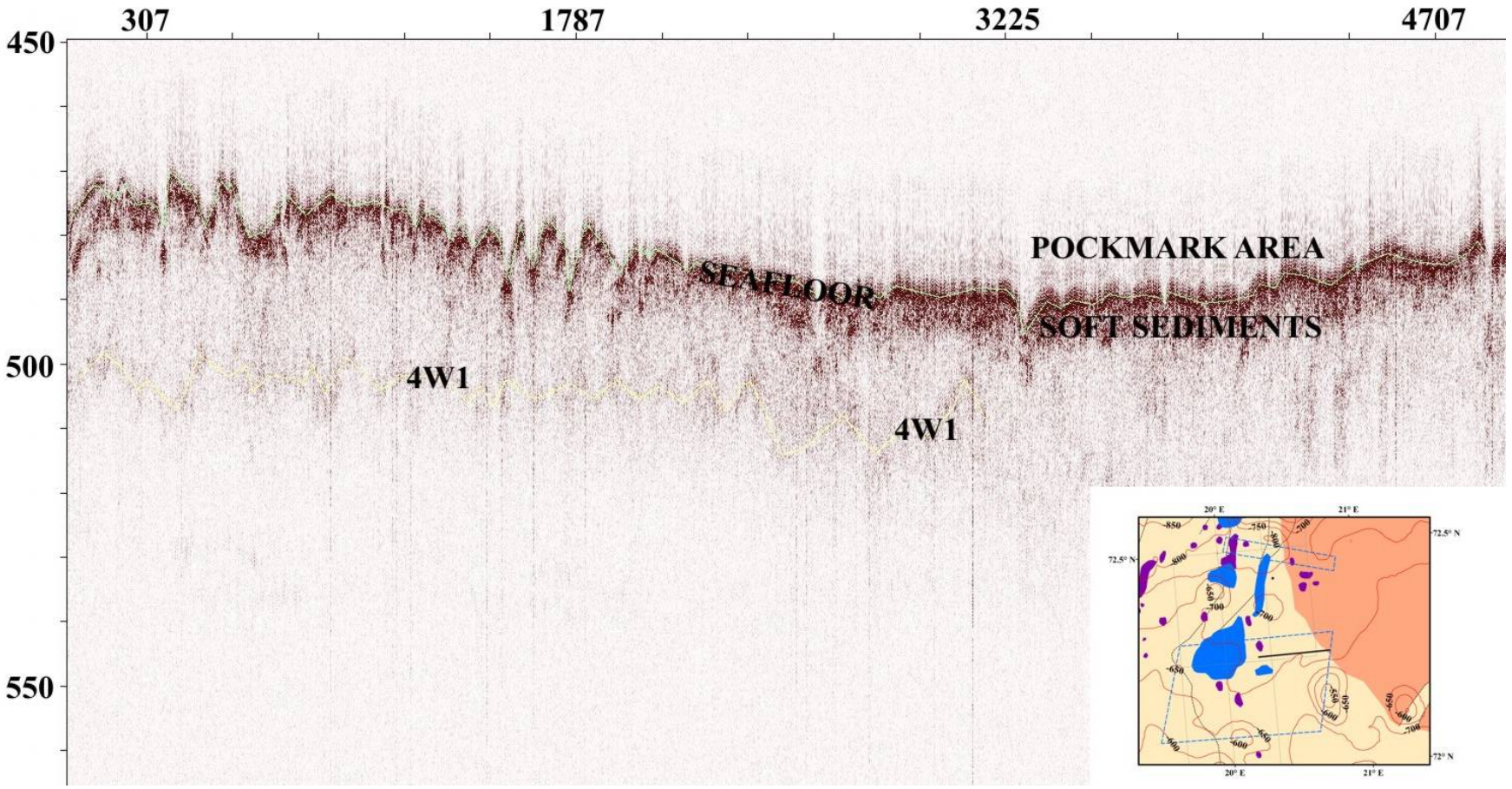

Figure 50. FFI TOPAS line 101065 in W-E direction indicating intra 4W reflection 4W1 within the unit 4W. The northern pockmark area is underlain by a thin layer of soft sediments overlying glacial till from the last glaciation (4W1) is also indicated.

5. CONCLUSIONS

1. Bathymetry and backscatter has given an overview of Holocene surface processes and their relation to subsurface geological processes. The backscatter data shows typical signatures of pockmarks and iceberg ploughmarks. Numerous pockmarks were identified in the two basins along the study area, but no water column gas flares were detected to indicate active gas leakage from the study area during the acquisition of the MBB data.
2. Gas and gas hydrate features (high amplitude reflections) were identified and related to gas hydrate stability conditions of the study area. BSR-like anomalies could be identified subparalleling the seafloor seismic reflection as patchy reflections. GHSZ modelling indicates gas hydrate stability for structure II hydrates with a few percent of ethane, propane or CO2.
3. Based on high-resolution seismic data, regional geology and Quaternary stratigraphy has been established for the study area, giving a detailed picture of depositional processes during post glacial times. Comparison of published dating results to the interpretations from this study indicates that the three major subunits from the Quaternary cover a total age of < 400 kyrs and thicknesses of up to 160 ms TWT. We identified two subunits, 4W1 and 4W2, within the youngest Quaternary unit, 4W, probably representing the two last glacial advances LGM I and II towards the present shelf edge.

6. REFERENCES

Andreassen, K. & Hansen, T. 1995: Inferred gas hydrates offshore Norway and Svalbard. Norsk Geologisk Tidskrift 45, 10-34.

Andreassen, K., Laberg, J.S. & Vorren, T.O. 2008: Seafloor geomorphology of the SW Barents Sea and its glaci-dynamic implications. Geomorphology 97, 157-177.

Bass, D.W. & Woodworth-Lynas, C. 1988: Iceberg crater marks on the sea floor, Labrador shelf. Marine Geology 79, 243-260.

Bellefleur, G., Riedel, M. & Brent, T. 2006: Seismic characterization and continuity analysis of gas hydrate horizons near Mallik research wells, Mackenzie Delta, Canada. The Leading Edge 599-604.

Buenz, S. & Mienert, J. 2004: Acoustic imaging of gas hydrate and free gas at the Storegga slide. Journal of Geophysical Research 109, doi:10.1029/2003JB002863.

Butt, F.A., Elverhøi, A., Solheim, A. & Forsberg, C.F. 2000: Deciphering Late Cenozoic development of the western Svalbard margin from ODP site 986 results. Marine Geology 169, 373-390.

Chand, S. & Minshull, T.A. 2003: Seismic constraints on the effects of gas hydrate on sediment physical properties and fluid flow: A review. Geofluids 3, 275-289.

Chand, S., Minshull, T.A., Gei, D. & Carcione, J.M. 2004: Elastic velocity models for gas-hydrate bearing sediments – A comparison. Geophysical Journal International 159, 573-590.

Chand, S., Rise, L., Ottesen, D., Dolan, M.F.J., Bellec, V. & Bøe, R. 2009: Pockmark like depressions near the Goliat hydrocarbon field, Barents Sea: Morphology and genesis. Marine and Petroleum Geology 26, 1035-1042.

Chand, S., Minshull, T.A., Priest, J.A., Best, A.I. & Clayton, C.R.I. 2006: An effective medium inversion algorithm for gas hydrate quantification and its application to laboratory measurements of gas hydrate bearing sediments. Geophysical Journal International doi:10.1111/j.1365-246X.2006.03038.

Chand, S., Mienert, J., Andreassen, K., Knies, J., Plassen, L., & Fotland, B. 2008: Gas hydrate stability zone modeling in areas of salt tectonics and pockmarks of the Barents Sea suggest an active hydrocarbon venting system. Marine and Petroleum Geology 25, 625-636.

Eldholm, O., Sundover, E., Myhre, A.M. & Faleide, J.I. 1984: Cenozoic evolution of the continental margin off Norway and western Svalbard. In: AM Spencer (ed) Petroleum geology of the North European Margin, Graham and Trotman, London, 3-18.

Eidvin, T. & Riis, F. 1989: Nye dateringer av de tre vestligste borehullene I Barentshavet. Resultater og konsekvenser for den tertiaere hevingen. NPD Contribution 27, 44 pp.

Eidvin, T., Brekke, H., Riis, F. & Rensaw, D.K. 1998: Cenozoic stratigraphy of the Norwegian Sea continental shelf 64^{o}N – 68^{o}N. Norsk Geologisk Tidskrift 78, 125-151.

Eidvin, T., Jansen, E. & Riis, F. 1993: Chronolgy of Tertiary fan deposits off the western Barents Sea: implications for the uplift and erosion history of the Barents Shelf. Marine Geology 112, 109-131.

Faleide, J.I., Solheim, A., Fiedler, A., Hjelstuen, B.O., Andersen, E.S., Vanneste, K. 1996: Late Cenozoic evolution of the western Barents Sea – Svalbard continental margin. Global and Planetary change 12, 53-74.

Guerin, G. & Goldberg, D. 2002: Sonic waveform attenuation in gas hydrate bearing sediments from the Mallik 2L-38 research well, Mackenzie Delta, Canada. Journal of Geophysical Research 107, doi:10.1029/2001JB000556.

Hald, M., Saettem, J. & Nesse, E. 1990: Middle and Late Weichselian stratigraphy in shallow drillings from the southwestern Barents Sea: foraminiferal, amino acid and radiocarbon evidence. Norsk Geologisk Tidskrift 70, 241-257.

Hobro, J.W.D., Minshull, T.A., Singh, S.C. & Chand, S. 2005: A three-dimensional seismic tomographic study of the gas hydrate stability zone offshore Vancouver Island. Journal of Geophysical Research 110, B09102, doi:10.1029/2004JB003477.

Holbrook, W.S., Gorman, A.R., Hornbach, M., Hackwith, K.L. & Nealon, J. 2002: Seismic detection of marine methane hydrate. The Leading Edge 686-689.

Hornbach, M.J., Holbrook, W.S., Gorman, A.R., Hackwith, K.L., Lizarralde, D. & Pecher, I. 2003: Direct seismic detection of methane hydrate on the Blake Ridge. Geophysics 68, 92-100.

Hovland, M., Ottesen, D., Thorsnes, T., Fosså, J.H. & Bryn, P. 2005: Occurrence and implications of large Lophelia-reefs offshore Mid Norway. Onshore-Offshore relationships on

the north Atlantic margin. Proceedings of the Norwegian Petroleum Society Conference, Norwegian Petroleum Society Special Publications 12, 265-270.

Hustoft, S., Buenz, S., Mienert, J. & Chand, S. 2009. Gas hydrates in mounded contourites; Implications on focussed fluid migration at the western Svalbard margin. Earth and Planetary Science Letters 284, 12-24.

Knies, J., Matthiessen, J., Vogt, C., Laberg, J.S., Hjelstuen, B.O., Smelror, M., Larsen, E., Andreassen, K., Eidvin, T. & Vorren, T.O. 2009: The Plio-Pleistocene glaciation of the Barents Sea-Svalbard region: a new model based on revised chronostratigraphy. Quaternary Science Reviews 28, 812-829.

Laberg, J.S., Andreassen, K. & Knutsen, A.M. 1998: Inferred gas hydrate on the Barents shelf – a model for its formation and a volume estimate. Geo Marine Letters 18, 26-33.

Laberg, J.S. & Vorren, T.O. 1996: The Middle and Late Pleistocene evolution of the Bear Island trough mouth fan. Global and Planetary Change 12, 309-330.

Lastochkin, A.N. 1977: Submarine valleys on the northern continental shelf of Europe, Izv. Vsesoy. Geogr. Obsh. 5, 412-417.

Lebesbye, E. 2000: Late Cenozoic glacial history of the south western Barents Sea. PhD Thesis, University of Tromsø, Tromsø.

Lebesbye, E. & Vorren, T.O. 1996: Submerged terraces in the southwestern Barents Sea: origin and implications for the late Cenozoic geological history. Marine Geology 130, 265-280.

Longva, O. & Thoresen, M. 1991: Iceberg scours, iceberg gravity craters and current erosion marks from a gigantic Preboreal flood in southeastern Norway. Boreas 20, 47-62.

Løseth, H., Lippard, S.J., Sættem, J., Fanavoll, S., Fjerdingstad, V., Leith, L.T., Ritter, U., Smelror, M. & Sylta, O. 1992: Cenozoic uplift and erosion of the Barents Sea – evidence from the Svalis Dome area. In : TO Vorren et al (eds) Arctic Geology and Petroleum Potential (Norw. Pet. Soc. Spec Pub. 2, Elsevier Amsterdam, 639-661.

Minshull, T.A. & Chand, S. 2009: The microstructure of sediment-hosted hydrates: evidence from effective medium modeling of laboratory and borehole datasets, Geological Society of London, special publication 319, ‘Sediment-hosted Gas Hydrates: New Insights on Natural and Synthetic Systems’, 93-101.

Monteys, X., Hardy, D., Doyle, E. & Garcia-Gil, S. 2008: Distribution, morphology and acoustic characterization of a gas pockmark field on the main shelf, NW Ireland, International Geological Congress Abstracts, Oslo.

Mørk, M.B. & Duncan, R.A. 1993: Late Pliocene basaltic volcanism on the western Barents shelf margin: implications from petrology and ^{40}Ar -^{39}Ar dating of volcani-clastic debris from a shallow drill core. Norsk geologisk Tidskrift 73, 209-225.

Nansen, F. 1904: The bathymetrical features of the North Polar seas with a discussion of the continental shelves and previous oscillations of the shoreline. Norwegian Polar Expeditions 1893-1896, Scientific results, vol. IV, 231pp.

Nyland, B., Jensen, L.N., Skagen, J., Skarpnes, O. & Vorren, T.O. 1992: Tertiary uplift and erosion in the Barents Sea: Magnitude, timing and consequences. In: RM Larsen and H Brekke, TB Larsen and E Talleraas (eds), Structural and tectonic modeling and its application to petroleum geology, Norw. Pet. Soc. Spec. Publ. 1, Elsevier, Amsterdam, 153-162.

Nøttvedt, A., Berglund, T., Rasmussen, E. & Steel, R. 1988: Some aspects of Tertiary tectonics and sediments along the western Barents shelf. In: Morton AC, and Parson LM, (eds): Early Tertiary volcanism and the opening of the NE Atlantic. Geological Society of London, special publication 39, 421-425.

Pratt, R.G., Bauer, K. & Weber, M. 2003: Crosshole waveform tomography velocity and attenuation of Arctic gas hydrates. SEG, Extended abstracts.

Riis, F. & Fjeldskaar, W. 1992: On the magnitude of the late Tertiary and Quaternary erosion and its significance for the uplift of Scandinavia and the Barents Sea. In: RM Larsen, H Brekke, BT Larsen, and E Talleraas (eds): Structural and tectonic modeling and its application to the Petroleum Geology NPF Special Publication 1, 163-185, Elsevier, Amsterdam.

Rise, L., Sættem, J., Rendall, H. & Nesteby, H. 1993: Database of sound velocities and related parameters in the upper part of the Norwegian continental shelf sediments. IKU Petroleum Research Report (Unpublished), pp 136.

Sheriff, R. 1980: Nomogram for Fresnel zone calculation. Geophysics 45, 968-972.

Shipley, T.H., Houston, M., Buffler, R.T., Shaub, F.J., McMillan, K.J., Ladd, J.W. & Worzel, J.L. 1979: Seismic reflection evidence for the wide spread occurrence of possible gas hydrate horizons on continental slopes and rises. American Association of Petroleum Geologists 63, 2204-2213.

Sloan, E. D. 1990: Clathrate Hydrates of Natural Gases, Marcel Dekker, NewYork.

Solheim, A., Faleide, J.I., Andersen, E.S., Elverhøi, A., Forsberg, C.F., Vanneste, K., Uenzelmann-Neben, G. & Channell, J.E.T: 1998. Late Cenozoic seismic stratigraphy and glacial geological development of the east Greenland and Svalbard-Barents Sea continental margins. Quaternary Science Reviews 17, 155-184.

Solheim, A. & Kristoffersen, Y. 1984: Sediments above the upper regional unconformity: thickness, seismic stratigraphy and outline of the glacial history, Norsk Polarinstitutt Skrifter 179B, 26pp.

Spencer, A.M., Home, P.C. & Berglund, L.T. 1984: Tertiary structural development of western Barents shelf: Troms to Svalbard. In: AM Spencer (ed) Petroleum geology of the North European Margin, Graham and Trotman, London, 199-210.

Stoll, R.D. & Bryan, G.M. 1979: Physical properties of sediments containing gas hydrates. Journal of Geophysical Research 84, 645-648.

Sættem, J., Poole, D.A.R., Ellingsen, L. & Sejrup, H.P. 1992: Glacial geology of outer Bjørnoyrenna, southwestern Barents Sea. Marine Geology 103, 15-51.

Sættem, J., Rise, L. & Westgard, D.A. 1992: Composition and properties of Glacigenic sediments in the southwestern Barents Sea. Marine Geotechnology 10, 229-255.

Thorsnes, T., Christensen, O. & Fosså, J.H. 2004: Deep water coral reefs – Acoustic recognition and geological setting. Hydro International 8, 26-29.

Vanneste, M., Batist, M.De., Gomshtok, A., Kremlev, A. & Versteeg, W. 2001: Multi-frequency seismic study of gas hydrate bearing sediments in Lake Baikal, Siberia. Marine Geology 172, 1-21.

Vorren, T.O., Hald, M. & Lebesbye, E. 1988: Late Cenozoic environments in the Barents Sea. Paleocenography 3, 601-612.

Vorren, T.O., Hald, M. & Thomsen, E. 1984: Quaternary sediments and environments on the continental shelf off northern Norway. Marine Geology 57, 229-257.

Vorren, T.O., Kristoffersen, Y. & Andreassen, K. 1986: Geology of the inner shelf west of North Cape. Norsk Geologisk Tidskrift 66, 99-105.

Vorren, T.O., Lebesbye, E., Andreassen, K. & Larsen, B. 1989: Glacigenic sediments on a passive continental margin as exemplified by the Barents sea. Marine Geology 85, 251-272.

Vorren, T.O., Lebesbye, E. & Larsen, K,B. 1990: Geometry and genesis of the glacigenic sediments in the southern Barents Sea, In: Dowdeswell JA and Scourse JD, (eds) Glacimarine environments, processes and sediments, Geol Soc London, Sp Publ. 53, 309-328.

Vorren, T.O., Richrdsen, G., Knutsen, S.M. & Henriksen, E. 1991: Cenozoic erosion and sedimentation in the western Barents Sea. Marine and Petroleum Geology 8, 317-340.

Westbrook, G. K., Chand, S., Rossi, G., Long, C., Buenz, S., Camerlenghi, A., Carcione, J.M., Dean, S., Foucher, J.P., Flueh, E., Gei, D., Haacke, R.R., Madrussani, G., Mienert, J., Minshull, T.A., Nouze, H., Peacock, S., Reston, T.J., Vanneste, M. & Zilmer, M. 2008: Estimation of gas hydrate concentration from multicomponent seismic data at sites on the continental margins of NW Svalbard and the Storegga region of Norway. Marine and Petroleum Geology 25, 744-758.

Williams, D.F., Thunell, R.C., Tappa, E., Rio, D. & Raffi, I. 1988: Chronology of the Pleistocene oxygen isotope record: 0-1.88 m.y. B.P. Palaeogeography Palaeoclimatology and Palaeoecology 64, 221-240.